New Ion Mobility Measurements Enabled by Innovations in Instrumentation and Modeling

AnneClaire Wageman

A dissertation

submitted in partial fulfillment of the

requirements for the degree of

Doctor of Philosophy

University of Washington

2025

Reading Committee:

Matthew F. Bush, Chair

Nicholas M. Riley

Robert E. Synovec

Program Authorized to Offer Degree:

Chemistry

University of Washington

Abstract

New Ion Mobility Measurements Enabled by Innovations in Instrumentation and Modeling

AnneClaire Wageman

Chair of the Supervisory Committee:

Matthew F. Bush

Department of Chemistry

This thesis describes the characterization of a novel traveling-wave (TW) ion mobility (IM) device and a method to assess the impacts of experimental conditions on ion internal temperatures. IM is a gas-phase analytical technique that separates analyte ions on the basis of shape, size, and charge and is often coupled with mass spectrometry (MS) to yield structural information on top of mass-to-charge (m/z). Chapter 1 contains an overview of IM-MS techniques, with a particular focus on recent advances and their application to structural studies of biomolecular ions. The following chapters describe experimental and computational approaches to assess activation within TWIM separations, including a novel method for precisely controlled ion heating.

Our lab has previously designed and implemented several ion mobility devices constructed using the Structures for Lossless Ion Manipulations (SLIM) architecture, in which

ion motion is controlled by potentials applied to mirrored pairs of printed circuit boards; these previous implementations all employed electrostatic fields. Engineering challenges posed by this method led us to consider alternative strategies, including traveling waves. Chapter 2 presents a novel TW-SLIM instrument consisting of two antiparallel IM regions controlled by traveling waves enabling tandem and IM separations involving multiple passes around the SLIM device. Tandem IM separations of native-like protein ions performed with this instrument demonstrate the ability to control protein ion structural states via tuning of applied potentials.

Chapter 3 details a statistical method for quantifying the internal temperatures of ions under IM conditions, including those described in Chapter 2. Results of ion trajectory simulations performed on a geometric model of a similar TW-SLIM device indicate that minimal ion heating occurs during transmission through the separation region, while significant ion heating occurs while ions are trapped or stored. Additionally, computational results indicate that instrument parameters including background gas pressure, wave height, and guard electrode potential impact ion temperatures to varying extents. Results from the work described in this dissertation have implications for structural conclusions drawn from ongoing and future IM work, especially as commercialization expands the use of the technique.

Dedication

For KLS: everything I've done is because of you

Acknowledgments

I'd like to dedicate a few pages to thanking the many people who have offered me help and support throughout my time in graduate school. First and foremost, thank you to my advisor, Dr. Matt Bush. Matt does incredible science, and I'm grateful to have been able to participate in and contribute to such an exciting body of work. His guidance has helped me to develop a level of confidence and an ability to approach complex problems that I never thought I would have. I also appreciate the emphasis Matt placed on presentation, writing, and data visualization skills. Finally, Matt's concern for his students and our success was always apparent to me and helped me to stay motivated through the ups and downs of my Ph.D. I will always be thankful for the time and effort Matt committed to my scientific development – none of this work would have been possible without him.

The research group Matt has cultivated has also been supportive on a scientific and personal level. To all the members of the Bush group that I've overlapped with, thanks for your feedback and questions on my presentations and helpful discussions at journal club meetings. To Dr. Rae Eaton, thank you for training me on instrument assembly and troubleshooting. To Addison Roush and Bruce Feng, I can't thank you enough for your help with data collection and getting the new instrument up and running. Building an instrument is really hard, so thanks for sticking with me through the process. I'm excited about the future directions for the SLIM project and can't wait to see what you both do next. To Dr. Meagan Gadzuk-Shea and Dr. Theresa Gozzo, I'm so thankful to you both for being there through some of the more challenging years of my Ph.D. To Chris Weir, thank you for the bus-ride and office chats, both science-related and not. To Chris and Addison, your friendship during the last year of my Ph.D.

was instrumental to my sanity. To Meagan (and Misa!), May Constabel, and Carley Hinrichs, thanks for being great officemates over the years.

Within the Chemistry Department, I'd like to thank Dr. Ashley Dostie for her support, first as a fellow TA and later as an instructional tech for several courses I taught. I'm also thankful to Dostie for putting so much effort into building a welcoming and inclusive community when I was new to the department. Thanks to the instructors and TAs of the courses I both took and taught for, as well as to my students, who all contributed to my learning in different ways. Thanks to the many staff members in the front office and stockroom who were always helpful with bureaucracy, paperwork, orders and shipments, etc.

To Gordon Anderson, thank you for many hours of help with development and troubleshooting of the MIPS systems and software. To Brian Wadey and especially to Kevin Soderlund in the machine shop, thank you so much for all your work on fabricating vacuum parts for my instrument and for always being flexible and willing to help solve problems. Next, thank you to all my committee members: Dr. Rob Synovec, Dr. Nick Riley, Dr. Frank Turecek, Dr. Mike Guttman, Dr. Ashleigh Theberge, and Dr. Dan Fu. I sincerely appreciate your time, flexibility with scheduling, and insightful questions about my work over the years.

I'm also deeply grateful to my friends and family – I wouldn't be here without you. To Shyam, thank you for being my first Seattle housemate and for introducing me to the friends who made Seattle home for me. To Tom and Susan, thank you for your endless hospitality. The Thanksgiving and Fourth of July weekends I spent at your house are some of my favorite Seattle memories. To Ian, Mimi, Matt, and Bekah, thank you for your constant friendship. The four of you have been here for me through the good times and hard times of the past few years, and I'm not sure how I would have gotten through it without you. We've been through so many changes

and adventures together, and I'm looking forward to what the future holds for all of us. To my parents, I am so thankful for how supportive you are of whatever I choose, no matter how far away it takes me. To Caroline and Josh, thank you for the visits and for staying close despite the distance. I hope we can all see each other more often now. To Conor, thank you for your endless encouragement, advice, commiseration, and humor. Your impact on my life, my outlook, and my accomplishments is impossible to measure, even for an analytical chemist. Finally, to Jimmy, thank you for being by my side through it all and picking me up when I'm down. I'm looking forward to all the marathons in our future, both figurative and literal.

Table of Contents

Abstract 3
Acknowledgments 6
Chapter 1. Introduction 11
1.1 Abstract 11
1.2 Foundations of Ion Mobility 11
1.2.1 Ion Mobility Theory 11
1.2.2 Electrodynamic IM 14
1.3 Structures for Lossless Ion Manipulations 16
1.3.1 Electrostatic Voltage Control 16
1.3.2 Traveling-wave SLIM 17
1.4 Applications 17
1.4.1 Structural Biology 17
1.4.2 Next-generation Implementations 19
1.5 Effective Ion Temperatures 21
1.5.1 Theory & Motivation 21
1.5.2 Experimental Estimates 23
1.5.3 Computational Estimates 23
1.6 Current Work 24
1.7 References 25
Chapter 2. SLIMPHONY: A New SLIM-Based Instrument That Orchestrates Complex Ion Mobility–Mass Spectrometry Experiments 43
2.1 Abstract 43
2.2 Introduction 44
2.3 Methods 47
2.3.1 Sample Preparation 47
2.3.2 Instrumentation 48
2.3.3 Voltage Control 50
2.4 Results & Discussion 51
2.4.1 Instrument Operation 51
2.4.2 Single-Pass IM-MS 52
2.4.3 Multiple-Pass IM-MS 54

2.4.4 Time-Dependent, Selection-Trapping IM-IM-MS 56
2.4.5 Activating Ions Between Dimensions of Selection-Trapping IM-IM-MS ... 59
2.4.6 Combining Multiple Passes and Activation in Selection-Trapping IM-IM-MS 61
2.5 Conclusions 64
2.6 Acknowledgments 66
2.7 References 66
Chapter 3. Conformational Landscapes Observed through Controlled Kinetics (CLOCK): Using Precision Heating to Characterize Protein Dynamics in the Gas Phase 79
3.1 Abstract 79
3.2 Introduction 80
3.3 Methods 83
3.3.1 CLOCK Experiments 83
3.3.2 Trajectory Simulations 85
3.3.3 Statistical Analysis of Effective Translational Temperatures 87
3.3.4 Software Availability 88
3.4 Results & Discussion 88
3.4.1 CLOCK Analysis of 6+ Ubiquitin 89
3.4.2 Ion Effective Temperatures Increase During Trapping 91
3.4.3 Effects of Applied Potentials on Effective Temperatures of Trapped Ions 94
3.5 Conclusions 98
3.6 Acknowledgements 99
3.7 References 99
Appendix A: Supporting Information for Chapter 2 108
A.1 Supplementary Information 108
Appendix B: Supporting Information for Chapter 3 111
B.1 Supplementary Information 111
B.2 Sample SIMION user program 120
B.3 Sample SIMION trajectory data 122
B.4 iontemperature.py 125

Chapter 1. Introduction

1.1 Abstract

Advances in understanding the mechanisms of diseases and developing therapeutics require structural techniques that are sensitive to the dynamics and heterogeneity characteristic of many biomolecules. Ion mobility (IM) mass spectrometry (MS) can be used to study native-like structures of large biomolecules including proteins and protein complexes. Recent developments in IM-MS, including the use of traveling waves to drive ion motion and the development of the Structures for Lossless Ion Manipulations (SLIM) architecture, have led to increases in resolution and selectivity, improving performance for analytes with only subtle differences in structure as well as those that exist in complex biological mixtures. There remain outstanding questions regarding structural changes that may occur during the course of IM-MS experiments. In this work, I report on the design and characterization of a novel traveling-wave (TW) IM-MS instrument capable of precision heating of selected protein ions to control the distribution of structural states and use a computational method to quantify ion heating under IM conditions.

1.2 Foundations of Ion Mobility

1.2.1 Ion Mobility Theory

Ion mobility spectrometry (IMS) is a gas-phase electrophoretic separation technique that is sensitive to differences in ion shape, size, and charge.[1] Opposing forces from 1) an applied electric field and 2) interactions with neutral gas molecules act on ions differentially according to these properties. By applying an electric field in the presence of a neutral bath gas, ions of different shape, size, and charge can be made to traverse a separation region with different velocities, resulting in a temporal separation. Ion mobility (IM) has seen a significant growth in

popularity as an analytical technique since being coupled with mass spectrometry (MS).[2] Like MS, IM requires analytes to be gas-phase ions. IM separates ions based on their mobilities under a set of experimental conditions and thus provides complementary information to the mass-to-charge ratio (m/z) reported by MS.

The mobility, K, of an ion is governed by the relationship

$$v_D = KE = \frac{L}{t_D} \tag{1.1}$$

where v_D is the steady-state velocity of the ion, E is the electric field, L is the length of the separation region, and t_D is the drift time of the ion. In an IM separation, the analytical readout is arrival time, t_A, which corresponds to the time at which an ion is detected downstream of the separation and encompasses time an ion spends both in the separation region, t_D, and outside the separation region, t_0:

$$t_A = t_D + t_0 \tag{1.2}$$

To determine K from experimental arrival-time data, Equations 1 and 2 can be combined as follows:

$$t_A = \frac{L}{KE} + t_0 \tag{1.3}$$

The Mason-Schamp equation[3] relates the mobility of an ion to the collision cross section Ω of the ion-neutral pair:

$$\Omega = \frac{3ez}{16N}\left(\frac{2\pi}{\mu k_B T_{eff}}\right)^{1/2}\frac{1}{K} \tag{1.4}$$

where e is the elementary charge, z is the charge of the ion, N is the drift-gas number density, μ is the reduced mass of the ion-neutral pair, k_B is the Boltzmann constant, and T_{eff} is the effective temperature of the ion. This relationship is valid under the low-field limit, in which v_D is

sufficiently low compared to the ion-neutral speed in the absence of E such that T_{eff} is equivalent to the neutral gas temperature, T_{gas}.[4,5]

Traditional IM instrumentation consists of a series of stacked ring electrodes connected to a voltage divider network, which will be referred to as "electrostatic IM" because this implementation applies a uniform electric field over the separation region.[6] In electrostatic IM, uncertainty in **Ω** determination can arise from ion diffusion,[7] ion population heterogeneity, uncertainty in t_0, and deviations from the low-field limit.[8] Ion diffusion along the axis of transmission leads to broadening in the arrival-time distribution and lowers resolving power,[7] while radial ion diffusion leads to losses via collisions with electrode surfaces and lowers overall ion intensity.[7] Superimposing alternating-polarity rf waveforms on adjacent electrodes spanning the separation region has been shown to mitigate ion loss due to radial diffusion[9] while preserving determined **Ω** values[10,11] and contributing minimally to effective ion temperatures under the conditions and geometry considered.[9]

IM resolving power, R_p, ideally scales with the square root of separation length and electric field, as follows:[12]

$$R_p = \frac{t_D}{t_{FWHM}} \sim \left(\frac{LE}{T}\right)^{1/2} \tag{1.5}$$

where t_{FWHM} is the width of the arrival-time peak at half its maximum value. Increasing E to improve R_p risks violating the low-field limit, as described previously. Increasing L for a drift tube increases ion diffusion, instrument size, and the input voltage required to establish a uniform electric field. The engineering challenges posed by large instrument footprints and propensity for electrical breakdown induced by high input voltages[13] have been addressed in part by introducing electrodynamic fields to drive IM separations.

1.2.2 Electrodynamic IM

Electrodynamic fields have been employed for IM separations via traveling waves,[14] which are the primary focus of this work, and gradient electric fields.[15] Briefly, a gradient electric field applied counter to a neutral gas flow confines ions at positions dependent on their mobilities in trapped IMS (TIMS),[15] and separation is achieved by decreasing the field gradient as a function of time to elute trapped ions in order of mobility. In traveling-wave (TW) IM, moderate potentials of tens of volts are propagated in series down the length of the separation region. The potential at a given position along the axis of transmission varies with time. An ion in a TW device moves with a velocity that depends on mobility when subjected to the electric field resulting from the traveling wavefront (Equation 1).[16] This results in the ion being pushed in front of the wave, while drag caused by collisions with background gas molecules impedes ion motion.[16] If the drag is sufficient, that wave will propagate past the ion, and the ion will be subject to the electric field imposed by the next wavefront.[16] This process is governed by mobility, leading to temporal dispersion as in electrostatic IM separations. The speed and amplitude of the traveling waves can be varied to alter the electric fields and, thereby, the separation: ions may not separate from other ions of different mobilities if insufficient roll over events occur, while ions moving much more slowly than the traveling waves experience many roll over events and may not be pushed forward enough to reach the end of the separation region.[16,17]

Because the potential at each point along L varies in a TWIM separation, E is not uniform. Instead, it varies with time and position, affecting the instantaneous velocity of an ion as in Equation 1. Thus, ions in TWIM devices spend different amounts of time in regions with different electric fields, and determining mobility as established in Equations 1 and 3 is not

trivial.[18,19] An alternative strategy to the direct determination of K is calibration to electrostatic measurements. Calibration accuracy is limited by differences in charge state,[20] molecular class,[21] and effective temperatures[8] between the calibrants and analytes, as well as background gas identity.[8,22] Traditional calibration methods use an empirically-determined power function to derive TW K values from measured TW t_A values and directly-determined drift-tube K values.[23] More recently, a new approach to calibration called IMSCal[24] has been introduced that predicts Ω by taking TW-specific velocity relaxation[17] and varied confinement effects into account.

Stacked ring electrode architectures have been adapted for TWIM separations[14,25] by modifying the circuit applied to them; instead of a voltage divider network, every *n*th electrode is electrically connected. This allows a series of traveling waves to be propagated by applying a potential to a number $<n$ of adjacent electrodes, applying the same magnitude negative potential or zero potential to the subsequent electrodes $\leq n$, and shifting the phase of this pattern at a defined frequency. TWIM has been implemented commercially by Waters Corp.;[25,26] the Synapt series of TWIM instruments has been used extensively to complement MS analysis of analytes spanning a wide range of sizes and molecular classes.[27–31] The electric field driving ion motion in a TWIM device is defined by the motion of the traveling wave rather than the monotonically decreasing potentials characteristic of an electrostatic system; input voltages of tens of volts can be used to drive IM separations of arbitrary lengths. However, due to the linear geometric constraints of stacked ring electrodes, increasing L beyond 1-2 meters remains impractical in most laboratory settings.

1.3 Structures for Lossless Ion Manipulations

1.3.1 Electrostatic Voltage Control

Smith and colleagues at the Pacific Northwest National Laboratory developed an alternative architecture for IM separations called Structures for Lossless Ion Manipulations (SLIM).[32] SLIM devices consist of mirrored pairs of printed circuit boards (PCBs) with electrodes used to generate the electric fields driving IM separations deposited directly onto their surfaces. A SLIM board contains a set of "rung" electrodes analogous to the ring electrodes of the drift tube flanked by a set of "guard" electrodes. A uniform electric field can be established by applying a voltage divider network to the rung electrodes and alternating rf potentials can be applied to improve ion confinement between the electrode surfaces. Because of the planar geometry, applied rf no longer confines ions radially. A separate voltage divider network applied to the guard electrodes enables the application of a confining electric field that prevents ion losses due to lateral diffusion.

Early implementations of electrostatic SLIM demonstrated its ability to transmit ions over a linear path as well as one incorporating a 90 ° turn[32] and to trap ions for several hours without significant losses.[32] To evaluate the utility of SLIM for IM, time-based resolving powers were reported for separations of commercial tuning mix ions[32] and Ω values for protein and protein complex ions were determined and found to be consistent with those resulting from rf-confining drift cell measurements.[33] Notably, results from electrostatic SLIM separations indicated that the architecture is capable of maintaining sufficiently gentle conditions to preserve native-like structures of protein and protein complex ions throughout analysis.[33] With the introduction of 90 ° turns to ion trajectories came the ability to mobility-select and isolate ion populations for separate manipulation including trapping.[34,35]

1.3.2 Traveling-wave SLIM

Smith and colleagues also used the SLIM architecture with electrodynamic fields to drive IM separations. A TW-SLIM board consists of repeating electrode units deposited on PCB surfaces to establish a separation path of arbitrary geometry. Each traveling wave unit contains alternating polarity rf electrodes interleaved by sets of DC (TW) electrodes and are flanked by guard electrodes on both sides. As with the TW circuits applied to stacked ring electrodes, the *n*th electrode of each repeating unit is electrically connected so the wave can be propagated down the length of the device. Early linear TW-SLIM instruments demonstrated comparable performance in terms of resolving power and peak-to-peak resolution to radial-symmetry TWIM separations with similar lengths and showed that separation performance could be optimized by adjusting the wave speed, amplitude, and shape.[36] A TW-SLIM device featuring an electrode path with sixteen 90 ° turns was compared to an electrostatic drift tube and exhibited similar separation performance for peptide and tetrasaccharide isomers.[37] Applying traveling waves to SLIM addresses the issue of high operating voltage requirements posed by electrostatic profiles, while also eliminating the linear separation path limitations inherent to the traditional stacked ring electrode architecture.

1.4 Applications

1.4.1 Structural Biology

Large biomolecules are often heterogeneous in terms of structure, assembly, and interactions with other species in solution. In particular, proteins and protein complexes can adopt a range of higher order structures that are intrinsically linked to their biological activity. Such dynamic features are difficult to study via the typical structural biology techniques of x-ray crystallography[38] and cryogenic electron microscopy,[39] which favor purified, highly

concentrated, and crystallized samples. MS has seen extensive use in bottom-up protein sequencing,[40] which provides rich information about protein primary structure at the expense of higher-order interactions. Top-down MS analysis of intact protein ions can identify specific combinations of post-translational modifications that make up unique proteoforms.[41] MS techniques alone, however, only detect *m*/*z* and remain insensitive to isomerism and structural heterogeneity.

Bottom-up and top-down MS proteomics methods usually use electrospray ionization (ESI) to ionize proteins and transfer them to the gas phase.[42] Electrospray ionization[43] is a soft technique in which a kilovolt potential is applied to a capillary containing the analyte dissolved in a volatile solvent. This causes charged droplets to break free from the solvent surface. As the solvent evaporates, the droplets shrink, become unstable, and eject desolvated analyte ions. ESI enables the transfer of intact protein and peptide ions into the gas phase without further fragmentation,[44] but solvents used often lead to denaturation,[45] limiting the study of higher-order structures. Reducing the flow rate and capillary diameter used for ESI both consumes less analyte material and allows the use of solvents mimicking the biological environment,[45,46] including aqueous solutions, neutral pH values, and small-molecule additives that help biomolecules maintain their structures. This modified ionization technique, called nano-ESI (nESI), has been shown to preserve aspects of native protein and protein complex structures including quaternary assemblies into the gas phase under optimized solution and instrument conditions.[47] Combining native MS with IM separation has proved useful for probing many aspects of protein structural dynamics, including temperature-induced folding and unfolding,[48–52] responses to intermolecular interactions,[53–55] and oligomerization processes.[56–58]

1.4.2 Next-generation Implementations

High-Resolution IM Instrumentation

To increase the utility of IM to the study of increasingly complex samples, next-generation separation strategies have sought to improve IM resolving power and increase the orthogonal information content of IM-MS experiments. Per Equation 5, theoretical IM resolving power scales with the square root of separation length. Increasing separation length in electrostatic and drift tube IM devices is limited by input voltage and linear geometry requirements, challenges addressed by the development of TW-SLIM. By arranging TW electrodes in a serpentine shape, a 13-m separation path was collapsed onto a 45.9 cm x 32.5 cm PCB, yielding a 5-fold improvement in resolution for a separation of commercial tuning mix ions compared to a 90-cm electrostatic drift tube.[59] An iteration on this design that allowed ions to be re-cycled on the same boards for additional IM separation drastically increased the separation length possible for a single IM experiment; a 40-pass separation of tuning mix ions (equivalent to 540 m) improved resolution 30 fold over the 90-cm drift tube.[60] Extended separation lengths can lead to increased ion diffusion along the transmission axis, leading to broad arrival-time peaks and artificially-suppressed ion intensities.[61] Spatial compression of ions mid-TW separation has been achieved by interfacing moving and stationary traveling waves resulting in narrower peaks while maintaining peak-to-peak resolution.[61]

Tandem IM and Hyphenated IM Techniques

Tandem IM and combining IM with other analytical techniques have enabled experiments capable of providing new structural insights. In tandem IM, multiple IM separations, called dimensions, are performed sequentially. Species of interest can be mobility-selected and activated, fragmented, or otherwise manipulated between IM separations. Pioneered

by Clemmer and colleagues using electrostatic drift tubes connected in series, early tandem IM experiments demonstrated evidence for multiple closely-related structures comprising arrival-time peaks corresponding to protein ion conformers.[62] Tandem IM has incorporated collision-induced dissociation (CID) between IM dimensions to resolve structures of peptide,[63,64] protein,[63,64] and carbohydrate[65] fragment ions. Notably, tandem IM experiments performed on electrostatic SLIM instruments have revealed structural changes in small, monomeric protein ions with increased trapping time between IM dimensions,[66,67] while no similar changes were observed for larger, multimeric protein complex ions.[67] These results have implications for protein and protein complex ion stability over the course of increasingly long IM separations. TW-SLIM has been combined with CID and cryogenic infrared spectroscopy to create a new method for identifying glycans[68–72] and with liquid chromatography to separate lipid isomers[73] and peptides containing modifications impacting their therapeutic function.[74]

Trajectory Simulations

Because IM relies on the interactions of multiple simultaneous and sometimes dynamic electric fields, the potential surfaces ions experience can be complex and computationally intensive. IM instrument design has been supported by the use of SIMION, a software package that simulates ion trajectories through static and quasistatic electric fields. The geometric arrangement of electrodes within an IM instrument are modeled, and SIMION uses user-defined potentials to calculate the electric fields present. Ion parameters including mass, charge, and **Ω** and background gas parameters are used to calculate trajectories based on the electric fields and ion-neutral collisions. SIMION simulations have been used to validate IM instrumentation[14,75–79] and experiment design[61,80–82] by predicting ion behavior under various conditions.

Commercial Implementations of TWIM

TWIM instruments have been introduced commercially, leading to increased use across a wide range of structural biology applications. Waters Corp. has commercialized a TW-based, tandem-IM enabled system employing alternative electrode architecture. The Cyclic IMS (cIMS) system contains a racetrack-like structure composed of mirrored electrodes arranged in a loop with a short switching region used to inject and remove ions from the separation region.[75] Ions can be cycled multiple times to perform multipass separations of arbitrary length.[75] Ion subpopulations can also be isolated and activated before, between, or after passes, which has been applied widely to assess protein structure interconversion,[83,84] characterize and identify complex glycans and carbohydrates,[85–87] and increase top-down sequence coverage of large proteins that normally yield congested fragment spectra.[88] The 13-m multipass-enabled TW-SLIM device originally introduced by Smith and coworkers has been commercialized by MOBILion Systems.[89] This system has been used to separate isomeric metabolites of synthetic cannabinoids,[90] vitamin D,[91] and cyclic peptides[92] in studies representing the development of new methods incorporating TW-SLIM to characterize biologically-relevant species resistant to traditional techniques. Clowers and colleagues have introduced open-source tools to aid in TW-SLIM device design and validation to make the technique more widely accessible to researchers with the analytical need for IM capabilities but who may lack engineering expertise.[93,94]

1.5 Effective Ion Temperatures

1.5.1 Theory & Motivation

As described in 1.2.1, the Mason-Schamp equation (Equation 1.4) used to calculate **Ω** depends on the effective ion temperature, T_{eff}. Within the low-field limit, the majority of the kinetic energy of the ion is in the form of thermal energy, with minimal contributions from the

electric field,[95] and T_{eff} is assumed to be equal to the background gas temperature, T_{gas}. The magnitude of the applied electric field varies across different IM separations, which may result in values for T_{eff} that exceed T_{gas}.[22] Corrections that account for contributions to ion drift velocity from the applied electric field have been derived from first principles. The two-temperature theory includes an additional term in the approximation of T_{eff} to account for non-negligible ion drift velocity:

$$T_{eff} = T_{gas} + \frac{m}{3k_B} v_D^2 \tag{1.6}$$

where m is the mass of the gas, assuming elastic collisions.[3]

Elevated T_{eff} is of particular concern for TWIM separations, in which ions may experience high electric fields for some portions of the separation.[5,8,95] Because the electrodynamic fields present in TWIM separations complicate the direct determination of **Ω** from arrival-time measurements, **Ω** values from electrostatic IM separations are often used to calibrate TWIM separations. Calibration methods implicitly assume that T_{eff} and other instrumental parameters are the same between the calibrant and target methods.[8] Deviation from this assumption is a potential source of error in **Ω** values determined from TWIM measurements. Studies have shown that collisional heating of native-like protein ions in a TWIMS device can result in changes in **Ω** that reflect changes in the distribution of structural states occupied by the ion population.[96] With the application of IM-MS to structural studies of protein and other biomolecular ions, there is a broad need to assess whether instrument conditions that affect T_{eff} are gentle enough to maintain native-like structures similar to those found in solution or to assess the extent of activation they may induce. Estimating T_{eff} for actual IM device geometries and separation conditions will help to inform the models used for **Ω** determination and any structural conclusions that may be drawn.

1.5.2 Experimental Estimates

Several experimental and computational approaches have been employed to characterize effective ion temperatures in IM separations. T_{eff} has been estimated experimentally by measuring fragmentation yields of thermometer ions under different TW conditions and relating the rate constant of dissociation with a Boltzmann energy distribution.[97,98] The temperature of ions in the separation is assumed to be the temperature that would yield the observed extent of fragmentation. Results from studies of thermometer ions measured on Waters SYNAPT first- and second-generation TWIM instruments indicate that ion heating above ambient temperatures does occur in TWIM separations, but the extent varies based on TW conditions and ion size and charge. Ion heating was found to be more significant 1) during injection into the IM region than during IM separation,[98,99] 2) for smaller ions,[99] and 3) at higher TW heights, lower TW speeds, and lower pressures.[97] The ion heating observed in TWIM separations has implications for structural studies, particularly for **Ω** calibration with data obtained from electrostatic measurements with lower effective ion temperatures and for the ability to observe native-like structures.[97]

1.5.3 Computational Estimates

Computational approaches to estimating T_{eff} throughout the course of IM separations have used SIMION trajectory simulations to sample ion velocities during IM separations. The velocities of the gas molecules follow a Maxwell-Boltzmann distribution dependent on T_{gas}. From these, an ion-neutral relative speed distribution can be constructed and compared to Boltzmann distributions at various temperatures to determine the effective temperature of the ion-neutral collisions.[9] Results from a study applying this method to electrostatic drift tubes

show that rf-confining potentials can lead to modest increases in T_{eff} for small analytes like peptide ions and have a negligible effect on T_{eff} for protein complex ions.

Understanding the effects of IM experimental conditions and ion-neutral collisions on ion temperatures is an area of ongoing current research. A recent review of numerical approaches to predicting mobilities presents a comprehensive list of factors impacting mobility that are often overlooked in IM experiments and calculations, including high electric fields, collision inelasticity, rotational energy of ions, and gas polarizability.[100] The Prell group has developed a software tool called IonSPA and incorporated partially-inelastic collision models to calculate changes in ion temperature in collision-induced dissociation and collision-induced unfolding (CIU) experiments.[101] IonSPA calculations were used to predict heating and cooling for 7+ cytochrome *c* ions at pressures consistent with IM separations.[101] Applying IonSPA calculations to electric fields present in TWIM systems will provide a valuable point of comparison to existing methods for modeling ion trajectories and effective temperatures.

1.6 Current Work

The work described in this thesis focuses on characterizing the structures of protein ions in TW-SLIM devices. TWIM and TW-SLIM systems have recently been commercialized and are seeing broader use for structural biology analyses. Because results from IM experiments are used to draw conclusions about gas-phase ionic structures, it is important to understand the extent to which these structures may be impacted by the conditions present in these devices. This knowledge is critical for the study of native-like structures by TWIM as well as methods that rely on intentionally perturbing ionic structures to study their dynamics.

In Chapter 2, a novel TW-SLIM device is described and results from tandem and multiple-pass separations of protein, peptide, and small molecule ions are reported. Among these

is a novel method of activating ions, in which a subpopulation of ions is selected and trapped following an initial ion mobility separation. During trapping, the electric potential applied to a set of electrodes used to confine ions during the separation is modulated, which can induce structural changes to the trapped ion population. Chapter 3 uses ion trajectory simulations under conditions comparable to those used on the instrument described in Chapter 2 to assess the effective temperatures of ions within the TW-SLIM device. The results reported in this dissertation will help to contextualize the structural conclusions drawn from future TWIM and TW-SLIM studies.

1.7 References

(1) Hill, H. H.; Siems, W. F.; Louis, R. H. St.; McMinn, D. G. ION MOBILITY SPECTROMETRY. *Anal. Chem.* **1990**, *62* (23), 1201A-1209A. https://doi.org/10.1021/ac00222a716.

(2) May, J. C.; McLean, J. A. Ion Mobility-Mass Spectrometry: Time-Dispersive Instrumentation. *Anal. Chem.* **2015**, *87* (3), 1422–1436. https://doi.org/10.1021/ac504720m.

(3) Mason, E. A.; McDaniel, E. W. *Transport Properties of Ions in Gases*, 1st ed.; Wiley, 1988. https://doi.org/10.1002/3527602852.

(4) Siems, W. F.; Viehland, L. A.; Hill, H. H. Improved Momentum-Transfer Theory for Ion Mobility. 1. Derivation of the Fundamental Equation. *Anal. Chem.* **2012**, *84* (22), 9782–9791. https://doi.org/10.1021/ac301779s.

(5) Webb, I. K. Perspective: The Complex Relationship between Charge, Mobility, and Gas-phase Protein Structure. *J. Mass Spectrom.* **2024**, *59* (5), e5013. https://doi.org/10.1002/jms.5013.

(6) Dugourd, Ph.; Hudgins, R. R.; Clemmer, D. E.; Jarrold, M. F. High-Resolution Ion Mobility Measurements. *Rev. Sci. Instrum.* **1997**, *68* (2), 1122–1129. https://doi.org/10.1063/1.1147873.

(7) Tang, K.; Shvartsburg, A. A.; Lee, H.-N.; Prior, D. C.; Buschbach, M. A.; Li, F.; Tolmachev, A. V.; Anderson, G. A.; Smith, R. D. High-Sensitivity Ion Mobility Spectrometry/Mass Spectrometry Using Electrodynamic Ion Funnel Interfaces. *Anal. Chem.* **2005**, *77* (10), 3330–3339. https://doi.org/10.1021/ac048315a.

(8) Gabelica, V.; Shvartsburg, A. A.; Afonso, C.; Barran, P.; Benesch, J. L. P.; Bleiholder, C.; Bowers, M. T.; Bilbao, A.; Bush, M. F.; Campbell, J. L.; Campuzano, I. D. G.; Causon, T.; Clowers, B. H.; Creaser, C. S.; De Pauw, E.; Far, J.; Fernandez-Lima, F.; Fjeldsted, J. C.; Giles, K.; Groessl, M.; Hogan, C. J.; Hann, S.; Kim, H. I.; Kurulugama, R. T.; May, J. C.; McLean, J. A.; Pagel, K.; Richardson, K.; Ridgeway, M. E.; Rosu, F.; Sobott, F.; Thalassinos, K.; Valentine, S. J.; Wyttenbach, T. Recommendations for Reporting Ion Mobility Mass Spectrometry Measurements. *Mass Spectrom. Rev.* **2019**, *38* (3), 291–320. https://doi.org/10.1002/mas.21585.

(9) Allen, S. J.; Bush, M. F. Radio-Frequency (Rf) Confinement in Ion Mobility Spectrometry: Apparent Mobilities and Effective Temperatures. *J. Am. Soc. Mass Spectrom.* **2016**, *27* (12), 2054–2063. https://doi.org/10.1007/s13361-016-1479-9.

(10) Bush, M. F.; Hall, Z.; Giles, K.; Hoyes, J.; Robinson, C. V.; Ruotolo, B. T. Collision Cross Sections of Proteins and Their Complexes: A Calibration Framework and Database for Gas-Phase Structural Biology. *Anal. Chem.* **2010**, *82* (22), 9557–9565. https://doi.org/10.1021/ac1022953.

(11) Allen, S. J.; Giles, K.; Gilbert, T.; Bush, M. F. Ion Mobility Mass Spectrometry of Peptide, Protein, and Protein Complex Ions Using a Radio-Frequency Confining Drift Cell. *The Analyst* **2016**, *141* (3), 884–891. https://doi.org/10.1039/C5AN02107C.

(12) Zercher, B. P.; Gozzo, T. A.; Wageman, A.; Bush, M. F. Enhancing the Depth of Analyses with Next-Generation Ion Mobility Experiments. *Annu. Rev. Anal. Chem.* **2023**, *16* (1), 27–48. https://doi.org/10.1146/annurev-anchem-091522-031329.

(13) Kemper, P. R.; Dupuis, N. F.; Bowers, M. T. A New, Higher Resolution, Ion Mobility Mass Spectrometer. *Int. J. Mass Spectrom.* **2009**, *287* (1–3), 46–57. https://doi.org/10.1016/j.ijms.2009.01.012.

(14) Giles, K.; Pringle, S. D.; Worthington, K. R.; Little, D.; Wildgoose, J. L.; Bateman, R. H. Applications of a Travelling Wave-based Radio-frequency-only Stacked Ring Ion Guide. *Rapid Commun. Mass Spectrom.* **2004**, *18* (20), 2401–2414. https://doi.org/10.1002/rcm.1641.

(15) Fernandez-Lima, F.; Kaplan, D. A.; Suetering, J.; Park, M. A. Gas-Phase Separation Using a Trapped Ion Mobility Spectrometer. *Int. J. Ion Mobil. Spectrom.* **2011**, *14* (2–3), 93–98. https://doi.org/10.1007/s12127-011-0067-8.

(16) Shvartsburg, A. A.; Smith, R. D. Fundamentals of Traveling Wave Ion Mobility Spectrometry. *Anal. Chem.* **2008**, *80* (24), 9689–9699. https://doi.org/10.1021/ac8016295.

(17) Richardson, K.; Langridge, D.; Giles, K. Fundamentals of Travelling Wave Ion Mobility Revisited: I. Smoothly Moving Waves. *Int. J. Mass Spectrom.* **2018**, *428*, 71–80. https://doi.org/10.1016/j.ijms.2018.03.007.

(18) Giles, K.; Wildgoose, J. L.; Langridge, D. J.; Campuzano, I. A Method for Direct Measurement of Ion Mobilities Using a Travelling Wave Ion Guide. *Int. J. Mass Spectrom.* **2010**, *298* (1–3), 10–16. https://doi.org/10.1016/j.ijms.2009.10.008.

(19) Mortensen, D. N.; Susa, A. C.; Williams, E. R. Collisional Cross-Sections with T-Wave Ion Mobility Spectrometry without Experimental Calibration. *J. Am. Soc. Mass Spectrom.* **2017**, *28* (7), 1282–1292. https://doi.org/10.1007/s13361-017-1669-0.

(20) Gelb, A. S.; Jarratt, R. E.; Huang, Y.; Dodds, E. D. A Study of Calibrant Selection in Measurement of Carbohydrate and Peptide Ion-Neutral Collision Cross Sections by Traveling Wave Ion Mobility Spectrometry. *Anal. Chem.* **2014**, *86* (22), 11396–11402. https://doi.org/10.1021/ac503379e.

(21) Bush, M. F.; Campuzano, I. D. G.; Robinson, C. V. Ion Mobility Mass Spectrometry of Peptide Ions: Effects of Drift Gas and Calibration Strategies. *Anal. Chem.* **2012**, *84* (16), 7124–7130. https://doi.org/10.1021/ac3014498.

(22) Gabelica, V.; Marklund, E. Fundamentals of Ion Mobility Spectrometry. *Curr. Opin. Chem. Biol.* **2018**, *42*, 51–59. https://doi.org/10.1016/j.cbpa.2017.10.022.

(23) Ruotolo, B. T.; Benesch, J. L. P.; Sandercock, A. M.; Hyung, S.-J.; Robinson, C. V. Ion Mobility–Mass Spectrometry Analysis of Large Protein Complexes. *Nat. Protoc.* **2008**, *3* (7), 1139–1152. https://doi.org/10.1038/nprot.2008.78.

(24) Richardson, K.; Langridge, D.; Dixit, S. M.; Ruotolo, B. T. An Improved Calibration Approach for Traveling Wave Ion Mobility Spectrometry: Robust, High-Precision Collision Cross Sections. *Anal. Chem.* **2021**, *93* (7), 3542–3550. https://doi.org/10.1021/acs.analchem.0c04948.

(25) Pringle, S. D.; Giles, K.; Wildgoose, J. L.; Williams, J. P.; Slade, S. E.; Thalassinos, K.; Bateman, R. H.; Bowers, M. T.; Scrivens, J. H. An Investigation of the Mobility Separation of Some Peptide and Protein Ions Using a New Hybrid Quadrupole/Travelling Wave IMS/Oa-ToF Instrument. *Int. J. Mass Spectrom.* **2007**, *261* (1), 1–12. https://doi.org/10.1016/j.ijms.2006.07.021.

(26) Giles, K.; Williams, J. P.; Campuzano, I. Enhancements in Travelling Wave Ion Mobility Resolution. *Rapid Commun. Mass Spectrom.* **2011**, *25* (11), 1559–1566. https://doi.org/10.1002/rcm.5013.

(27) Salbo, R.; Bush, M. F.; Naver, H.; Campuzano, I.; Robinson, C. V.; Pettersson, I.; Jørgensen, T. J. D.; Haselmann, K. F. Traveling-wave Ion Mobility Mass Spectrometry of Protein Complexes: Accurate Calibrated Collision Cross-sections of Human Insulin Oligomers. *Rapid Commun. Mass Spectrom.* **2012**, *26* (10), 1181–1193. https://doi.org/10.1002/rcm.6211.

(28) Domalain, V.; Hubert-Roux, M.; Tognetti, V.; Joubert, L.; Lange, C. M.; Rouden, J.; Afonso, C. Enantiomeric Differentiation of Aromatic Amino Acids Using Traveling Wave Ion Mobility-Mass Spectrometry. *Chem Sci* **2014**, *5* (8), 3234–3239. https://doi.org/10.1039/C4SC00443D.

(29) Hofmann, J.; Struwe, W. B.; Scarff, C. A.; Scrivens, J. H.; Harvey, D. J.; Pagel, K. Estimating Collision Cross Sections of Negatively Charged *N*- Glycans Using Traveling Wave Ion Mobility-Mass Spectrometry. *Anal. Chem.* **2014**, *86* (21), 10789–10795. https://doi.org/10.1021/ac5028353.

(30) Paglia, G.; Astarita, G. Metabolomics and Lipidomics Using Traveling-Wave Ion Mobility Mass Spectrometry. *Nat. Protoc.* **2017**, *12* (4), 797–813. https://doi.org/10.1038/nprot.2017.013.

(31) Hernández-Mesa, M.; D'Atri, V.; Barknowitz, G.; Fanuel, M.; Pezzatti, J.; Dreolin, N.; Ropartz, D.; Monteau, F.; Vigneau, E.; Rudaz, S.; Stead, S.; Rogniaux, H.; Guillarme, D.; Dervilly, G.; Le Bizec, B. Interlaboratory and Interplatform Study of Steroids Collision Cross Section by Traveling Wave Ion Mobility Spectrometry. *Anal. Chem.* **2020**, *92* (7), 5013–5022. https://doi.org/10.1021/acs.analchem.9b05247.

(32) Webb, I. K.; Garimella, S. V. B.; Tolmachev, A. V.; Chen, T.-C.; Zhang, X.; Norheim, R. V.; Prost, S. A.; LaMarche, B.; Anderson, G. A.; Ibrahim, Y. M.; Smith, R. D. Experimental Evaluation and Optimization of Structures for Lossless Ion Manipulations for Ion Mobility Spectrometry with Time-of-Flight Mass Spectrometry. *Anal. Chem.* **2014**, *86* (18), 9169–9176. https://doi.org/10.1021/ac502055e.

(33) Allen, S. J.; Eaton, R. M.; Bush, M. F. Analysis of Native-Like Ions Using Structures for Lossless Ion Manipulations. *Anal. Chem.* **2016**, *88* (18), 9118–9126. https://doi.org/10.1021/acs.analchem.6b02089.

(34) Webb, I. K.; Garimella, S. V. B.; Tolmachev, A. V.; Chen, T.-C.; Zhang, X.; Cox, J. T.; Norheim, R. V.; Prost, S. A.; LaMarche, B.; Anderson, G. A.; Ibrahim, Y. M.; Smith, R. D. Mobility-Resolved Ion Selection in Uniform Drift Field Ion Mobility Spectrometry/Mass Spectrometry: Dynamic Switching in Structures for Lossless Ion Manipulations. *Anal. Chem.* **2014**, *86* (19), 9632–9637. https://doi.org/10.1021/ac502139e.

(35) Chen, T.-C.; Ibrahim, Y. M.; Webb, I. K.; Garimella, S. V. B.; Zhang, X.; Hamid, A. M.; Deng, L.; Karnesky, W. E.; Prost, S. A.; Sandoval, J. A.; Norheim, R. V.; Anderson, G. A.;

Tolmachev, A. V.; Baker, E. S.; Smith, R. D. Mobility-Selected Ion Trapping and Enrichment Using Structures for Lossless Ion Manipulations. *Anal. Chem.* **2016**, *88* (3), 1728–1733. https://doi.org/10.1021/acs.analchem.5b03910.

(36) Hamid, A. M.; Ibrahim, Y. M.; Garimella, S. V. B.; Webb, I. K.; Deng, L.; Chen, T.-C.; Anderson, G. A.; Prost, S. A.; Norheim, R. V.; Tolmachev, A. V.; Smith, R. D. Characterization of Traveling Wave Ion Mobility Separations in Structures for Lossless Ion Manipulations. *Anal. Chem.* **2015**, *87* (22), 11301–11308. https://doi.org/10.1021/acs.analchem.5b02481.

(37) Hamid, A. M.; Garimella, S. V. B.; Ibrahim, Y. M.; Deng, L.; Zheng, X.; Webb, I. K.; Anderson, G. A.; Prost, S. A.; Norheim, R. V.; Tolmachev, A. V.; Baker, E. S.; Smith, R. D. Achieving High Resolution Ion Mobility Separations Using Traveling Waves in Compact Multiturn Structures for Lossless Ion Manipulations. *Anal. Chem.* **2016**, *88* (18), 8949–8956. https://doi.org/10.1021/acs.analchem.6b01914.

(38) Smyth, M. S. X Ray Crystallography. *Mol. Pathol.* **2000**, *53* (1), 8–14. https://doi.org/10.1136/mp.53.1.8.

(39) Carroni, M.; Saibil, H. R. Cryo Electron Microscopy to Determine the Structure of Macromolecular Complexes. *Methods* **2016**, *95*, 78–85. https://doi.org/10.1016/j.ymeth.2015.11.023.

(40) Zhang, Y.; Fonslow, B. R.; Shan, B.; Baek, M.-C.; Yates, J. R. Protein Analysis by Shotgun/Bottom-up Proteomics. *Chem. Rev.* **2013**, *113* (4), 2343–2394. https://doi.org/10.1021/cr3003533.

(41) Donnelly, D. P.; Rawlins, C. M.; DeHart, C. J.; Fornelli, L.; Schachner, L. F.; Lin, Z.; Lippens, J. L.; Aluri, K. C.; Sarin, R.; Chen, B.; Lantz, C.; Jung, W.; Johnson, K. R.;

Koller, A.; Wolff, J. J.; Campuzano, I. D. G.; Auclair, J. R.; Ivanov, A. R.; Whitelegge, J. P.; Paša-Tolić, L.; Chamot-Rooke, J.; Danis, P. O.; Smith, L. M.; Tsybin, Y. O.; Loo, J. A.; Ge, Y.; Kelleher, N. L.; Agar, J. N. Best Practices and Benchmarks for Intact Protein Analysis for Top-down Mass Spectrometry. *Nat. Methods* **2019**, *16* (7), 587–594. https://doi.org/10.1038/s41592-019-0457-0.

(42) Shuken, S. R. An Introduction to Mass Spectrometry-Based Proteomics. *J. Proteome Res.* **2023**, *22* (7), 2151–2171. https://doi.org/10.1021/acs.jproteome.2c00838.

(43) Yamashita, M.; Fenn, J. B. Electrospray Ion Source. Another Variation on the Free-Jet Theme. *J. Phys. Chem.* **1984**, *88* (20), 4451–4459. https://doi.org/10.1021/j150664a002.

(44) Loo, J. A.; Udseth, H. R.; Smith, R. D. Peptide and Protein Analysis by Electrospray Ionization-Mass Spectrometry and Capillary Electrophoresis-Mass Spectrometry. *Anal. Biochem.* **1989**, *179* (2), 404–412. https://doi.org/10.1016/0003-2697(89)90153-X.

(45) Kebarle, P.; Verkerk, U. H. Electrospray: From Ions in Solution to Ions in the Gas Phase, What We Know Now. *Mass Spectrom. Rev.* **2009**, *28* (6), 898–917. https://doi.org/10.1002/mas.20247.

(46) Juraschek, R.; Dülcks, T.; Karas, M. Nanoelectrospray—More than Just a Minimized-Flow Electrospray Ionization Source. *J. Am. Soc. Mass Spectrom.* **1999**, *10* (4), 300–308. https://doi.org/10.1016/S1044-0305(98)00157-3.

(47) Heuvel, R. H. V. D.; Heck, A. J. Native Protein Mass Spectrometry: From Intact Oligomers to Functional Machineries. *Curr. Opin. Chem. Biol.* **2004**, *8* (5), 519–526. https://doi.org/10.1016/j.cbpa.2004.08.006.

(48) Pacholarz, K. J.; Peters, S. J.; Garlish, R. A.; Henry, A. J.; Taylor, R. J.; Humphreys, D. P.; Barran, P. E. Molecular Insights into the Thermal Stability of mAbs with Variable-

Temperature Ion-Mobility Mass Spectrometry. *ChemBioChem* **2016**, *17* (1), 46–51. https://doi.org/10.1002/cbic.201500574.

(49) Jeanne Dit Fouque, K.; Fernandez-Lima, F. Following Structural Changes by Thermal Denaturation Using Trapped Ion Mobility Spectrometry–Mass Spectrometry. *J. Phys. Chem. B* **2020**, *124* (29), 6257–6265. https://doi.org/10.1021/acs.jpcb.0c04276.

(50) El-Baba, T. J.; Woodall, D. W.; Raab, S. A.; Fuller, D. R.; Laganowsky, A.; Russell, D. H.; Clemmer, D. E. Melting Proteins: Evidence for Multiple Stable Structures upon Thermal Denaturation of Native Ubiquitin from Ion Mobility Spectrometry-Mass Spectrometry Measurements. *J. Am. Chem. Soc.* **2017**, *139* (18), 6306–6309. https://doi.org/10.1021/jacs.7b02774.

(51) McCabe, J. W.; Shirzadeh, M.; Walker, T. E.; Lin, C.-W.; Jones, B. J.; Wysocki, V. H.; Barondeau, D. P.; Clemmer, D. E.; Laganowsky, A.; Russell, D. H. Variable-Temperature Electrospray Ionization for Temperature-Dependent Folding/Refolding Reactions of Proteins and Ligand Binding. *Anal. Chem.* **2021**, *93* (18), 6924–6931. https://doi.org/10.1021/acs.analchem.1c00870.

(52) Köhler, M.; Marchand, A.; Hentzen, N. B.; Egli, J.; Begley, A. I.; Wennemers, H.; Zenobi, R. Temperature-Controlled Electrospray Ionization Mass Spectrometry as a Tool to Study Collagen Homo- and Heterotrimers. *Chem. Sci.* **2019**, *10* (42), 9829–9835. https://doi.org/10.1039/C9SC03248G.

(53) Hyung, S.-J.; Robinson, C. V.; Ruotolo, B. T. Gas-Phase Unfolding and Disassembly Reveals Stability Differences in Ligand-Bound Multiprotein Complexes. *Chem. Biol.* **2009**, *16* (4), 382–390. https://doi.org/10.1016/j.chembiol.2009.02.008.

(54) Lai, A. L.; Clerico, E. M.; Blackburn, M. E.; Patel, N. A.; Robinson, C. V.; Borbat, P. P.; Freed, J. H.; Gierasch, L. M. Key Features of an Hsp70 Chaperone Allosteric Landscape Revealed by Ion-Mobility Native Mass Spectrometry and Double Electron-Electron Resonance. *J. Biol. Chem.* **2017**, *292* (21), 8773–8785. https://doi.org/10.1074/jbc.M116.770404.

(55) Liu, Y.; Cong, X.; Liu, W.; Laganowsky, A. Characterization of Membrane Protein–Lipid Interactions by Mass Spectrometry Ion Mobility Mass Spectrometry. *J. Am. Soc. Mass Spectrom.* **2017**, *28* (4), 579–586. https://doi.org/10.1007/s13361-016-1555-1.

(56) Song, Y.; Nelp, M. T.; Bandarian, V.; Wysocki, V. H. Refining the Structural Model of a Heterohexameric Protein Complex: Surface Induced Dissociation and Ion Mobility Provide Key Connectivity and Topology Information. *ACS Cent. Sci.* **2015**, *1* (9), 477–487. https://doi.org/10.1021/acscentsci.5b00251.

(57) Pont, L.; Benavente, F.; Vilaseca, M.; Giménez, E.; Sanz-Nebot, V. Characterisation of Serum Transthyretin by Electrospray Ionisation-Ion Mobility Mass Spectrometry: Application to Familial Amyloidotic Polyneuropathy Type I (FAP-I). *Talanta* **2015**, *144*, 1216–1224. https://doi.org/10.1016/j.talanta.2015.07.079.

(58) Smith, D. P.; Radford, S. E.; Ashcroft, A. E. Elongated Oligomers in β_2 -Microglobulin Amyloid Assembly Revealed by Ion Mobility Spectrometry-Mass Spectrometry. *Proc. Natl. Acad. Sci.* **2010**, *107* (15), 6794–6798. https://doi.org/10.1073/pnas.0913046107.

(59) Deng, L.; Ibrahim, Y. M.; Hamid, A. M.; Garimella, S. V. B.; Webb, I. K.; Zheng, X.; Prost, S. A.; Sandoval, J. A.; Norheim, R. V.; Anderson, G. A.; Tolmachev, A. V.; Baker, E. S.; Smith, R. D. Ultra-High Resolution Ion Mobility Separations Utilizing Traveling Waves in

a 13 m Serpentine Path Length Structures for Lossless Ion Manipulations Module. *Anal. Chem.* **2016**, *88* (18), 8957–8964. https://doi.org/10.1021/acs.analchem.6b01915.

(60) Deng, L.; Webb, I. K.; Garimella, S. V. B.; Hamid, A. M.; Zheng, X.; Norheim, R. V.; Prost, S. A.; Anderson, G. A.; Sandoval, J. A.; Baker, E. S.; Ibrahim, Y. M.; Smith, R. D. Serpentine Ultralong Path with Extended Routing (SUPER) High Resolution Traveling Wave Ion Mobility-MS Using Structures for Lossless Ion Manipulations. *Anal. Chem.* **2017**, *89* (8), 4628–4634. https://doi.org/10.1021/acs.analchem.7b00185.

(61) Garimella, S. V. B.; Hamid, A. M.; Deng, L.; Ibrahim, Y. M.; Webb, I. K.; Baker, E. S.; Prost, S. A.; Norheim, R. V.; Anderson, G. A.; Smith, R. D. Squeezing of Ion Populations and Peaks in Traveling Wave Ion Mobility Separations and Structures for Lossless Ion Manipulations Using Compression Ratio Ion Mobility Programming. *Anal. Chem.* **2016**, *88* (23), 11877–11885. https://doi.org/10.1021/acs.analchem.6b03660.

(62) Koeniger, S. L.; Merenbloom, S. I.; Clemmer, D. E. Evidence for Many Resolvable Structures within Conformation Types of Electrosprayed Ubiquitin Ions. *J. Phys. Chem. B* **2006**, *110* (13), 7017–7021. https://doi.org/10.1021/jp056165h.

(63) Koeniger, S. L.; Merenbloom, S. I.; Valentine, S. J.; Jarrold, M. F.; Udseth, H. R.; Smith, R. D.; Clemmer, D. E. An IMS−IMS Analogue of MS−MS. *Anal. Chem.* **2006**, *78* (12), 4161–4174. https://doi.org/10.1021/ac051060w.

(64) Merenbloom, S. I.; Koeniger, S. L.; Valentine, S. J.; Plasencia, M. D.; Clemmer, D. E. IMS−IMS and IMS−IMS−IMS/MS for Separating Peptide and Protein Fragment Ions. *Anal. Chem.* **2006**, *78* (8), 2802–2809. https://doi.org/10.1021/ac052208e.

(65) Li, H.; Bendiak, B.; Siems, W. F.; Gang, D. R.; Hill, H. H. Carbohydrate Structure Characterization by Tandem Ion Mobility Mass Spectrometry (IMMS)^2. *Anal. Chem.* **2013**, *85* (5), 2760–2769. https://doi.org/10.1021/ac303273z.

(66) Allen, S. J.; Eaton, R. M.; Bush, M. F. Structural Dynamics of Native-Like Ions in the Gas Phase: Results from Tandem Ion Mobility of Cytochrome *c*. *Anal. Chem.* **2017**, *89* (14), 7527–7534. https://doi.org/10.1021/acs.analchem.7b01234.

(67) Zercher, B. P.; Hong, S.; Roush, A. E.; Feng, Y.; Bush, M. F. Are the Gas-Phase Structures of Molecular Elephants Enduring or Ephemeral? Results from Time-Dependent, Tandem Ion Mobility. *Anal. Chem.* **2023**, *95* (25), 9589–9597. https://doi.org/10.1021/acs.analchem.3c01222.

(68) Dyukova, I.; Ben Faleh, A.; Warnke, S.; Yalovenko, N.; Yatsyna, V.; Bansal, P.; Rizzo, T. R. A New Approach for Identifying Positional Isomers of Glycans Cleaved from Monoclonal Antibodies. *The Analyst* **2021**, *146* (15), 4789–4795. https://doi.org/10.1039/D1AN00780G.

(69) Bansal, P.; Yatsyna, V.; AbiKhodr, A. H.; Warnke, S.; Ben Faleh, A.; Yalovenko, N.; Wysocki, V. H.; Rizzo, T. R. Using SLIM-Based IMS-IMS Together with Cryogenic Infrared Spectroscopy for Glycan Analysis. *Anal. Chem.* **2020**, *92* (13), 9079–9085. https://doi.org/10.1021/acs.analchem.0c01265.

(70) Bansal, P.; Ben Faleh, A.; Warnke, S.; Rizzo, T. R. Identification of *N* -Glycan Positional Isomers by Combining IMS and Vibrational Fingerprinting of Structurally Determinant CID Fragments. *The Analyst* **2022**, *147* (4), 704–711. https://doi.org/10.1039/D1AN01861B.

(71) Pellegrinelli, R. P.; Yue, L.; Carrascosa, E.; Ben Faleh, A.; Warnke, S.; Bansal, P.; Rizzo, T. R. A New Strategy Coupling Ion-Mobility-Selective CID and Cryogenic IR Spectroscopy to Identify Glycan Anomers. *J. Am. Soc. Mass Spectrom.* **2022**, *33* (5), 859–864. https://doi.org/10.1021/jasms.2c00043.

(72) Ben Faleh, A.; Warnke, S.; Bansal, P.; Pellegrinelli, R. P.; Dyukova, I.; Rizzo, T. R. Identification of Mobility-Resolved *N* -Glycan Isomers. *Anal. Chem.* **2022**, *94* (28), 10101–10108. https://doi.org/10.1021/acs.analchem.2c01181.

(73) Kedia, K.; Harris, R.; Ekroos, K.; Moser, K. W.; DeBord, D.; Tiberi, P.; Goracci, L.; Zhang, N. R.; Wang, W.; Spellman, D. S.; Bateman, K. Investigating Performance of the SLIM-Based High Resolution Ion Mobility Platform for Separation of Isomeric Phosphatidylcholine Species. *J. Am. Soc. Mass Spectrom.* **2023**, *34* (10), 2176–2186. https://doi.org/10.1021/jasms.3c00157.

(74) Dykstra, A. B.; Lubinsky, T. G.; Vitrac, H.; Campuzano, I. D. G.; Bondarenko, P. V.; Simone, A. R. Utilization of Liquid Chromatography–Mass Spectrometry and High-Resolution Ion Mobility–Mass Spectrometry to Characterize Therapeutically Relevant Peptides with Asparagine Deamidation and Isoaspartate. *Anal. Chem.* **2025**, *97* (1), 749–757. https://doi.org/10.1021/acs.analchem.4c05246.

(75) Giles, K.; Ujma, J.; Wildgoose, J.; Pringle, S.; Richardson, K.; Langridge, D.; Green, M. A Cyclic Ion Mobility-Mass Spectrometry System. *Anal. Chem.* **2019**, *91* (13), 8564–8573. https://doi.org/10.1021/acs.analchem.9b01838.

(76) Wyttenbach, T.; Kemper, P. R.; Bowers, M. T. Design of a New Electrospray Ion Mobility Mass Spectrometer. *Int. J. Mass Spectrom.* **2001**, *212* (1–3), 13–23. https://doi.org/10.1016/S1387-3806(01)00517-6.

(77) Garimella, S. V. B.; Ibrahim, Y. M.; Webb, I. K.; Tolmachev, A. V.; Zhang, X.; Prost, S. A.; Anderson, G. A.; Smith, R. D. Simulation of Electric Potentials and Ion Motion in Planar Electrode Structures for Lossless Ion Manipulations (SLIM). *J. Am. Soc. Mass Spectrom.* **2014**, *25* (11), 1890–1896. https://doi.org/10.1007/s13361-014-0976-y.

(78) Lynn, E. C.; Chung, M.-C.; Han, C.-C. Characterizing the Transmission Properties of an Ion Funnel. *Rapid Commun. Mass Spectrom.* **2000**, *14* (22), 2129–2134. https://doi.org/10.1002/1097-0231(20001130)14:22<2129::AID-RCM144>3.0.CO;2-M.

(79) Tolmachev, A. V.; Webb, I. K.; Ibrahim, Y. M.; Garimella, S. V. B.; Zhang, X.; Anderson, G. A.; Smith, R. D. Characterization of Ion Dynamics in Structures for Lossless Ion Manipulations. *Anal. Chem.* **2014**, *86* (18), 9162–9168. https://doi.org/10.1021/ac502054p.

(80) Eaton, R. M.; Allen, S. J.; Bush, M. F. Principles of Ion Selection, Alignment, and Focusing in Tandem Ion Mobility Implemented Using Structures for Lossless Ion Manipulations (SLIM). *J. Am. Soc. Mass Spectrom.* **2019**, *30* (6), 1115–1125. https://doi.org/10.1007/s13361-019-02170-1.

(81) Attah, I. K.; Garimella, S. V. B.; Webb, I. K.; Nagy, G.; Norheim, R. V.; Schimelfenig, C. E.; Ibrahim, Y. M.; Smith, R. D. Dual Polarity Ion Confinement and Mobility Separations. *J. Am. Soc. Mass Spectrom.* **2019**, *30* (6), 967–976. https://doi.org/10.1007/s13361-019-02138-1.

(82) Li, A.; Garimella, S. V. B.; Ibrahim, Y. M. A Simulation Study of the Influence of the Traveling Wave Patterns on Ion Mobility Separations in Structures for Lossless Ion Manipulations. *The Analyst* **2020**, *145* (1), 240–248. https://doi.org/10.1039/C9AN01509D.

(83) Eldrid, C.; Ben-Younis, A.; Ujma, J.; Britt, H.; Cragnolini, T.; Kalfas, S.; Cooper-Shepherd, D.; Tomczyk, N.; Giles, K.; Morris, M.; Akter, R.; Raleigh, D.; Thalassinos, K. Cyclic Ion

Mobility–Collision Activation Experiments Elucidate Protein Behavior in the Gas Phase. *J. Am. Soc. Mass Spectrom.* **2021**, *32* (6), 1545–1552. https://doi.org/10.1021/jasms.1c00018.

(84) Deslignière, E.; Ollivier, S.; Ehkirch, A.; Martelet, A.; Ropartz, D.; Lechat, N.; Hernandez-Alba, O.; Menet, J.-M.; Clavier, S.; Rogniaux, H.; Genet, B.; Cianférani, S. Combination of IM-Based Approaches to Unravel the Coexistence of Two Conformers on a Therapeutic Multispecific mAb. *Anal. Chem.* **2022**, *94* (22), 7981–7989. https://doi.org/10.1021/acs.analchem.2c00928.

(85) Peterson, T. L.; Nagy, G. Toward Sequencing the Human Milk Glycome: High-Resolution Cyclic Ion Mobility Separations of Core Human Milk Oligosaccharide Building Blocks. *Anal. Chem.* **2021**, *93* (27), 9397–9407. https://doi.org/10.1021/acs.analchem.1c00942.

(86) Ollivier, S.; Tarquis, L.; Fanuel, M.; Li, A.; Durand, J.; Laville, E.; Potocki-Veronese, G.; Ropartz, D.; Rogniaux, H. Anomeric Retention of Carbohydrates in Multistage Cyclic Ion Mobility (IMS^n): De Novo Structural Elucidation of Enzymatically Produced Mannosides. *Anal. Chem.* **2021**, *93* (15), 6254–6261. https://doi.org/10.1021/acs.analchem.1c00673.

(87) Ollivier, S.; Fanuel, M.; Rogniaux, H.; Ropartz, D. Molecular Networking of High-Resolution Tandem Ion Mobility Spectra: A Structurally Relevant Way of Organizing Data in Glycomics? *Anal. Chem.* **2021**, *93* (31), 10871–10878. https://doi.org/10.1021/acs.analchem.1c01244.

(88) Shaw, J. B.; Cooper-Shepherd, D. A.; Hewitt, D.; Wildgoose, J. L.; Beckman, J. S.; Langridge, J. I.; Voinov, V. G. Enhanced Top-Down Protein Characterization with Electron Capture Dissociation and Cyclic Ion Mobility Spectrometry. *Anal. Chem.* **2022**, *94* (9), 3888–3896. https://doi.org/10.1021/acs.analchem.1c04870.

(89) May, J. C.; Leaptrot, K. L.; Rose, B. S.; Moser, K. L. W.; Deng, L.; Maxon, L.; DeBord, D.; McLean, J. A. Resolving Power and Collision Cross Section Measurement Accuracy of a Prototype High-Resolution Ion Mobility Platform Incorporating Structures for Lossless Ion Manipulation. *J. Am. Soc. Mass Spectrom.* **2021**, *32* (4), 1126–1137. https://doi.org/10.1021/jasms.1c00056.

(90) Aderorho, R.; Lucas, S. W.; Chouinard, C. D. Separation and Characterization of Synthetic Cannabinoid Metabolite Isomers Using SLIM High-Resolution Ion Mobility-Tandem Mass Spectrometry (HRIM-MS/MS). *J. Am. Soc. Mass Spectrom.* **2024**, *35* (3), 582–589. https://doi.org/10.1021/jasms.3c00419.

(91) Kingsley, S.; Hoover, M.; Pettit-Bacovin, T.; Sawyer, A. R.; Chouinard, C. D. SLIM-Based High-Resolution Ion Mobility Reveals New Structural Insights into Isomeric Vitamin D Metabolites and Their Isotopologues. *J. Am. Soc. Mass Spectrom.* **2024**, *35* (11), 2650–2658. https://doi.org/10.1021/jasms.4c00116.

(92) Fawaz, M.; Sun, C.; Feng, Y.; Qirjollari, A.; Josien, H.; DeBord, D.; Simone, A.; Williamson, D. L.; Pearson, K.; Gonzalez, R. J.; Vasicek, L.; Cancilla, M. T.; Wang, W.; Spellman, D. S.; Kedia, K. Leveraging High-Resolution Ion Mobility-Mass Spectrometry for Cyclic Peptide Soft Spot Identification. *J. Am. Soc. Mass Spectrom.* **2024**, *35* (11), 2596–2607. https://doi.org/10.1021/jasms.4c00109.

(93) Kinlein, Z. R.; Anderson, G. A.; Clowers, B. H. Accelerating Prototyping Experiments for Traveling Wave Structures for Lossless Ion Manipulations. *Talanta* **2022**, *244*, 123446. https://doi.org/10.1016/j.talanta.2022.123446.

(94) Greer, C.; Kinlein, Z.; Clowers, B. H. SLIM Tricks: Tools, Concepts, and Strategies for the Development of Planar Ion Guides. *J. Am. Soc. Mass Spectrom.* **2023**, *34* (8), 1715–1723. https://doi.org/10.1021/jasms.3c00163.

(95) Siems, W. F.; Viehland, L. A.; Hill, H. H. Correcting the Fundamental Ion Mobility Equation for Field Effects. *The Analyst* **2016**, *141* (23), 6396–6407. https://doi.org/10.1039/C6AN01353H.

(96) Chen, S.-H.; Russell, D. H. How Closely Related Are Conformations of Protein Ions Sampled by IM-MS to Native Solution Structures? *J. Am. Soc. Mass Spectrom.* **2015**, *26* (9), 1433–1443. https://doi.org/10.1007/s13361-015-1191-1.

(97) Morsa, D.; Gabelica, V.; De Pauw, E. Effective Temperature of Ions in Traveling Wave Ion Mobility Spectrometry. *Anal. Chem.* **2011**, *83* (14), 5775–5782. https://doi.org/10.1021/ac201509p.

(98) Merenbloom, S. I.; Flick, T. G.; Williams, E. R. How Hot Are Your Ions in TWAVE Ion Mobility Spectrometry? *J. Am. Soc. Mass Spectrom.* **2012**, *23* (3), 553–562. https://doi.org/10.1007/s13361-011-0313-7.

(99) Morsa, D.; Gabelica, V.; De Pauw, E. Fragmentation and Isomerization Due to Field Heating in Traveling Wave Ion Mobility Spectrometry. *J. Am. Soc. Mass Spectrom.* **2014**, *25* (8), 1384–1393. https://doi.org/10.1007/s13361-014-0909-9.

(100) Larriba-Andaluz, C.; Prell, J. S. Fundamentals of Ion Mobility in the Free Molecular Regime. Interlacing the Past, Present and Future of Ion Mobility Calculations. *Int. Rev. Phys. Chem.* **2020**, *39* (4), 569–623. https://doi.org/10.1080/0144235X.2020.1826708.

(101) Prell, J. S. Modeling Collisional Kinetic Energy Damping, Heating, and Cooling of Ions in Mass Spectrometers: A Tutorial Perspective. *Int. J. Mass Spectrom.* **2024**, *504*, 117290. https://doi.org/10.1016/j.ijms.2024.117290.

Chapter 2. SLIMPHONY: A New SLIM-Based Instrument That Orchestrates Complex Ion Mobility–Mass Spectrometry Experiments

2.1 Abstract

The inherent heterogeneity of biological macromolecules offers a unique challenge for analysis. The combination of ion mobility spectrometry (IMS) and mass spectrometry (MS) is sensitive to the size, shape, and dynamics of, for example, proteins and their complexes. Combining multiple dimensions of ion mobility and mass spectrometry (IM-IM-MS) while leveraging unique gas-phase ion chemistry between dimensions has particularly increased the information content of protein structural studies. Here, we introduce a new IMS instrument, SLIMPHONY, built using the Structures for Lossless Ion Manipulations (SLIM) architecture. SLIMPHONY is unique in that eight independently controlled traveling-wave regions work in concert to enable complex, multidimensional separations. Separation of a mixture of proteins and protein complexes is demonstrated through a single-dimension IM-MS experiment, and the peak-to-peak resolution of commercial tuning mix ions is found to increase roughly with the square root of the separation length. In harmony with prior work, ion selection and trapping between dimensions probes the gas-phase unfolding of a subpopulation of ubiquitin ions. Finally, by varying the guard potential used to confine ions during trapping, we demonstrate tunable activation of ubiquitin subpopulations. With its ability to simultaneously control the extent of ion activation and length of separation, SLIMPHONY represents a flexible platform for conducting novel studies of protein structure and unfolding.

2.2 Introduction

Large biomolecules often exhibit heterogeneity and dynamism in structure, assembly, and intermolecular interactions, features that challenge conventional structural biology methods but can be tractable to mass spectrometry (MS). For example, proteins and protein complexes can adopt a range of oligomeric states with varying biological activities and functions;[1] native MS is exquisitely sensitive to this property.[2] In ion mobility spectrometry (IMS), gas-phase ions are subjected to an electric field and collisions with neutral background gas molecules. This results in separation based on size, charge, and shape. Ion mobility (IM) provides orthogonal information to MS by resolving different structures with the same mass-to-charge ratio (m/z) that are undifferentiated by MS alone.[3–6] For example, IM-MS has been used to characterize conformational states of full-length ubiquilin-2 protein ions under different conditions, revealing that more compact structures are favored under conditions associated with normal function and that extended structures become populated under conditions associated with disease.[7] IM-MS has proved useful for probing many aspects of protein structural dynamics, including temperature-induced folding and unfolding,[8–12] responses to intermolecular interactions,[13–15] and oligomerization processes.[16–18]

Advances in IM methods have sought to increase resolving power,[19] which ideally scales with the square root of separation length.[20] Conventional drift tubes consist of a series of concentric ring electrodes connected by a voltage divider network, resulting in ions experiencing a constant applied electric field. Separation paths are largely limited to linear shapes, and separation length is limited by input voltage needed to establish an electric field. Trapped IMS (TIMS) is an alternative approach in which a gradient electric field is applied against a directional gas flow to trap and subsequently elute ions according to mobility; resolution in a

TIMS device depends on the electric field ramp rate as opposed to separation length, enabling performance improvements via tuning of the applied potentials.[21] Alternative electrode architectures in combination with electrodynamic fields allow for non-linear paths and lower operation voltages,[19] making long separations more feasible. Structures for Lossless Ion Manipulations (SLIM), in which electrodes are deposited on a mirrored pair of printed circuit boards, have used serpentine paths and switches enabling multiple passes to increase resolution up to 30-fold compared to a 90-cm drift tube separation.[22,23] The Waters Cyclic IMS device contains a racetrack-like structure composed of electrodes arranged in a loop with a short switching region used to inject and remove ions from the separation region. By sending ions around the cyclical path multiple times, separation lengths of hundreds of meters can be achieved.[20] Both of these strategies rely on traveling-wave (TW) potentials, in which repeating pulses of moderate voltage are propagated down the length of the drift region to drive ion motion.[24] TIMS, traveling-wave IMS (TWIMS), SLIM, and cyclic IMS have helped to push the boundaries of achievable resolving powers, resulting in previously unrealized separations of monoclonal antibody conformers,[25,26] glycan isomers,[27,28] and isotopic isomers.[29]

Developments in tandem IM have magnified the utility of IM to structural biology. Tandem IM involves sequential IM separations between which ion populations can be selected according to their mobilities and further manipulated by activation and other strategies. Clemmer and coworkers combined multiple drift tubes separated by ion funnels to study different conformations of protein ions[30] and to collisionally fragment[31,32] and unfold[31] protein and peptide ions between dimensions of IM. Hill and colleagues coupled a drift tube with a TWIMS device capable of collision-induced dissociation to study isomeric oligosaccharides.[33] Other implementations of tandem IM have included laser excitation[34] and storage in the trapping region

of an ion funnel that was resistively heated[35] between IM dimensions. The commercialization of the Waters Cyclic IMS instrument has given rise to an explosion of applications for tandem IM, including studies of different structural forms of a monoclonal antibody,[26] an amyloidogenic polypeptide,[36] and a protein associated with Parkinson's disease[37] as well as progress in de novo sequencing of complex glycans.[38–40] Notably, tandem cyclic IM separations have yielded the first evidence for a single enzyme capable of synthesizing oligosaccharides with either α- or β-glycosidic bonds.[38] TIMS has also been employed for tandem IM;[41] tandem TIMS has been applied to top-down sequencing of protein and protein complex ions to provide structural information about the fragments used for sequencing.[42–44]

Next-generation IM instrumentation has increased experimental flexibility and information content.[19] New geometries facilitate ion accumulation and selection off-axis from transmission, allowing increasingly complex experiments. Serpentine electrode paths have drastically reduced physical instrument footprints, making them more practical in laboratory settings. Tandem IM has benefitted from the non-linear electrode paths enabled by SLIM and has been used to probe the structural evolution of gas-phase biomolecular ions. We have previously reported an increase in collision cross section (CCS) of monomeric protein ions with increasing time trapped between the first and second dimensions of electrostatic tandem IM separations, while no changes in CCS were observed for larger protein complex ions under the same conditions.[45,46] TW-SLIM has also been combined with collision-induced dissociation and cryogenic infrared spectroscopy to identify novel glycans, whose high rates of isomerism and heterogeneity resist characterization by conventional methods, including comparison to known standards.[47–51] Developments in tandem IM and hyphenated techniques center around finding

new strategies to isolate and manipulate species of biomolecular interest from matrices that are complex, heterogeneous, and challenging to analyze.

Here, we introduce SLIMPHONY, which uses 8 independently controlled TW-SLIM regions to enable complex, multi-step experiments. Two 82-cm antiparallel separation regions connected by short, perpendicular segments enable ion selection and storage at two distinct locations. Ions are separated through multiple passes to vary the length of each separation. To demonstrate the functionality of this platform, time- and voltage-dependent tandem IM separations are employed to probe the structural evolution of native-like protein ions. Tandem and multi-pass capabilities are combined within the same experiment, demonstrating our ability to manipulate ion populations in multiple ways simultaneously.

2.3 Methods

2.3.1 Sample Preparation

E. coli-derived human ubiquitin was purchased from R&D Systems (Minneapolis, MN). Bovine serum albumin, *beta*-lactoglobulin from bovine milk, and avidin from egg white were purchased from Sigma-Aldrich (St. Louis, MO). Protein sample solutions were prepared to concentrations between 5 and 35 μM in aqueous 200 mM ammonium acetate at pH 7.0. All protein samples except for ubiquitin were buffer exchanged using Micro Bio-Spin 6 columns (Bio-Rad, Hercules, CA) equilibrated with aqueous 200 mM aqueous ammonium acetate at pH 7.0. A commercial tuning mixture for liquid chromatography-mass spectrometry instruments was purchased from Agilent (Santa Clara, CA). The tuning mixture was diluted 1:1 in deionized water prior to analysis.

2.3.2 Instrumentation

The new IM system is assembled upstream of a Waters Q-Tof Premier mass spectrometer (Wilmslow, U.K.) and is contained within a set of custom aluminum chambers. Ions are generated using nanoelectrospray ionization[52] and introduced to the vacuum system through a stainless steel capillary with a 0.25 mm inner diameter that was held at 80 °C. The stainless steel capillary directs ions into a series of ion funnels, as described previously.[53] Ions first enter an ion funnel trap[54] used as a funnel only, then pass through a 1.85 mm conductance limit and enter a rectangular ion funnel.[55] After transport and spatial focusing through the rectangular ion funnel, the ion beam travels between two mirror-image SLIM boards, whose electrode path and operation are described below. A circular ion funnel[56] is positioned after the SLIM boards and transmits ions into the mass spectrometer via a stacked-ring ion guide. This interface has also been described previously.[57] High-purity N_2 gas is introduced to the aluminum chambers via a mass flow controller. The chamber containing the ion funnel trap is separated from the chamber containing the SLIM boards by a conductance limit, and the operating pressures in each chamber are ~3.00 Torr and ~3.05 Torr, respectively.

The SLIM boards are custom designed and fabricated printed circuit boards containing a series of electrodes arranged in a path as shown in Figure 2.1A. Two mirror-image boards, electrode sides facing, are separated by 6.35 mm using acetal spacers. The electrodes are arrayed in repeating TW units flanked by guard electrodes on both sides. The TW units consist of five rows of eight DC electrodes that propagate the traveling waves; the DC electrodes are interleaved with alternating polarity rf electrodes for ion confinement. This arrangement of electrodes was modeled after designs reported by Smith and coworkers[58] and by Rizzo and coworkers.[59] The electrode path on each board is divided into eight separate regions, the

traveling wave applied to each of which can be controlled independently. Within each region, every eighth electrode is connected electrically, allowing a series of traveling waves to be propagated by applying a potential between +1 V and +50 V to four adjacent TW lines, applying the same magnitude negative potential to the four subsequent TW lines, and shifting the phase of this pattern by 45 ° at a defined frequency.

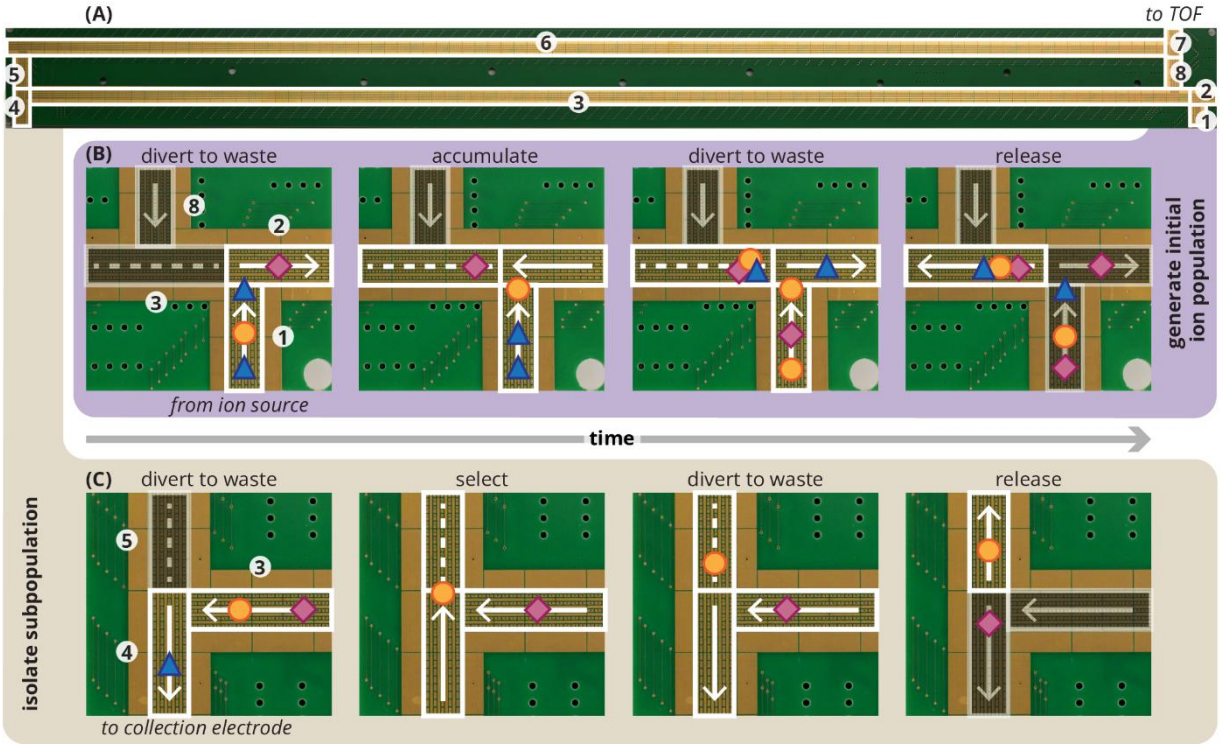

Figure 2.1. (A) Photograph of the bottom SLIM board used in this instrument and descriptions of how regions of this board are used in an IM-IM-MS experiment. "^{n}R" denotes the *n*th TW region, as indicated by the numbers 1-8. The first dimension of IM (^{1}D) consists of ^{3}R and the portion of ^{4}R ions traverse between ^{3}R and ^{5}R. The second dimension of IM (^{2}D) consists of ^{5}R, the portion of ^{6}R ions traverse between ^{5}R and ^{7}R, and ^{7}R. (B) Close-up views of ^{1}R, ^{2}R, ^{3}R, and ^{8}R, showing the sequence of steps used to generate an initial population of ions. (C)

Close-up views of ^{3}R, ^{4}R, and ^{5}R, showing the sequence of steps used to mobility-select a subpopulation of ions between dimensions in a tandem IM separation. White arrows indicate the direction of the traveling wave in each region during each step of ion accumulation. Dashed lines indicate that the wave is stationary. Blue triangles, orange circles, and pink squares represent ions of high, intermediate, and low mobility, respectively.

2.3.3 Voltage Control

Three Modular Intelligent Power Sources (MIPS, GAA Custom Electronics, Kennewick, WA) generate the potentials used to control all elements of the system between the inlet capillary and the circular ion funnel, which is the last element before the stacked-ring ion guide of the original mass spectrometer. One MIPS with 16 DC outputs supplies voltages for the ion funnels and inlet capillary and synchronizes the time-dependent voltage changes between the MIPS systems and an 8-bit, 1 GHz analog-to-digital converter, as described elsewhere.[57] Two MIPS with four arbitrary waveform generators (ARB) each supply the traveling waves to the SLIM boards. The ARB modules enable independent control of the TW amplitude, TW frequency, and direction (forward or reverse) of each TW region on the SLIM boards. The RF potentials applied to the ion funnel trap have a peak-to-peak amplitude (V_{p-p}) of 120 V and a frequency of 804 kHz, and the RF potentials applied to the rectangular ion funnel, SLIM boards, and circular ion funnel have a V_{p-p} of 240 V and a frequency of 943 kHz.

2.4 Results & Discussion

2.4.1 Instrument Operation

The SLIM boards consist of eight separate TW regions (numbered in Figure 2.1A). By controlling the traveling waves applied to these regions independently, ion accumulation, trapping, selection, and separation are enabled. Ion packets are generated prior to IM separation at region 3 in a four-step process (Figure 2.1B). In the first step (divert), the traveling wave on ^{1}R transports ions entering from the rectangular ion funnel toward ^{2}R, and the traveling wave on ^{2}R transports ions out of the SLIM region toward a collection electrode. In the next step (accumulate), the traveling wave on ^{2}R is reversed, transporting ions to ^{3}R, while the traveling wave on ^{3}R is stopped (wave potentials are applied to the electrodes but those waves are stationary). This establishes a static trap at the interface between ^{2}R and ^{3}R where ions can accumulate. After accumulation, the traveling waves on ^{2}R return to the divert configuration while the ion packet remains trapped at the beginning of ^{3}R. Finally, the traveling wave on ^{3}R starts moving toward ^{4}R (inject), initiating an IM separation.

A simple IM separation is performed by operating the traveling wave on all downstream regions in the forward direction relative to the axis of transmission following ion packet generation. More complex experiments, including tandem IM and multipass separations, require time-dependent modulation of the traveling waves on other TW regions. Selection of an ion population after ^{1}D is performed by changing the direction of the traveling wave on ^{4}R to transmit ions of a desired mobility while directing all others to a collection electrode (Figure 2.1C). This process is analogous to the packet generation described above, in which a divert step directs undesired high mobility ions to a collection electrode, an accumulate step directs ions of the desired mobility toward ^{5}R where they are trapped in a static trap, undesired low mobility

ions are again diverted to waste, and finally the trapped ions are released onto ^{2}D for separation. Multi-pass experiments are performed by modulating the direction of the traveling wave on ^{7}R such that ions remain on the boards and continue to undergo IM separation for a desired number of cycles before being transmitted toward the circular ion funnel and ultimately the mass spectrometer.

2.4.2 Single-Pass IM-MS

In a simple IM experiment, a packet of ions is generated as depicted in Figure 2.1B. Following the accumulate step, the ion packet is held for 4 ms (second divert step) before being released onto ^{1}D. The traveling waves on all subsequent regions direct ions toward the mass spectrometer, separating them along a 171-cm electrode path (Figure 2.2A). Ions generated from a mixture of ubiquitin (8.6 kDa), bovine serum albumin (66 kDa), and *beta*-lactoglobulin (18 kDa) were separated in such an experiment. The *m*/*z* of the protein mixture ions are plotted against their arrival times in Figure 2.2B. This demonstrates the platform's ability to separate protein ions ranging from 1000 to 5000 *m*/*z* under one set of potentials and TW conditions. We have previously reported the single-dimension IM separation of a mixture of protein ions on an electrostatic SLIM system with a drift length of 83 cm.[53] Compared to that instrument, for a similar protein mixture, the overall arrival times for ions analyzed on the TW instrument are longer, ranging from 170 to 330 ms. Arrival-time peaks are also broader, as ions with longer arrival times experience more diffusion during an IM separation.

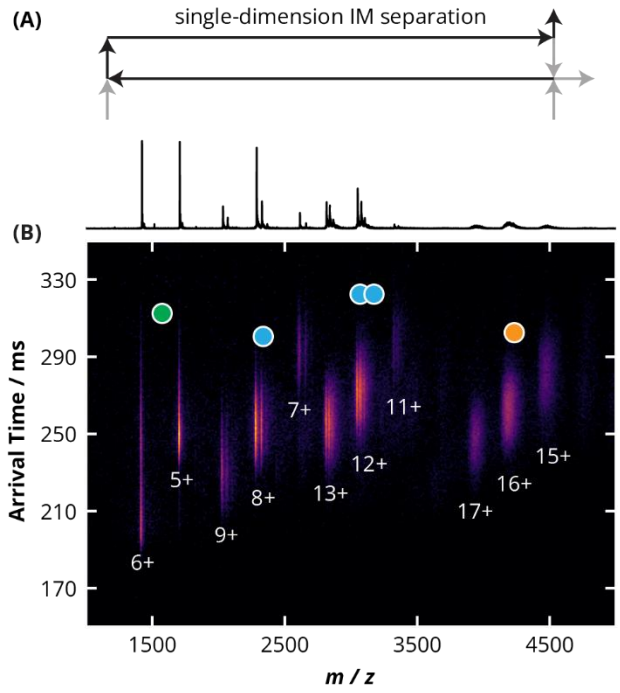

Figure 2.2. (A) Cartoon representation of the direction of each traveling wave during a simple IM separation following ion accumulation. Traveling waves with a frequency of 40 kHz and height of 25 $V_{p\text{-}p}$ and a guard bias of 8 V were used for the separation. (B) IM-MS data from a separation of native-like ions of ubiquitin (green marker), *beta*-lactoglobulin monomer and dimer (blue markers), and bovine serum albumin (orange marker). The mass spectrum is projected above the 2-dimensional heat map. The charge states of the detected ions are indicated below each feature in the heat map.

These IM-MS experiments used a guard bias of 8 V. We observed that the magnitude of the applied guard voltage impacted ion arrival times: increased guard potentials resulted in shorter arrival times for ions of a given mobility. We also observed that increasing the guard voltage resulted in increased relative abundances for lower-mobility conformers of protein ions, which we attribute to initial native-like structures that have unfolded in the gas phase. This

observation is consistent with our understanding of the effect of guard potential on ion position – namely, that increased field penetration pushes ions closer to the electrode surfaces.[58] Clowers and coworkers have also suggested that SLIM guard bias may be used to drive interconversion between structural states of peptide ions.[60] These observations will be discussed in further detail below.

2.4.3 Multiple-Pass IM-MS

After passing through ^{6}R and depending on the direction of the traveling-wave in ^{7}R, ions can either be directed out of the SLIM region and towards the TOF mass analyzer or be directed back toward ^{3}R for additional separation. Similar "multi-pass" separations, in which ions traverse one or more portions of an IM system multiple times within the same separation in order to achieve longer path lengths, have been performed previously on other instruments.[20,23,61] By reversing the direction of the traveling wave applied to ^{7}R, ions exiting ^{6}R can be directed onto ^{8}R, initiating a subsequent pass around the SLIM region. Ions will continue to separate around this path, shown in Figure 2.3A, until the traveling wave on ^{7}R is directed back toward the circular ion funnel. Any ions exiting ^{6}R after this time are directed toward the circular ion funnel and ultimately detected. By varying the time at which the traveling wave on ^{7}R changes direction, the number of passes traversed by the ions can be controlled. Each additional pass increases the total separation length by 172 cm. Figure 2.3B compares the arrival-time distributions of selected ions sprayed from a commercial tuning mixture subjected to up to 6 passes around the SLIM region.

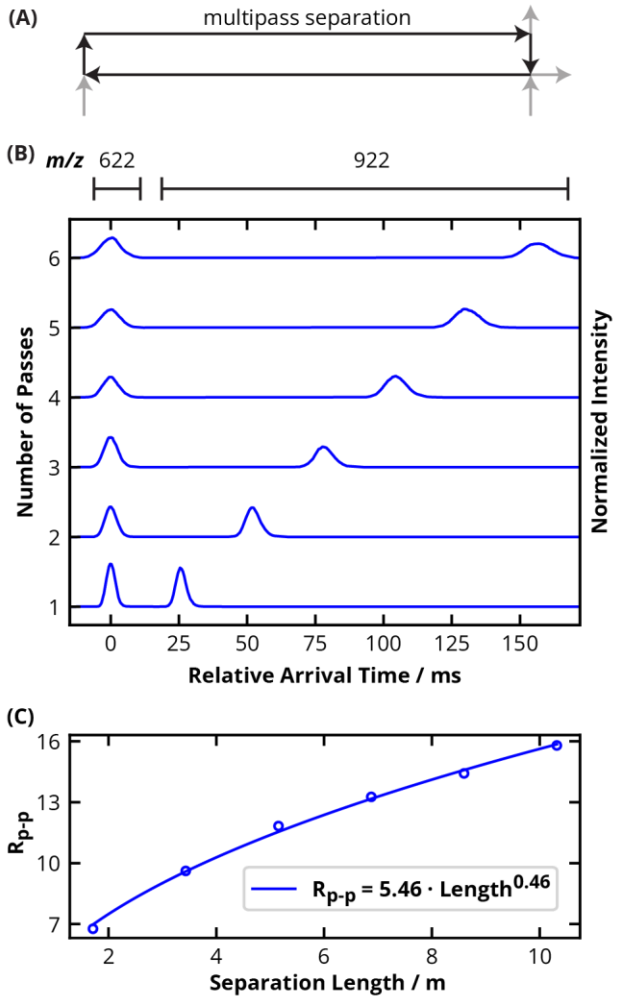

Figure 2.3. (A) Cartoon representation of the direction of each traveling wave during a multipass IM separation following ion accumulation and before ion detection. Traveling waves with a frequency of 15 kHz and height of 25 V_{p-p} were used for the separations. (B) Relative arrival-time distributions for the *m*/z 622 and 922 ions generated from a commercial tuning mixture after a varying number of passes around the SLIM boards. For ease of comparison, arrival-time distributions were shifted such that the centroids of the *m*/*z* 622 peaks were aligned for each separation length probed. (C) Calculated peak-to-peak resolutions for the *m*/*z* 622 and 922 ions as a function of total separation length. Values calculated from

experimental ATDs (represented by circles) were fitted with a power function (represented by a solid line).

One metric for assessing the quality of an IM separation is peak-to-peak resolution, $R_{p\text{-}p}$:

$$R_{p-p} = 2\left|\frac{t_2 - t_1}{\Delta t_2 + \Delta t_1}\right| \quad (2.1)$$

where t_2 and t_1 are the centroid values of the two arrival-time distributions and Δt_2 and Δt_1 are the full widths at half the maximum (FWHM) values of the two arrival-time distributions.[19,58] Peak-to-peak resolution offers the advantage over resolving power of a single peak that it is sensitive to ion "surfing" behavior, in which peaks appear artificially narrow due to limited rollover events and minimal separation occurring.[58] It is evident from the aligned arrival-time distributions (Figure 2.3B) that as total separation length increases, the temporal separation between the two peaks increases as well as the widths of both peaks. To quantify this relationship, Figure 2.3C displays the peak-to-peak resolution values calculated for the *m*/*z* 622 and 922 tuning mix ions from separations up to 6 passes in length. The calculated $R_{p\text{-}p}$ values were fitted with a power function of the form $R_{p\text{-}p} = a \cdot \text{Length}^b$; the value of $b \sim 0.46$ is similar to the expectation that ion mobility resolution should scale with the square root of separation length.[19]

2.4.4 Time-Dependent, Selection-Trapping IM-IM-MS

While tandem IM separations have seen wider use to provide additional structural information, a few studies have also trapped mobility-selected ions between IM dimensions.[34,45] Benefits of the "selection-trapping" approach include that the selected ion population can be spatially focused, limiting peak broadening caused by ion diffusion during the first dimension of IM.[62] On SLIMPHONY, selection-trapping tandem IM experiments are performed by accumulating an ion packet as described previously (Figure 2.1B) and performing the first

dimension of IM (^{1}D) along ^{3}R. Ions comprising a desired population (e.g., charge state or conformational state) are selected between ^{1}D and ^{2}D (Figure 2.1C). The time window for the selection is determined empirically for each analyte. Following ion selection, the wave applied to ^{5}R can remain stationary for an arbitrary period, referred to as "delay time," resulting in trapping of selected ions prior to an 87-cm ^{2}D separation. Figure 2.4B shows results of tandem IM separations of 6+ ubiquitin trapped for delay times ranging from 5 to 525 ms.

Tandem IM separations of 6+ ubiquitin, shown in Figure 2.4B, are consistent with results from similar experiments performed on an electrostatic SLIM instrument.[46] At short delay times, ion intensity is primarily centered around an arrival time of just over 100 ms, with a small shoulder of intensity at around 122 ms. As delay time increases, the population of ions arriving at the earlier rival time decreases while the population of ions arriving at the later arrival time increases and simultaneously shifts to longer drift times, centered around 130 ms. At the longest delay time of 525 ms, the total ion intensity is partitioned roughly evenly between the two populations. As observed in the electrostatic tandem IM separations of 6+ ubiquitin, there appears to be two distinct structures, a more compact one favored under shorter delay times and a more extended one favored under longer delay times, that are well-separated in ^{2}D.

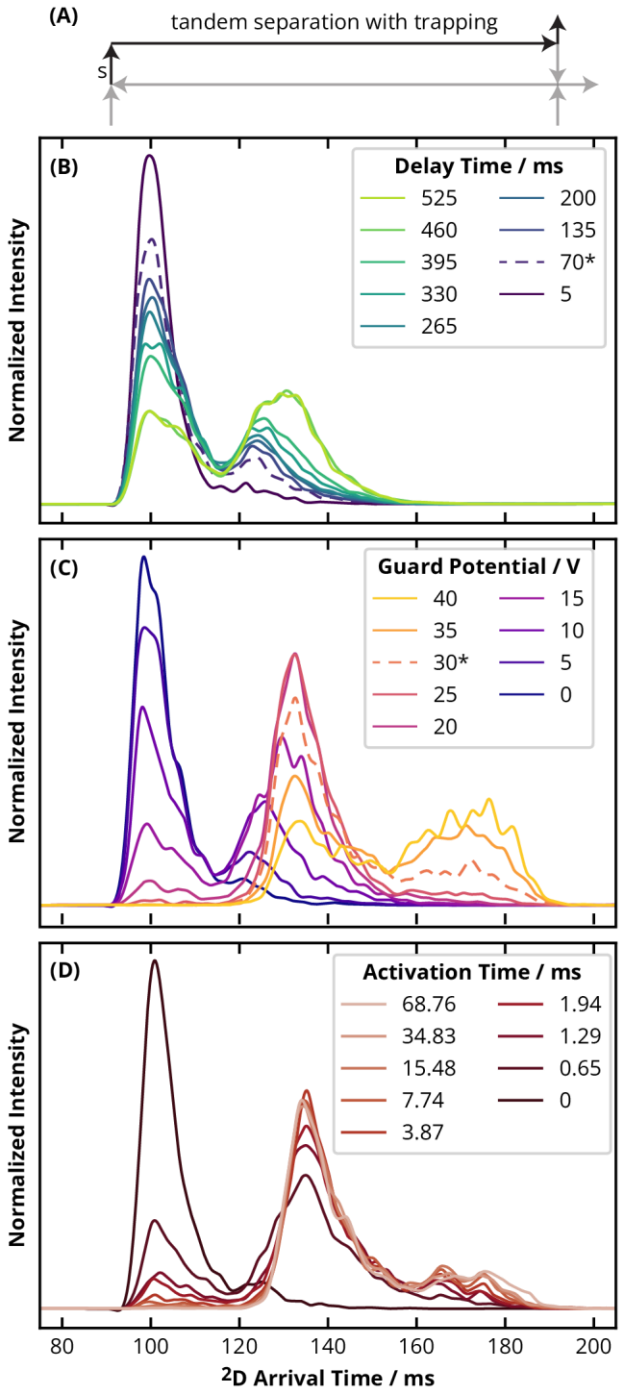

Figure 2.4. (A) Cartoon representation of the direction of each traveling wave during a tandem IM separation following ion accumulation, ^{1}D separation, and selection. The region where 6+ ubiquitin was selected is indicated by an *s*. (B) ^{2}D arrival-time distributions for 6+ ubiquitin ions trapped at ^{5}R for varying delay times

between IM dimensions. Distributions have been aligned such that the time point $t_A = 0$ corresponds with the time at which ions are released from trapping at ^{5}R. The 70 ms trace, indicated with an asterisk in the legend, is plotted with a dashed line for ease of comparison to the subsequent panels, which both employed ~70 ms trapping time for all experiments. (C) ^{2}D arrival-time distributions for 6+ ubiquitin ions trapped at ^{5}R with varying potential applied to the guard electrodes while trapped. The 30 V trace, indicated with an asterisk in the legend, is plotted with a dashed line for ease of comparison to the subsequent panel, which employed 30 V of guard activation for all experiments. (D) ^{2}D arrival-time distributions for 6+ ubiquitin ions trapped for ~70 ms at ^{5}R with 30 V applied to the guard electrodes for activation time varying from 0 to ~69 ms. The potential applied to the guard electrodes was lowered from 30 V to 0 V after the activation duration for the remainder of the total trapping time. Instrumental parameters and timings for the separation and trapping portions of the experiments shown in B–D are displayed in Table A.1.1, Table A.1.2, and Figure A.1.1.

2.4.5 Activating Ions Between Dimensions of Selection-Trapping IM-IM-MS

The tandem IM experiments discussed thus far have assessed the effect of varying delay times on ion arrival-time distributions. In our analysis of a variety of single-pass IM-MS, multi-pass IM-MS (vide infra), and time-dependent, selection trapping IM-MS experiments using the same guard bias, we observed that the rate of unfolding during trapping appeared to be greater than that during transport. Combined with our observations of increased unfolding observed for

experiments with higher potentials applied to the guard electrodes, we probed the effect of modulating the guard bias between dimensions of selection-trapping, IM-IM-MS experiments.

Figure 2.4C shows results from tandem IM separations of 6+ ubiquitin with constant ~70 ms trapping times while varying the potential applied to the guard electrodes during trapping at ^{5}R. These experiments were performed as described previously, by generating an ion packet, separating it along ^{1}D, selecting the desired charge state, and trapping at ^{5}R prior to ^{2}D. During trapping at ^{5}R, a potential between 0 and 40 V was applied to the guard electrodes until ~1 ms before release of the trapped ions, when the potential was reset to 5 V. During all other steps of the experiment, the guard electrodes were held at 5 V.

For the separations with the lowest trap guard potentials, the 6+ ubiquitin arrival-time distribution is similar to those with the shortest delay times (Figure 2.4B), with the primary feature of the ATD centered around 100 ms and a smaller feature at around 122 ms. As the trap guard potential is increased up to 20 V, the population arriving around 100 ms is depleted in favor of the population arriving around 122 ms. At a trap guard potential of 15 V, the 6+ ubiquitin is roughly evenly partitioned between the populations with 100 ms and 122 ms arrival times. As the trap guard potential is increased beyond 20 V, the population centered at 122 ms shifts to around 130 ms and continues to increase in relative intensity. Finally, beyond guard potentials of 30 V, a third state centered around an arrival time of 175 ms begins to populate, as the two shorter arrival time states are both depleted.

The previously described experiments activated 6+ ubiquitin ions by varying the magnitude of the potential applied to the guard electrodes over ~69 ms of trapping. Figure 2.4D shows the arrival-time distributions of 6+ ubiquitin following 1) separation along ^{1}D, 2) selection, and 3) trapping for ~70 ms at ^{5}R with 30 V applied to the guard electrodes for 0 to ~69

ms. Following the activation duration for each experiment, the potential applied to the guard electrodes was lowered from 30 V to 0 V, until ~1 ms before release of the trapped ions, when the guard electrode potential was returned to 5 V. The arrival-time distributions exhibit similar trends as those shown in Figure 2.4C, in which the population with the shortest arrival time is depleted in favor of two extended populations with longer arrival times. After only ~650 μs of guard-potential activation, the majority of the population of 6+ ubiquitin with the shortest arrival time is depleted, and after ~69 ms of guard-potential activation, the arrival-time distribution of 6+ ubiquitin qualitatively resembles that of the 30 V guard electrode potential trace in Figure 2.4C (indicated with a dashed line for ease of visualization).

Overall, the results from these experiments indicate that by alternately varying the delay time and the guard potential applied to trapped 6+ ubiquitin ions, different activation pathways can be achieved. Under the least activating conditions in both experiment types, the population arriving at 100 ms is dominant. As conditions become more activating in nature, that population is depleted in favor of one arriving at 122 ms, which concomitantly shifts to slightly longer arrival times. Activation via the potential applied to the guard electrodes eventually allows 6+ ubiquitin ions to access a third structural state comparable to that previously observed in energy-dependent experiments (i.e. collision-induced unfolding).[46,63] Using guard potentials during trapping to activate 6+ ubiquitin ions facilitates the generation of more extended conformations without the longer experiments needed to activate ions via increasing delay time.

2.4.6 Combining Multiple Passes and Activation in Selection-Trapping IM-IM-MS

SLIMPHONY is also capable of experiments that combine tandem and multiple-pass separations. Following ^{1}D, a subpopulation of interest is isolated as described previously. That subpopulation can then be subjected to additional IM separation. By modulating the direction of

the traveling wave applied to ^{7}R, the length of this additional separation can be controlled. Figure 2.5 shows results from separations of 6+ ubiquitin isolated and trapped for ~50 ms after ^{1}D (Figure 2.5B–D) or after traversing one full pass around the SLIM region (Figure 2.5E–G) and subjected to up to 2 additional passes before detection. This experiment combing tandem IM with multiple passes was performed with guard potentials ranging from 5 to 30 V applied during trapping of 6+ ubiquitin prior to any subsequent separation. More details about the timing of these experiments can be found in the Additional Methods in Appendix A.1.

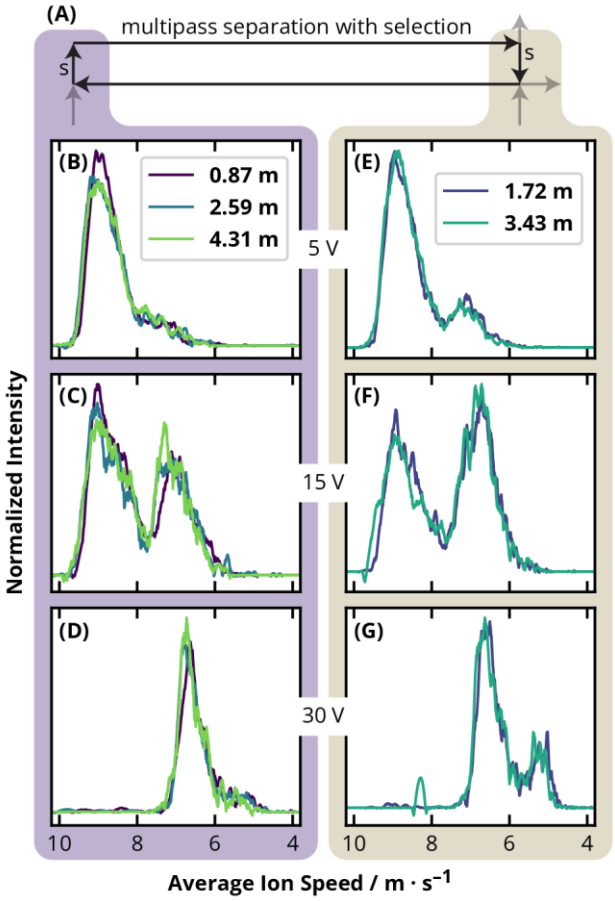

Figure 2.5. (A) Cartoon representation of the direction of each traveling wave during a tandem IM separation with multiple passes following a first dimension of IM separation, selection, and trapping and before ion detection. The locations

where 6+ ubiquitin was selected are indicated by an *s*. Traveling waves with a frequency of 15 kHz and height of 15 V_{p-p} were used for separation. (B–D) Average speed of 6+ ubiquitin ions selected after ^{1}D and subjected to up to 2 additional passes around the SLIM region, with varying potential applied to the guard electrodes during trapping immediately after selection. (E–G) Average speed of 6+ ubiquitin ions selected after one pass around the SLIM device and subjected to up to 2 additional passes around the SLIM region, with varying potential applied to the guard electrodes during trapping immediately after selection, as indicated by the labels between the columns. The x axes are oriented from high speed to low speed to aid in comparison to a traditional arrival-time distribution in which higher-mobility ions are shown to the left of lower-mobility ions.

To aid in comparing the results of separations of very different lengths, the average ion speed distributions were plotted (Figure 2.5B–D, E–G) by dividing the separation length in mm by the arrival-time axis for each separation. Ions with similar collision cross section values should traverse the SLIM device with similar average speeds regardless of separation length. Like the results shown in Figure 2.3C, results from these experiments indicate that by varying the potential applied to the guard electrodes during trapping between ^{1}D and ^{2}D, the distribution of structural populations of 6+ ubiquitin can be controlled. With 5 V applied to the guard electrodes during trapping and regardless of where ion selection was performed, the dominant feature of the average speed distribution is centered around ~9 m/s with a smaller feature centered around ~7 m/s. With a guard potential of 15 V, the 6+ ubiquitin intensity is partitioned relatively equally between populations moving at ~9 m/s and ~7 m/s. With 30 V applied to the

guard electrodes and for both selection regions, the majority of the 6+ ubiquitin has a speed of ~7 m/s, with a minor feature slightly above 5 m/s. Note that in Figure 2.5G, a small population of ions with a speed slightly above 8 m/s is observed. This is an artifact of the multi-pass timing. As ions complete the first pass after activation, they are sent for another pass if the traveling wave on ^{7}R moves toward ^{8}R. The direction of this traveling wave is reversed in preparation for detecting ions after they have completed the second pass. If ions completing their first pass have not fully exited ^{7}R when the wave direction is reversed, they are detected immediately and appear to have moved aberrantly fast relative to other ion populations due to their much shorter path length.

The trends in average speed distributions hold for separations of 87 cm, 259 cm, and 431 cm, corresponding to 0, 1, and 2 additional passes around the SLIM region after release from trapping at ^{5}R and before the final ^{2}D directing ions toward the detector. The trends are also maintained for separations of 172 cm and 343 cm, corresponding to 1 and 2 additional passes around the SLIM region after release from trapping at ^{8}R. The observed ion speed distributions vary as a function of applied guard potential during trapping and are independent of total separation length. Subjecting the range of 6+ ubiquitin structures to multiple passes does not appear to perturb their existing structural distributions, indicating that the observed structural changes occur as a direct consequence of the trapping conditions, with no evidence for isomerization during transport.

2.5 Conclusions

The new TW-SLIM instrument was used to perform several different types of IM separations by leveraging independent control of eight separate TW electrode regions. Small molecule, protein, and protein complex ions were accumulated, mobility-selected, trapped,

activated, and separated over a range of path lengths. Multiple-pass experiments were demonstrated to improve peak-to-peak resolution (Figure 2.3C). Selection-trapping tandem IM separations of 6+ ubiquitin revealed unfolding to different extents as a result of time-based (Figure 2.4B) versus voltage-based (Figure 2.4C–D) activation. Selection-trapping tandem IM was then performed while simultaneously subjecting 6+ ubiquitin ions to multi-pass separations (Figure 2.5B–D, E–G), illustrating the flexibility of the platform and our ability to manipulate ions via different strategies and at multiple sites within the instrument.

The results in Figure 2.4 indicate that (1) ions are activated when high guard bias voltages are applied, (2) the magnitude of that activation increases with the magnitude of the guard bias, and (3) the activation occurs continuously throughout the duration of time that the high guard bias is applied. Collisional activation has been integrated with a wide range of IM experiments, including foundational studies of gas-phase protein ions[64–66] and more-recent applications of collision-induced unfolding.[67–71] Activation during earlier beam-type experiments typically involved acceleration of ions during spatial transfer between regions of the instrument, in which potential energy would have rapidly been converted to internal energy. For example, recent modeling of kinetic energy transfer under the conditions of collision cells and mobility cells in conventional IM-MS instruments suggests that collisional heating and cooling in those experiments is very rapid and certainly sub-millisecond; for 7+ cytochrome *c* injected into a drift cell "the ion spends only 1–2 μs within 10% of its maximum vibrational energy [and] cools back [to ambient] in less than 30 μs."[72] As shown in Figure 2.4, the ability to precisely and independently control the duration and extent of activation enable the observation of different conformational distributions. These new experiments, which we refer to as "Conformational

Landscapes Observed Through Controlled Kinetics" (CLOCK) are under continued study and will be reported in more detail in the near future.

2.6 Acknowledgments

This material is based upon work supported by the National Institute of General Medical Sciences of the National Institutes of Health through award R01GM130708 (M.F.B.), the National Science Foundation through award 2203513 (M.F.B.) from the Division of Chemistry, with partial co-funding from the Division of Molecular and Cellular Biosciences, and the National Science Foundation through award 2140004 (A.E.R.) from the Division of Graduate Education.

2.7 References

(1) Griffin, M. D. W.; Gerrard, J. A. The Relationship between Oligomeric State and Protein Function. In *Protein Dimerization and Oligomerization in Biology*; Matthews, J. M., Ed.; Advances in Experimental Medicine and Biology; Springer New York: New York, NY, 2012; Vol. 747, pp 74–90. https://doi.org/10.1007/978-1-4614-3229-6_5.

(2) Barth, M.; Schmidt, C. Native Mass Spectrometry—A Valuable Tool in Structural Biology. *J. Mass Spectrom.* **2020**, *55* (10), e4578. https://doi.org/10.1002/jms.4578.

(3) Creese, A. J.; Cooper, H. J. Separation and Identification of Isomeric Glycopeptides by High Field Asymmetric Waveform Ion Mobility Spectrometry. *Anal. Chem.* **2012**, *84* (5), 2597–2601. https://doi.org/10.1021/ac203321y.

(4) Bagal, D.; Valliere-Douglass, J. F.; Balland, A.; Schnier, P. D. Resolving Disulfide Structural Isoforms of IgG2 Monoclonal Antibodies by Ion Mobility Mass Spectrometry. *Anal. Chem.* **2010**, *82* (16), 6751–6755. https://doi.org/10.1021/ac1013139.

(5) May, J. C.; McLean, J. A. A Uniform Field Ion Mobility Study of Melittin and Implications of Low-field Mobility for Resolving Fine Cross-sectional Detail in Peptide and Protein Experiments. *PROTEOMICS* **2015**, *15* (16), 2862–2871. https://doi.org/10.1002/pmic.201400551.

(6) Stauber, J.; MacAleese, L.; Franck, J.; Claude, E.; Snel, M.; Kaletas, B. K.; Wiel, I. M. V. D.; Wisztorski, M.; Fournier, I.; Heeren, R. M. A. On-Tissue Protein Identification and Imaging by MALDI-Ion Mobility Mass Spectrometry. *J. Am. Soc. Mass Spectrom.* **2010**, *21* (3), 338–347. https://doi.org/10.1016/j.jasms.2009.09.016.

(7) Robb, C. G.; Dao, T. P.; Ujma, J.; Castañeda, C. A.; Beveridge, R. Ion Mobility Mass Spectrometry Unveils Global Protein Conformations in Response to Conditions That Promote and Reverse Liquid–Liquid Phase Separation. *J. Am. Chem. Soc.* **2023**, *145* (23), 12541–12549. https://doi.org/10.1021/jacs.3c00756.

(8) Pacholarz, K. J.; Peters, S. J.; Garlish, R. A.; Henry, A. J.; Taylor, R. J.; Humphreys, D. P.; Barran, P. E. Molecular Insights into the Thermal Stability of mAbs with Variable-Temperature Ion-Mobility Mass Spectrometry. *ChemBioChem* **2016**, *17* (1), 46–51. https://doi.org/10.1002/cbic.201500574.

(9) Jeanne Dit Fouque, K.; Fernandez-Lima, F. Following Structural Changes by Thermal Denaturation Using Trapped Ion Mobility Spectrometry–Mass Spectrometry. *J. Phys. Chem. B* **2020**, *124* (29), 6257–6265. https://doi.org/10.1021/acs.jpcb.0c04276.

(10) El-Baba, T. J.; Woodall, D. W.; Raab, S. A.; Fuller, D. R.; Laganowsky, A.; Russell, D. H.; Clemmer, D. E. Melting Proteins: Evidence for Multiple Stable Structures upon Thermal Denaturation of Native Ubiquitin from Ion Mobility Spectrometry-Mass

Spectrometry Measurements. *J. Am. Chem. Soc.* **2017**, *139* (18), 6306–6309. https://doi.org/10.1021/jacs.7b02774.

(11) McCabe, J. W.; Shirzadeh, M.; Walker, T. E.; Lin, C.-W.; Jones, B. J.; Wysocki, V. H.; Barondeau, D. P.; Clemmer, D. E.; Laganowsky, A.; Russell, D. H. Variable-Temperature Electrospray Ionization for Temperature-Dependent Folding/Refolding Reactions of Proteins and Ligand Binding. *Anal. Chem.* **2021**, *93* (18), 6924–6931. https://doi.org/10.1021/acs.analchem.1c00870.

(12) Köhler, M.; Marchand, A.; Hentzen, N. B.; Egli, J.; Begley, A. I.; Wennemers, H.; Zenobi, R. Temperature-Controlled Electrospray Ionization Mass Spectrometry as a Tool to Study Collagen Homo- and Heterotrimers. *Chem. Sci.* **2019**, *10* (42), 9829–9835. https://doi.org/10.1039/C9SC03248G.

(13) Hyung, S.-J.; Robinson, C. V.; Ruotolo, B. T. Gas-Phase Unfolding and Disassembly Reveals Stability Differences in Ligand-Bound Multiprotein Complexes. *Chem. Biol.* **2009**, *16* (4), 382–390. https://doi.org/10.1016/j.chembiol.2009.02.008.

(14) Lai, A. L.; Clerico, E. M.; Blackburn, M. E.; Patel, N. A.; Robinson, C. V.; Borbat, P. P.; Freed, J. H.; Gierasch, L. M. Key Features of an Hsp70 Chaperone Allosteric Landscape Revealed by Ion-Mobility Native Mass Spectrometry and Double Electron-Electron Resonance. *J. Biol. Chem.* **2017**, *292* (21), 8773–8785. https://doi.org/10.1074/jbc.M116.770404.

(15) Liu, Y.; Cong, X.; Liu, W.; Laganowsky, A. Characterization of Membrane Protein–Lipid Interactions by Mass Spectrometry Ion Mobility Mass Spectrometry. *J. Am. Soc. Mass Spectrom.* **2017**, *28* (4), 579–586. https://doi.org/10.1007/s13361-016-1555-1.

(16) Song, Y.; Nelp, M. T.; Bandarian, V.; Wysocki, V. H. Refining the Structural Model of a Heterohexameric Protein Complex: Surface Induced Dissociation and Ion Mobility Provide Key Connectivity and Topology Information. *ACS Cent. Sci.* **2015**, *1* (9), 477–487. https://doi.org/10.1021/acscentsci.5b00251.

(17) Pont, L.; Benavente, F.; Vilaseca, M.; Giménez, E.; Sanz-Nebot, V. Characterisation of Serum Transthyretin by Electrospray Ionisation-Ion Mobility Mass Spectrometry: Application to Familial Amyloidotic Polyneuropathy Type I (FAP-I). *Talanta* **2015**, *144*, 1216–1224. https://doi.org/10.1016/j.talanta.2015.07.079.

(18) Smith, D. P.; Radford, S. E.; Ashcroft, A. E. Elongated Oligomers in β_2 -Microglobulin Amyloid Assembly Revealed by Ion Mobility Spectrometry-Mass Spectrometry. *Proc. Natl. Acad. Sci.* **2010**, *107* (15), 6794–6798. https://doi.org/10.1073/pnas.0913046107.

(19) Zercher, B. P.; Gozzo, T. A.; Wageman, A.; Bush, M. F. Enhancing the Depth of Analyses with Next-Generation Ion Mobility Experiments. *Annu. Rev. Anal. Chem.* **2023**, *16* (1), 27–48. https://doi.org/10.1146/annurev-anchem-091522-031329.

(20) Giles, K.; Ujma, J.; Wildgoose, J.; Pringle, S.; Richardson, K.; Langridge, D.; Green, M. A Cyclic Ion Mobility-Mass Spectrometry System. *Anal. Chem.* **2019**, *91* (13), 8564–8573. https://doi.org/10.1021/acs.analchem.9b01838.

(21) Hernandez, D. R.; DeBord, J. D.; Ridgeway, M. E.; Kaplan, D. A.; Park, M. A.; Fernandez-Lima, F. Ion Dynamics in a Trapped Ion Mobility Spectrometer. *The Analyst* **2014**, *139* (8), 1913–1921. https://doi.org/10.1039/C3AN02174B.

(22) Deng, L.; Ibrahim, Y. M.; Hamid, A. M.; Garimella, S. V. B.; Webb, I. K.; Zheng, X.; Prost, S. A.; Sandoval, J. A.; Norheim, R. V.; Anderson, G. A.; Tolmachev, A. V.; Baker, E. S.; Smith, R. D. Ultra-High Resolution Ion Mobility Separations Utilizing Traveling

Waves in a 13 m Serpentine Path Length Structures for Lossless Ion Manipulations Module. *Anal. Chem.* **2016**, *88* (18), 8957–8964. https://doi.org/10.1021/acs.analchem.6b01915.

(23) Deng, L.; Webb, I. K.; Garimella, S. V. B.; Hamid, A. M.; Zheng, X.; Norheim, R. V.; Prost, S. A.; Anderson, G. A.; Sandoval, J. A.; Baker, E. S.; Ibrahim, Y. M.; Smith, R. D. Serpentine Ultralong Path with Extended Routing (SUPER) High Resolution Traveling Wave Ion Mobility-MS Using Structures for Lossless Ion Manipulations. *Anal. Chem.* **2017**, *89* (8), 4628–4634. https://doi.org/10.1021/acs.analchem.7b00185.

(24) Giles, K.; Pringle, S. D.; Worthington, K. R.; Little, D.; Wildgoose, J. L.; Bateman, R. H. Applications of a Travelling Wave-based Radio-frequency-only Stacked Ring Ion Guide. *Rapid Commun. Mass Spectrom.* **2004**, *18* (20), 2401–2414. https://doi.org/10.1002/rcm.1641.

(25) Deslignière, E.; Botzanowski, T.; Diemer, H.; Cooper-Shepherd, D. A.; Wagner-Rousset, E.; Colas, O.; Béchade, G.; Giles, K.; Hernandez-Alba, O.; Beck, A.; Cianférani, S. High-Resolution IMS–MS to Assign Additional Disulfide Bridge Pairing in Complementarity-Determining Regions of an IgG4 Monoclonal Antibody. *J. Am. Soc. Mass Spectrom.* **2021**, *32* (10), 2505–2512. https://doi.org/10.1021/jasms.1c00151.

(26) Deslignière, E.; Ollivier, S.; Ehkirch, A.; Martelet, A.; Ropartz, D.; Lechat, N.; Hernandez-Alba, O.; Menet, J.-M.; Clavier, S.; Rogniaux, H.; Genet, B.; Cianférani, S. Combination of IM-Based Approaches to Unravel the Coexistence of Two Conformers on a Therapeutic Multispecific mAb. *Anal. Chem.* **2022**, *94* (22), 7981–7989. https://doi.org/10.1021/acs.analchem.2c00928.

(27) Ujma, J.; Ropartz, D.; Giles, K.; Richardson, K.; Langridge, D.; Wildgoose, J.; Green, M.; Pringle, S. Cyclic Ion Mobility Mass Spectrometry Distinguishes Anomers and Open-Ring Forms of Pentasaccharides. *J. Am. Soc. Mass Spectrom.* **2019**, *30* (6), 1028–1037. https://doi.org/10.1007/s13361-019-02168-9.

(28) Peterson, T. L.; Nagy, G. Rapid Cyclic Ion Mobility Separations of Monosaccharide Building Blocks as a First Step toward a High-Throughput Reaction Screening Platform for Carbohydrate Syntheses. *RSC Adv.* **2021**, *11* (63), 39742–39747. https://doi.org/10.1039/D1RA08746K.

(29) Wojcik, R.; Nagy, G.; Attah, Isaac. K.; Webb, I. K.; Garimella, S. V. B.; Weitz, K. K.; Hollerbach, A.; Monroe, M. E.; Ligare, M. R.; Nielson, F. F.; Norheim, R. V.; Renslow, R. S.; Metz, T. O.; Ibrahim, Y. M.; Smith, R. D. SLIM Ultrahigh Resolution Ion Mobility Spectrometry Separations of Isotopologues and Isotopomers Reveal Mobility Shifts Due to Mass Distribution Changes. *Anal. Chem.* **2019**, *91* (18), 11952–11962. https://doi.org/10.1021/acs.analchem.9b02808.

(30) Koeniger, S. L.; Merenbloom, S. I.; Clemmer, D. E. Evidence for Many Resolvable Structures within Conformation Types of Electrosprayed Ubiquitin Ions. *J. Phys. Chem. B* **2006**, *110* (13), 7017–7021. https://doi.org/10.1021/jp056165h.

(31) Koeniger, S. L.; Merenbloom, S. I.; Valentine, S. J.; Jarrold, M. F.; Udseth, H. R.; Smith, R. D.; Clemmer, D. E. An IMS−IMS Analogue of MS−MS. *Anal. Chem.* **2006**, *78* (12), 4161–4174. https://doi.org/10.1021/ac051060w.

(32) Merenbloom, S. I.; Koeniger, S. L.; Valentine, S. J.; Plasencia, M. D.; Clemmer, D. E. IMS−IMS and IMS−IMS−IMS/MS for Separating Peptide and Protein Fragment Ions. *Anal. Chem.* **2006**, *78* (8), 2802–2809. https://doi.org/10.1021/ac052208e.

(33) Li, H.; Bendiak, B.; Siems, W. F.; Gang, D. R.; Hill, H. H. Carbohydrate Structure Characterization by Tandem Ion Mobility Mass Spectrometry (IMMS)^2. *Anal. Chem.* **2013**, *85* (5), 2760–2769. https://doi.org/10.1021/ac303273z.

(34) Simon, A.-L.; Chirot, F.; Choi, C. M.; Clavier, C.; Barbaire, M.; Maurelli, J.; Dagany, X.; MacAleese, L.; Dugourd, P. Tandem Ion Mobility Spectrometry Coupled to Laser Excitation. *Rev. Sci. Instrum.* **2015**, *86* (9), 094101. https://doi.org/10.1063/1.4930604.

(35) Le Fèvre, A.; Dugourd, P.; Chirot, F. Exploring Conformational Landscapes Using Trap and Release Tandem Ion Mobility Spectrometry. *Anal. Chem.* **2021**, *93* (9), 4183–4190. https://doi.org/10.1021/acs.analchem.0c04520.

(36) Eldrid, C.; Ben-Younis, A.; Ujma, J.; Britt, H.; Cragnolini, T.; Kalfas, S.; Cooper-Shepherd, D.; Tomczyk, N.; Giles, K.; Morris, M.; Akter, R.; Raleigh, D.; Thalassinos, K. Cyclic Ion Mobility–Collision Activation Experiments Elucidate Protein Behavior in the Gas Phase. *J. Am. Soc. Mass Spectrom.* **2021**, *32* (6), 1545–1552. https://doi.org/10.1021/jasms.1c00018.

(37) Makey, D. M.; Gadkari, V. V.; Kennedy, R. T.; Ruotolo, B. T. Cyclic Ion Mobility-Mass Spectrometry and Tandem Collision Induced Unfolding for Quantification of Elusive Protein Biomarkers. *Anal. Chem.* **2024**, *96* (15), 6021–6029. https://doi.org/10.1021/acs.analchem.4c00477.

(38) Ollivier, S.; Tarquis, L.; Fanuel, M.; Li, A.; Durand, J.; Laville, E.; Potocki-Veronese, G.; Ropartz, D.; Rogniaux, H. Anomeric Retention of Carbohydrates in Multistage Cyclic Ion Mobility (IMS^n): De Novo Structural Elucidation of Enzymatically Produced Mannosides. *Anal. Chem.* **2021**, *93* (15), 6254–6261. https://doi.org/10.1021/acs.analchem.1c00673.

(39) Ollivier, S.; Fanuel, M.; Rogniaux, H.; Ropartz, D. Molecular Networking of High-Resolution Tandem Ion Mobility Spectra: A Structurally Relevant Way of Organizing Data in Glycomics? *Anal. Chem.* **2021**, *93* (31), 10871–10878. https://doi.org/10.1021/acs.analchem.1c01244.

(40) Peterson, T. L.; Nagy, G. Toward Sequencing the Human Milk Glycome: High-Resolution Cyclic Ion Mobility Separations of Core Human Milk Oligosaccharide Building Blocks. *Anal. Chem.* **2021**, *93* (27), 9397–9407. https://doi.org/10.1021/acs.analchem.1c00942.

(41) Liu, F. C.; Ridgeway, M. E.; Park, M. A.; Bleiholder, C. Tandem Trapped Ion Mobility Spectrometry. *The Analyst* **2018**, *143* (10), 2249–2258. https://doi.org/10.1039/C7AN02054F.

(42) Liu, F. C.; Cropley, T. C.; Ridgeway, M. E.; Park, M. A.; Bleiholder, C. Structural Analysis of the Glycoprotein Complex Avidin by Tandem-Trapped Ion Mobility Spectrometry–Mass Spectrometry (Tandem-TIMS/MS). *Anal. Chem.* **2020**, *92* (6), 4459–4467. https://doi.org/10.1021/acs.analchem.9b05481.

(43) Liu, F. C.; Kirk, S. R.; Caldwell, K. A.; Pedrete, T.; Meier, F.; Bleiholder, C. Tandem Trapped Ion Mobility Spectrometry/Mass Spectrometry (tTIMS/MS) Reveals Sequence-Specific Determinants of Top-Down Protein Fragment Ion Cross Sections. *Anal. Chem.* **2022**, *94* (23), 8146–8155. https://doi.org/10.1021/acs.analchem.1c05171.

(44) Liu, F. C.; Ridgeway, M. E.; Wootton, C. A.; Theisen, A.; Panczyk, E. M.; Meier, F.; Park, M. A.; Bleiholder, C. Top-Down Protein Analysis by Tandem-Trapped Ion Mobility Spectrometry/Mass Spectrometry (Tandem-TIMS/MS) Coupled with Ultraviolet Photodissociation (UVPD) and Parallel Accumulation/Serial Fragmentation (PASEF)

MS/MS Analysis. *J. Am. Soc. Mass Spectrom.* **2023**, *34* (10), 2232–2246. https://doi.org/10.1021/jasms.3c00187.

(45) Allen, S. J.; Eaton, R. M.; Bush, M. F. Structural Dynamics of Native-Like Ions in the Gas Phase: Results from Tandem Ion Mobility of Cytochrome *c*. *Anal. Chem.* **2017**, *89* (14), 7527–7534. https://doi.org/10.1021/acs.analchem.7b01234.

(46) Zercher, B. P.; Hong, S.; Roush, A. E.; Feng, Y.; Bush, M. F. Are the Gas-Phase Structures of Molecular Elephants Enduring or Ephemeral? Results from Time-Dependent, Tandem Ion Mobility. *Anal. Chem.* **2023**, *95* (25), 9589–9597. https://doi.org/10.1021/acs.analchem.3c01222.

(47) Dyukova, I.; Ben Faleh, A.; Warnke, S.; Yalovenko, N.; Yatsyna, V.; Bansal, P.; Rizzo, T. R. A New Approach for Identifying Positional Isomers of Glycans Cleaved from Monoclonal Antibodies. *The Analyst* **2021**, *146* (15), 4789–4795. https://doi.org/10.1039/D1AN00780G.

(48) Bansal, P.; Yatsyna, V.; AbiKhodr, A. H.; Warnke, S.; Ben Faleh, A.; Yalovenko, N.; Wysocki, V. H.; Rizzo, T. R. Using SLIM-Based IMS-IMS Together with Cryogenic Infrared Spectroscopy for Glycan Analysis. *Anal. Chem.* **2020**, *92* (13), 9079–9085. https://doi.org/10.1021/acs.analchem.0c01265.

(49) Bansal, P.; Ben Faleh, A.; Warnke, S.; Rizzo, T. R. Identification of *N* -Glycan Positional Isomers by Combining IMS and Vibrational Fingerprinting of Structurally Determinant CID Fragments. *The Analyst* **2022**, *147* (4), 704–711. https://doi.org/10.1039/D1AN01861B.

(50) Pellegrinelli, R. P.; Yue, L.; Carrascosa, E.; Ben Faleh, A.; Warnke, S.; Bansal, P.; Rizzo, T. R. A New Strategy Coupling Ion-Mobility-Selective CID and Cryogenic IR

Spectroscopy to Identify Glycan Anomers. *J. Am. Soc. Mass Spectrom.* **2022**, *33* (5), 859–864. https://doi.org/10.1021/jasms.2c00043.

(51) Ben Faleh, A.; Warnke, S.; Bansal, P.; Pellegrinelli, R. P.; Dyukova, I.; Rizzo, T. R. Identification of Mobility-Resolved *N* -Glycan Isomers. *Anal. Chem.* **2022**, *94* (28), 10101–10108. https://doi.org/10.1021/acs.analchem.2c01181.

(52) Davidson, K. L.; Oberreit, D. R.; Hogan, C. J.; Bush, M. F. Nonspecific Aggregation in Native Electrokinetic Nanoelectrospray Ionization. *Int. J. Mass Spectrom.* **2017**, *420*, 35–42. https://doi.org/10.1016/j.ijms.2016.09.013.

(53) Eaton, R. M.; Zercher, B. P.; Wageman, A.; Bush, M. F. A Flexible, Modular Platform for Multidimensional Ion Mobility of Native-like Ions. *J. Am. Soc. Mass Spectrom.* **2023**, *34* (6), 1175–1185. https://doi.org/10.1021/jasms.3c00112.

(54) Clowers, B. H.; Ibrahim, Y. M.; Prior, D. C.; Danielson, W. F.; Belov, M. E.; Smith, R. D. Enhanced Ion Utilization Efficiency Using an Electrodynamic Ion Funnel Trap as an Injection Mechanism for Ion Mobility Spectrometry. *Anal. Chem.* **2008**, *80* (3), 612–623. https://doi.org/10.1021/ac701648p.

(55) Chen, T.-C.; Webb, I. K.; Prost, S. A.; Harrer, M. B.; Norheim, R. V.; Tang, K.; Ibrahim, Y. M.; Smith, R. D. Rectangular Ion Funnel: A New Ion Funnel Interface for Structures for Lossless Ion Manipulations. *Anal. Chem.* **2015**, *87* (1), 716–722. https://doi.org/10.1021/ac503564c.

(56) Shaffer, S. A.; Tolmachev, A.; Prior, D. C.; Anderson, G. A.; Udseth, H. R.; Smith, R. D. Characterization of an Improved Electrodynamic Ion Funnel Interface for Electrospray Ionization Mass Spectrometry. *Anal. Chem.* **1999**, *71* (15), 2957–2964. https://doi.org/10.1021/ac990346w.

(57) Allen, S. J.; Eaton, R. M.; Bush, M. F. Analysis of Native-Like Ions Using Structures for Lossless Ion Manipulations. *Anal. Chem.* **2016**, *88* (18), 9118–9126. https://doi.org/10.1021/acs.analchem.6b02089.

(58) Hamid, A. M.; Ibrahim, Y. M.; Garimella, S. V. B.; Webb, I. K.; Deng, L.; Chen, T.-C.; Anderson, G. A.; Prost, S. A.; Norheim, R. V.; Tolmachev, A. V.; Smith, R. D. Characterization of Traveling Wave Ion Mobility Separations in Structures for Lossless Ion Manipulations. *Anal. Chem.* **2015**, *87* (22), 11301–11308. https://doi.org/10.1021/acs.analchem.5b02481.

(59) Ben Faleh, A.; Warnke, S.; Rizzo, T. R. Combining Ultrahigh-Resolution Ion-Mobility Spectrometry with Cryogenic Infrared Spectroscopy for the Analysis of Glycan Mixtures. *Anal. Chem.* **2019**, *91* (7), 4876–4882. https://doi.org/10.1021/acs.analchem.9b00659.

(60) Kinlein, Z.; Clowers, B. H. Altering Conformational States of Dynamic Ion Populations Using Traveling Wave Structures for Lossless Ion Manipulations. *Anal. Chem.* **2024**, *96* (16), 6450–6458. https://doi.org/10.1021/acs.analchem.4c00692.

(61) Merenbloom, S. I.; Glaskin, R. S.; Henson, Z. B.; Clemmer, D. E. High-Resolution Ion Cyclotron Mobility Spectrometry. *Anal. Chem.* **2009**, *81* (4), 1482–1487. https://doi.org/10.1021/ac801880a.

(62) Eaton, R. M.; Allen, S. J.; Bush, M. F. Principles of Ion Selection, Alignment, and Focusing in Tandem Ion Mobility Implemented Using Structures for Lossless Ion Manipulations (SLIM). *J. Am. Soc. Mass Spectrom.* **2019**, *30* (6), 1115–1125. https://doi.org/10.1007/s13361-019-02170-1.

(63) Borotto, N. B.; Osho, K. E.; Richards, T. K.; Graham, K. A. Collision-Induced Unfolding of Native-like Protein Ions Within a Trapped Ion Mobility Spectrometry Device. *J. Am. Soc. Mass Spectrom.* **2022**, *33* (1), 83–89. https://doi.org/10.1021/jasms.1c00273.

(64) Von Helden, G.; Wyttenbach, T.; Bowers, M. T. Conformation of Macromolecules in the Gas Phase: Use of Matrix-Assisted Laser Desorption Methods in Ion Chromatography. *Science* **1995**, *267* (5203), 1483–1485. https://doi.org/10.1126/science.267.5203.1483.

(65) Shelimov, K. B.; Clemmer, D. E.; Hudgins, R. R.; Jarrold, M. F. Protein Structure *in Vacuo* : Gas-Phase Conformations of BPTI and Cytochrome *c*. *J. Am. Chem. Soc.* **1997**, *119* (9), 2240–2248. https://doi.org/10.1021/ja9619059.

(66) Shelimov, K. B.; Jarrold, M. F. Conformations, Unfolding, and Refolding of Apomyoglobin in Vacuum: An Activation Barrier for Gas-Phase Protein Folding. *J. Am. Chem. Soc.* **1997**, *119* (13), 2987–2994. https://doi.org/10.1021/ja962914k.

(67) Niu, S.; Ruotolo, B. T. Collisional Unfolding of Multiprotein Complexes Reveals Cooperative Stabilization upon Ligand Binding. *Protein Sci.* **2015**, *24* (8), 1272–1281. https://doi.org/10.1002/pro.2699.

(68) Tian, Y.; Han, L.; Buckner, A. C.; Ruotolo, B. T. Collision Induced Unfolding of Intact Antibodies: Rapid Characterization of Disulfide Bonding Patterns, Glycosylation, and Structures. *Anal. Chem.* **2015**, *87* (22), 11509–11515. https://doi.org/10.1021/acs.analchem.5b03291.

(69) Vallejo, D. D.; Polasky, D. A.; Kurulugama, R. T.; Eschweiler, J. D.; Fjeldsted, J. C.; Ruotolo, B. T. A Modified Drift Tube Ion Mobility-Mass Spectrometer for Charge-Multiplexed Collision-Induced Unfolding. *Anal. Chem.* **2019**, *91* (13), 8137–8146. https://doi.org/10.1021/acs.analchem.9b00427.

(70) Wagner, N. D.; Russell, D. H. Defining Noncovalent Ubiquitin Homodimer Interfacial Interactions through Comparisons with Covalently Linked Diubiquitin. *J. Am. Chem. Soc.* **2016**, *138* (51), 16588–16591. https://doi.org/10.1021/jacs.6b09829.

(71) Wagner, N. D.; Clemmer, D. E.; Russell, D. H. ESI-IM-MS and Collision-Induced Unfolding That Provide Insight into the Linkage-Dependent Interfacial Interactions of Covalently Linked Diubiquitin. *Anal. Chem.* **2017**, *89* (18), 10094–10103. https://doi.org/10.1021/acs.analchem.7b02932.

(72) Prell, J. S. Modeling Collisional Kinetic Energy Damping, Heating, and Cooling of Ions in Mass Spectrometers: A Tutorial Perspective. *Int. J. Mass Spectrom.* **2024**, *504*, 117290. https://doi.org/10.1016/j.ijms.2024.117290.

Chapter 3. Conformational Landscapes Observed through Controlled Kinetics (CLOCK): Using Precision Heating to Characterize Protein Dynamics in the Gas Phase

3.1 Abstract

Ion mobility spectrometry has proven useful as a technique for gaining new information about the structure and dynamics of biomolecular ions, including those of proteins and protein complexes. We have recently reported a new traveling-wave ion mobility instrument based on Structures for Lossless Ion Manipulations (SLIM) and a novel method for activating native-like protein ions to probe their conformational landscapes. This experiment involves modulating the potential applied to a set of electrodes used to confine ions and offers precise control over the distribution of structural states. Here, we combine SIMION trajectory simulations with statistical methods to estimate the effective temperature of ions under a range of conditions applicable to traveling-wave ion mobility separations. Results for 6+ ubiquitin ions indicate that ion temperature is impacted minimally by gas pressure and traveling-wave frequencies and heights during ion transmission but can be increased significantly during trapping. We correlate effective temperatures of protein ions with structural distributions that result from our on-SLIM activation experiments. Analyses of both ion velocity and position information from trajectory simulations suggest that radio-frequency (RF) heating caused by ion proximity to the SLIM electrodes enables this activation. Results from these experiments and calculations are extensible to other separations making use of traveling waves, SLIM, ion mobility, and collision-induced activation methods.

3.2 Introduction

Ion mobility (IM) spectrometry separates gas-phase ions according to size, charge, and shape. The opposing forces resulting from an electric field, E, applied in the presence of a neutral background gas will cause an ion to move with velocity, v_D, dictated by its mobility, K, under the conditions of the separation:

$$v_D = KE \tag{3.1}$$

An ion's mobility can be used to calculate an ion-neutral collision cross section, **Ω**, a proxy for size and shape information, via the Mason-Schamp equation,[1] under the low-field limit. IM is well-suited for combination with mass spectrometry (MS) due to the speed of separations and the requirement for analytes to be gas-phase ions. IM-MS can resolve structural differences of isomeric species and heterogeneous mixtures that are not distinguishable by MS alone and has been applied widely for structural biology analyses of proteins and protein complexes,[2–6] peptides,[7–11] and other biomolecules.[12–15] The introduction of Structures for Lossless Ion Manipulations (SLIM),[16] IM devices with planar symmetry fabricated as printed circuit boards, has enabled long pathlength separations capable of high resolving power[17,18] as well as complex geometries capable of isolating,[19,20] storing,[21,22] and activating[23,24] ion populations between dimensions of IM separation.

Mass spectrometry methods that use collisions to intentionally activate ions are well-established in protein sequencing and structural studies.[25–28] Activation via collisions with gas molecules is achieved by accelerating ions through an electric field to excite them prior to collisions with the gas, as in collision-induced dissociation (CID) and collision-induced unfolding (CIU). Ion-neutral collisions are not perfectly elastic and result in small increases to the internal energy of the ion. The magnitude of the increase in an ion's internal energy as a

result of collisions determines the impact of the activation on ion structure,[29] from removal of solvent and adducts and restructuring of intact assemblies at the lowest activation energies to loss of noncovalent interactions leading to unfolding and dissociation of assemblies at intermediate energies and finally, breaking of covalent interactions and fragmentation at the highest levels of activation. An alternative strategy to gas-based collisional activation in which ions are activated via collisions with a solid surface, called surface-induced dissociation, has been shown to induce dissociation of native-like protein complex ions into subunits that are consistent with native higher-order structures without significant structural rearrangement.[28]

While ion activation for CID and CIU is traditionally performed in a collision cell of a mass spectrometer, several instruments capable of ion activation prior to or between IM dimensions have been introduced, including SLIM-based systems. Smith and coworkers, who originally introduced SLIM, developed a SLIM module capable of CID and coupled it with an electrostatic SLIM IM separator.[23] Rizzo and coworkers have introduced a traveling-wave (TW) SLIM device with a multipass-enabled 1.5-m separation path and several on-board trapping regions for CID.[30] In combination with cryogenic IR spectroscopy, this technique has been used to develop a database method for identifying glycans, a molecular class known for its heterogeneity and isomerism.[24,31,32] We have previously characterized the structural evolution of protein ions in electrostatic SLIM systems, with increased trapping time between ion mobility dimensions resulting in increases in Ω for a number of different protein ion populations.[33,34]

For IM systems employing uniform electric fields, direct determination of mobility is possible according to Equation 1. As separation lengths have increased, the appeal of electrodynamic fields has increased to mitigate breakdown caused by high input voltages. In TWIM, a series of potentials of tens of volts is propagated down an electrode path. An ion in a

TWIM device is pushed forward by the traveling waves until collisions with the background gas cause it to "roll over" a wave. The number of rollover events ions experience is dictated by their mobilities, leading to dispersion in time.[35]

From the Mason-Schamp equation, Ω depends on ion temperature.[1] In electrodynamic IM separations, Ω is determined by calibration with values for standards obtained from electrostatic measurements. This procedure, combined with the low-field limit of the Mason-Schamp equation, assumes that 1) the effective ion temperature, T_{eff}, in the calibrant system is equal to T_{eff} in the target system[36] and 2) T_{eff} is equal to the gas temperature, T_{gas}.[1] Ions in a TWIM device experience electric fields that vary with time and position and may exceed the low-field limit for portions of the separation,[35,37–39] potentially violating both of these conditions and introducing error to calibrated Ω values.

Studies have shown that collisional heating of native-like protein ions in a TWIMS device can result in changes in Ω that reflect changes in the distribution of structural states occupied by the ion population.[40] Increased peptide ion fragmentation, used as an indicator for heating, has been reported with increased storage time and trapped ion population size on a TW-SLIM device.[41] This effect was mitigated through lowering the confining TW amplitude during trapping.[41] Peptide ion structural interconversion has also been observed with extended storage times in TW-SLIM, with RF-induced heating proposed as a possible cause.[42] Understanding T_{eff} in TWIM separations is necessary, particularly as structural biology applications increase, given its implications for Ω determination and ion structure.

Effective ion temperatures in IM separations have been estimated experimentally and computationally. Fragmentation yields of thermometer ions under different TW conditions combined with statistical mechanics models indicate increased ion heating during injection into

the IM region as well as with higher TW potentials, lower TW speeds, and lower background gas pressures.[37,38,43] The Prell group has developed a software tool called IonSPA and incorporated partially-inelastic collision models to calculate changes in ion temperature in CID, CIU, and IM experiments.[44] We have previously used SIMION trajectory simulations to sample ion velocities during electrostatic IM separations and construct ion-neutral relative speed distributions to determine T_{eff} for ion-neutral collisions. This method was used to demonstrate modest-to-negligible increases in T_{eff} as a result of rf-confinement for peptide and protein ions.[45]

Here, we report on the application of our model to calculate T_{eff} of ions in a TW-SLIM system. We present results from tandem IM separations of protein ions performed with varying potentials applied to laterally confining guard electrodes, which exhibit structural changes for selected protein ion populations. We then simulate ion transmission and trapping in a similar TW-SLIM region at a range of different conditions and relate the changes in ion temperature to these experimental results.

3.3 Methods

3.3.1 CLOCK Experiments

Human ubiquitin derived from *E. coli* was purchased from R&D Systems (Minneapolis, MN) and dissolved in 200 mM ammonium acetate to a final concentration of 5 μM at pH 7.0. Nanoelectrospray was used to generate gas-phase ions.[47] We have previously reported on the development of a TW-SLIM instrument capable of tandem IM separations.[46] A photograph of one of the SLIM boards with each of the independently controlled traveling wave regions is shown in Figure 3.1. Briefly, tandem IM experiments are performed by accumulating a slice of the incident ion beam up to ~12 ms wide on the SLIM boards before allowing it to separate along the first dimension of ion mobility (^{1}D). The direction of the traveling wave is used to selectively

send separated ions either to waste or into a downstream accumulation region on the SLIM boards. Mobility-selected ions accumulated between ^{1}D and the second dimension of IM (^{2}D) are activated by raising the potential applied to the guard electrodes that confines ions laterally during IM separations (Figure 3.2A). After being trapped for ~25 ms, the activated ions are released onto ^{2}D for additional separation. During separation, the guard electrode potential was held at 5 V. This value was selected empirically to optimize overall ion intensity and minimize ion activation as indicated by ion arrival times.

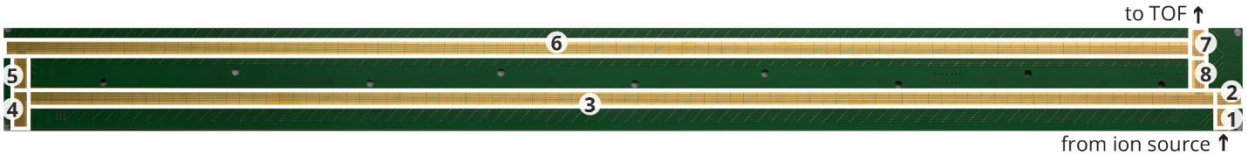

Figure 3.1. Photographs of the bottom SLIM board used in this instrument showing the full electrode path. "^{n}R" denotes the *n*th TW region, as indicated by the numbers 1-8. Tandem IM experiments, described below, were performed by allowing a packet of ions to separate along the first dimension of IM (^{3}R), selecting a desired population of ions at ^{4}R, and trapping the selected subpopulation at ^{5}R before releasing it onto the second dimension of IM (^{6}R). While ions are trapped at ^{5}R, the potential applied to the guard electrodes is modulated to control the extent of activation. Additional aspects of this instrument and its operation, including initial ion packet generation, ion selection, ion storage, and ion mobility, have been reported previously.[46]

3.3.2 Trajectory Simulations

SIMION 8.1 was used to simulate ion trajectories, with the HS1 hard-sphere program as a model for elastic ion-neutral collisions. This procedure has been described in detail elsewhere.[45] Briefly, the hard-sphere model assumes that the velocity of the background gas follows a Maxwell-Boltzmann distribution and predicts collisions as a function of temperature, pressure, and ion-neutral Ω. The potential array used to calculate electric field is based on the geometry of the TW-SLIM instrument. To minimize computation time, a segment ~64 mm in length representing 7 adjacent TW units was modeled. A close-up of a portion of the potential array is shown in Figure 3.2A. Electric fields in the TW-SLIM region were simulated using custom lua code to calculate the potentials on the guard, RF, and TW electrodes as a function of simulation time. For all simulations reported here, an RF waveform with frequency 943 kHz and amplitude 240 $V_{p\text{-}p}$ was used. TW frequency, TW height, N_2 pressure, guard electrode potential, and ion parameters including mass, charge, and Ω were varied according to the desired conditions for each simulation. The initial ion position in each set of simulations was selected by sampling the x-, y-, and z-positions of a stable transmission trajectory at a minimally activating set of TW conditions and seeding this position in the test simulation.

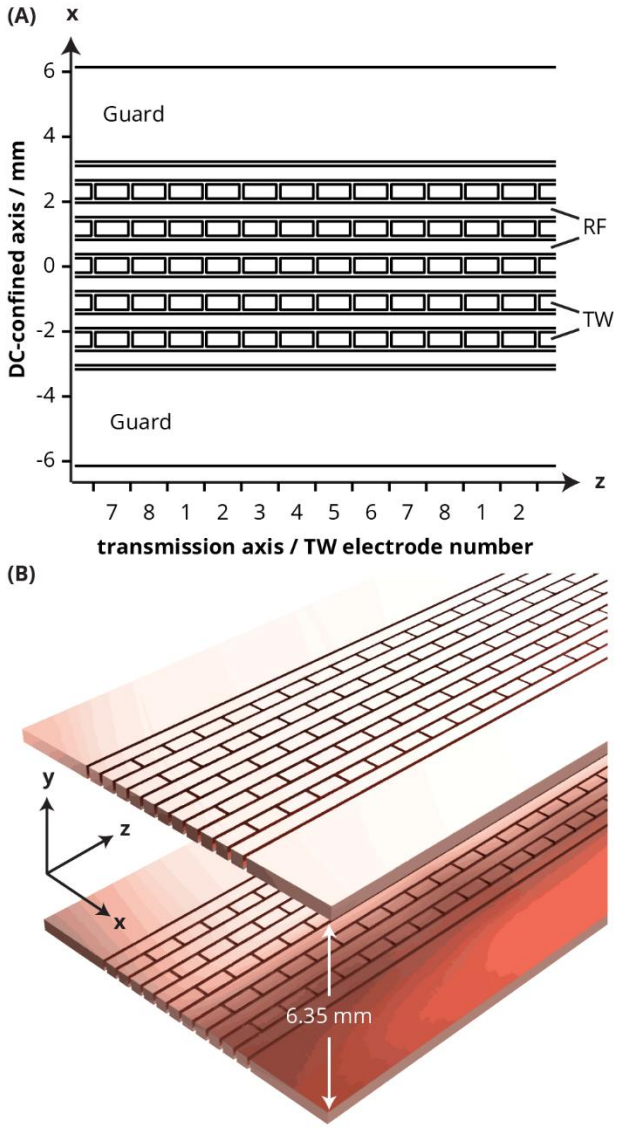

Figure 3.2. (A) Two-dimensional top-down view and (B) three-dimensional view of the electrode model used for ion trajectory simulations. Ions are transmitted along the z axis by the motion of the traveling waves and are confined in the x and y dimensions by DC potentials applied to the guard electrodes and RF potentials applied to the RF electrodes, respectively.

3.3.3 Statistical Analysis of Effective Translational Temperatures

A statistical approach reported previously was used to estimate T_{eff} under modeled simulation conditions.[45] Component velocities, V_i, where i represents the coordinates x, y, and z in the axes of the simulation, of the neutral gas were sampled from a Maxwell-Boltzmann distribution:

$$f(V_i) = \sqrt{\frac{M}{2\pi k_B T}} e^{\frac{MV_i^2}{2k_B T}} \tag{2}$$

where M is the mass of the gas molecule, k_B is the Boltzmann constant, and T is the gas temperature (298.15 K for these simulations). Component velocities, v_i, of the ion were recorded by SIMION immediately prior to an ion-neutral collision. From these, an ion-neutral relative speed, s, can be calculated:

$$s = \sqrt{\sum_i (v_i - V_i)^2} \tag{3}$$

and a distribution of s can be generated by repeating this calculation for each value of v_i, each of which corresponds to one collision modeled in the simulation. At equilibrium and with no applied electric field, the distribution of s should correspond with a Maxwell-Boltzmann relative-speed distribution:

$$f(s) = \left(\frac{\mu}{2\pi k_B T}\right)^{3/2} 4\pi s^2 e^{\frac{-\mu s^2}{2k_B T}} \tag{4}$$

where μ is the ion-neutral reduced mass and T is the equilibrated temperature. A least-squares minimization algorithm is used to adjust the value of T in Equation 4 such that the distribution of s is well described by a Maxwell-Boltzmann distribution. The temperature at which the difference between the two distributions is minimized is T_{eff}, which represents the effective translational temperature of the ion under the conditions of the simulation.

In this work, the distribution of T_{eff} for each simulation is estimated using a statistical bootstrapping method. To estimate a 95% confidence interval for the value of T_{eff}, 100 distributions of s are generated by resampling v_i and V_i with replacement, each with the same number of observations as collisions modeled in the simulation, then reoptimizing for the value of T in Equation 4 that reconstitutes each resampled distribution of s. The median of these 100 values of T_{eff} represents the estimated T_{eff} for the simulation, and the middle 95% of these 100 values of T_{eff} represents the 95% confidence interval.

3.3.4 Software Availability

A Python library for estimating effective transitional temperatures, representative data, and interactive notebooks demonstrating calculations used in this research are available from https://github.com/bushgroup/translational-temperature.

3.4 Results & Discussion

As IM experiments increase in complexity and as alternative strategies like SLIM and cyclic IMS grow in popularity, there is a need for deeper understanding of the impact of instrument parameters and experimental conditions on ion structures. Different IM experiments may benefit from either maintaining the native-like structures of analyte ions or disrupting them to study higher-energy states. Here, we employ a computational approach to characterize the extent and cause of ion effective temperature changes under conditions used in TW-SLIM experiments. We first report apparent changes in native-like protein ion structures as a result of varying conditions in tandem IM separations. We then perform ion trajectory simulations through a similar TW-SLIM region under conditions representing different portions of these experiments, use a statistical mechanical model to estimate simulated ion temperatures, and discuss the implications of these results for TW-SLIM studies.

3.4.1 CLOCK Analysis of 6+ Ubiquitin

Tandem IM experiments were conducted to isolate a population of native-like 6+ ubiquitin ions and subject it to guard-based activation. Results from these experiments are shown in Figure 3.3. After selection of the desired charge state, ions were trapped between ^{1}D and ^{2}D by stopping the motion of the traveling wave in that region with the wave potential still applied. The total trapping time for all guard activation experiments was ~25 ms. After ~1 ms of trapping, the potential applied to the guard electrodes was raised to the activating potential, and ~1 ms before restarting the motion of the waves and releasing ions to ^{2}D, the potential applied to the guard electrodes was lowered back to 5 V. The wave height was 15 $V_{p\text{-}p}$ during trapping and separation, and the TW frequency during separation was 15 kHz. The pressure of N_2 in the SLIM chamber was ~3.0 Torr.

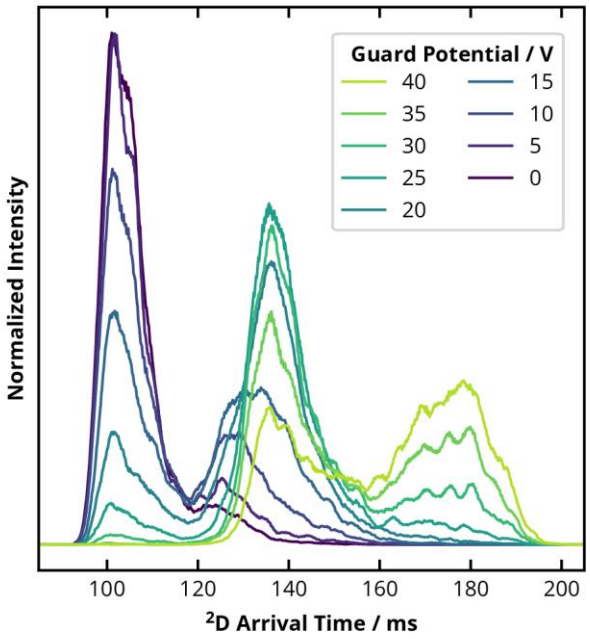

Figure 3.3. Arrival-time distributions of 6+ ubiquitin from guard-induced activation experiments. 6+ ubiquitin was selected after ^{1}D and trapped between ^{1}D

and ^{2}D for ~25 ms. The guard potentials listed in the key represent the potential applied to the guard electrodes during ion trapping between ^{1}D and ^{2}D. All experiments used a guard electrode potential of 5 V during separation.

Results from these tandem IM separations with guard-based activation indicate that 6+ ubiquitin undergoes structural shifts from an initial bimodal population with an arrival time centered at ~105 ms and ~125 ms. As the applied guard potential during trapping increases from 5 V to 15 V, the population with the shortest arrival time is depleted and the population with an arrival time centered at ~125 ms increases in intensity and shifts to ~130 ms. As the applied guard potential is raised to 25 V, the ~105 ms population continues to deplete while the ~130 ms population continues to grow and shift to ~135 ms, and a new population centered at ~175 ms grows in. Finally, as the applied guard voltage is increased to 40 V, both the ~105 ms population and the ~135 ms population are depleted in favor of the ~175 ms population.

We have previously reported structural changes of 6+ ubiquitin as a result of increasing trapping time in tandem IM separations performed on an electrostatic SLIM system and contrasted results of those time-dependent experiments with traditional energy-dependent CIU experiments.[34] In the previous time-dependent tandem IM experiments, 6+ ubiquitin ions occupied an initial compact population that was depleted in favor of a more extended population with increasing trapping time. In energy-dependent CIU experiments, 6+ ubiquitin ions occupied an initial bimodal distribution that is depleted in favor of two more extended populations with increasing laboratory frame energy. Current results from the TW-SLIM tandem IM separations with guard activation (Figure 3.3) follow the same trend observed in the energy-dependent CIU experiments reported previously. This indicates that modulating the applied guard potential while

ions are trapped enables 6+ ubiquitin ions to access structural states consistent with those observed in CIU experiments and that this manipulation can be performed selectively on populations of interest between IM dimensions.

3.4.2 Ion Effective Temperatures Increase During Trapping

Next-generation TW-SLIM experiments often incorporate periods of ion trapping as distinct subpopulations are isolated and manipulated separately.[30,48] To compare the impacts of transmission and trapping on ion effective temperature, SIMION 8.1 was used to simulate a 6+ ubiquitin ion 1) transmitted through the TW-SLIM region for 5 ms then 2) trapped in place for 5 ms. The simulated TW height was 15 $V_{p\text{-}p}$, the N_2 pressure was 3.0 Torr, and the guard bias was 5 V. During the transmission portion of the simulation, the traveling wave was propagated at a frequency of 30 kHz, and during the trapped portion of the simulation, the traveling wave voltages were applied with no propagation for 5 ms. Results from these transmit-to-trapped simulations are displayed in Figure 3.4.

Figure 3.4A shows the trajectory of 6+ ubiquitin viewed in the YZ plane between the SLIM electrodes. To calculate T_{eff}, ion x-, y-, and z-velocities were sampled separately from the first 5 ms of the simulation (transmitted, portion, plotted in blue) and the last 5 ms of the simulation (trapped portion, plotted in red). Neutral gas velocities were sampled from a Maxwell-Boltzmann distribution at 298 K as described in the Methods section. The resulting ion-neutral relative speed distributions are shown in Figure 3.4B and overlaid with the Maxwell-Boltzmann relative speed distributions at the temperatures calculated to minimize the differences to the simulated ion-neutral relative speed distributions. These distributions indicate that under the applied TW conditions, the effective temperature of 6+ ubiquitin is increased by 53 K during trapping as compared to transmission.

Figure 3.4A and 3.4B show results for a transmit-to-trapped simulation of 6+ ubiquitin using traveling waves with a square profile (i.e. +7.5 V applied to four adjacent TW electrodes and -7.5 V applied to four adjacent TW electrodes). Similar simulations were performed using three alternative TW profiles: sawtooth, sine, and triangle, as evaluated experimentally by others.[49] Figure 3.4C shows the median effective temperature calculated for each 0.5-ms segment of the 10-ms transmit-to-trapped simulations performed with four different TW profiles. For all waveform profiles simulated, the median effective temperature of 6+ ubiquitin increases when trapped versus when transmitted under the conditions simulated. For the pulse, sine, and triangle waveform profiles, the ΔT_{eff} between trapping and transmission were 52, 55, and 54 K, respectively, while the increase in T_{eff} for the sawtooth waveform was 61 K. See Table B.1.1 and Table B.1.2 for calculated T_{eff} values for transmission and trapping for each waveform profile. For all other experiments and simulations reported here, the pulse waveform profile was used.

Interestingly, previous work has demonstrated slight differences in achievable Ω error[49] peak-to-peak resolution[50] for measurements of lipids and small molecules based on waveform profile, with the sawtooth shape exhibiting better performance for both metrics. Previous work has also shown that transmission in a TW-SLIM device with different waveform profiles results in modest increases to T_{eff} above the neutral gas temperature,[49] consistent with results reported here. Results from these simulations implicate trapping in significant increases in T_{eff}, which is supported by observations of peptide ion structural interconversion during trapping in a TW-SLIM device.[42]

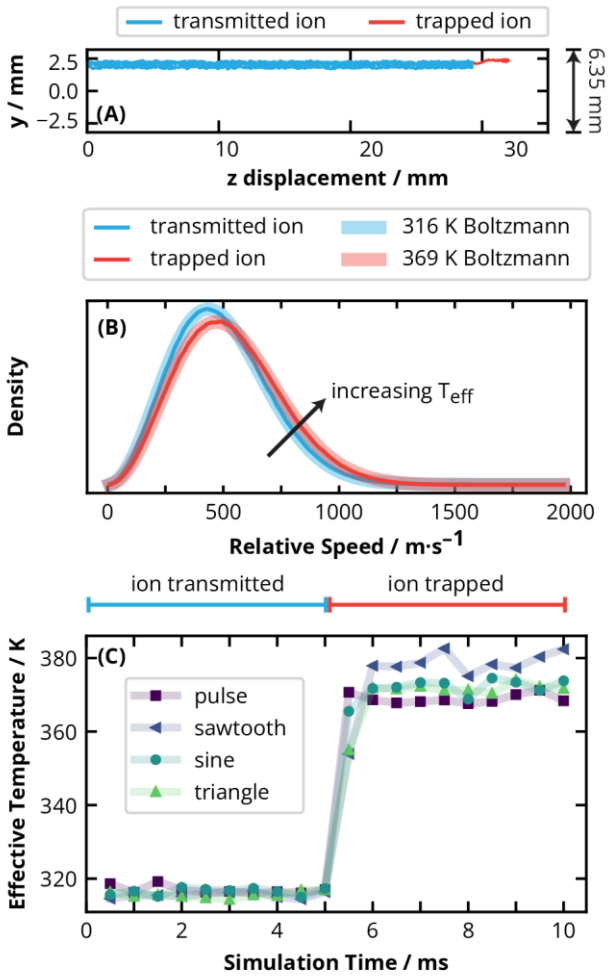

Figure 3.4. Results from simulations of 6+ ubiquitin transmitted through the TW-SLIM region for 5 ms, then trapped for 5 ms. Transmission was simulated with a wave height of 15 V_{p-p} and frequency of 30 kHz in 3.0 Torr N_2. Trapping was simulated by halting the traveling wave in place, keeping the wave height statically applied to the TW electrodes. (A) The trajectory of 6+ ubiquitin visualized in the YZ plane. The portion of the trajectory shown in blue represents the first 5 ms of the simulation with the traveling wave moving at 30 kHz and the portion of the trajectory shown in red represents the last 5 ms of the simulation with the traveling wave static. (B) The ion-neutral relative speed distributions for the first 5 ms of the

simulation (blue) and the last 5 ms of the simulation (red), overlaid with the Maxwell-Boltzmann relative-speed distributions used to determine the effective temperature for each portion of the simulation. (C) Median effective temperatures calculated for each 0.5-ms segment of simulations performed with one of four TW profiles: pulse (square), sawtooth, sine, or triangle.

To further characterize T_{eff} during ion transmission, simulations were performed at a range of TW conditions. Figure B.1.1 shows the median effective temperature of 6+ ubiquitin transmitted through the TW-SLIM region at TW frequency values up to 50 kHz for two different values of TW height and N_2 pressure. These results suggest little dependence of T_{eff} on TW frequency for frequencies accessible in TW-SLIM experiments (the frequency output range for the power supplies used to experimentally generate the traveling waves is 10 to 40 kHz).

3.4.3 Effects of Applied Potentials on Effective Temperatures of Trapped Ions

From the results of the CLOCK experiments (Figure 3.3) and the transmit-to-trapped simulations (Figure 3.4), simulations of ions trapped in the TW-SLIM region were performed with varying guard electrode potentials. Trapping simulations were performed with static square waves applied to the TW electrodes and RF waveforms identical to those used for transmission simulations and described previously. To assess the impact of guard electrode potential on T_{eff} of trapped ions, a default guard potential of 5V was applied. The guard potential was then either raised, lowered, or kept constant. Each voltage was held for 3.2 ms before a final 3.2-ms segment with the guard potential at 5 V. Based on observed power supply rise times, the potential was ramped linearly between values over 0.4 ms, for a total simulation time of 10.4 ms.

Results from these trapped simulations are presented in Figure 3.5. Panel A shows the applied guard potential plotted as a function of simulation time. Panel B contains the distributions of the relative speed of the 6+ ubiquitin ion and the N_2 overlaid with the Maxwell-Boltzmann relative speed distributions at the corresponding T_{eff} determined as described previously. During the pre-CLOCK segment of the simulation, T_{eff} is 347 K, which is elevated ~50 K above room temperature, while during the CLOCK segment at a simulated guard potential of 25 V, T_{eff} is 445 K, which is elevated ~150 K above room temperature. During the post-CLOCK segment, when the simulated guard potential is lowered back to 5 V, T_{eff} is 346 K, very similar to that during the pre-CLOCK segment. Residuals between the simulated ion-neutral relative speed distribution and the Maxwell-Boltzmann relative speed distribution used to determine T_{eff} for each portion of the simulation are shown in Figure 3.5C. The median value and 95% confidence interval of T_{eff} calculated for each 104 μs segment of the simulation is shown in Figure 3.5D and shows that T_{eff} changes on the timescale of the change in the simulated guard electrode potential.

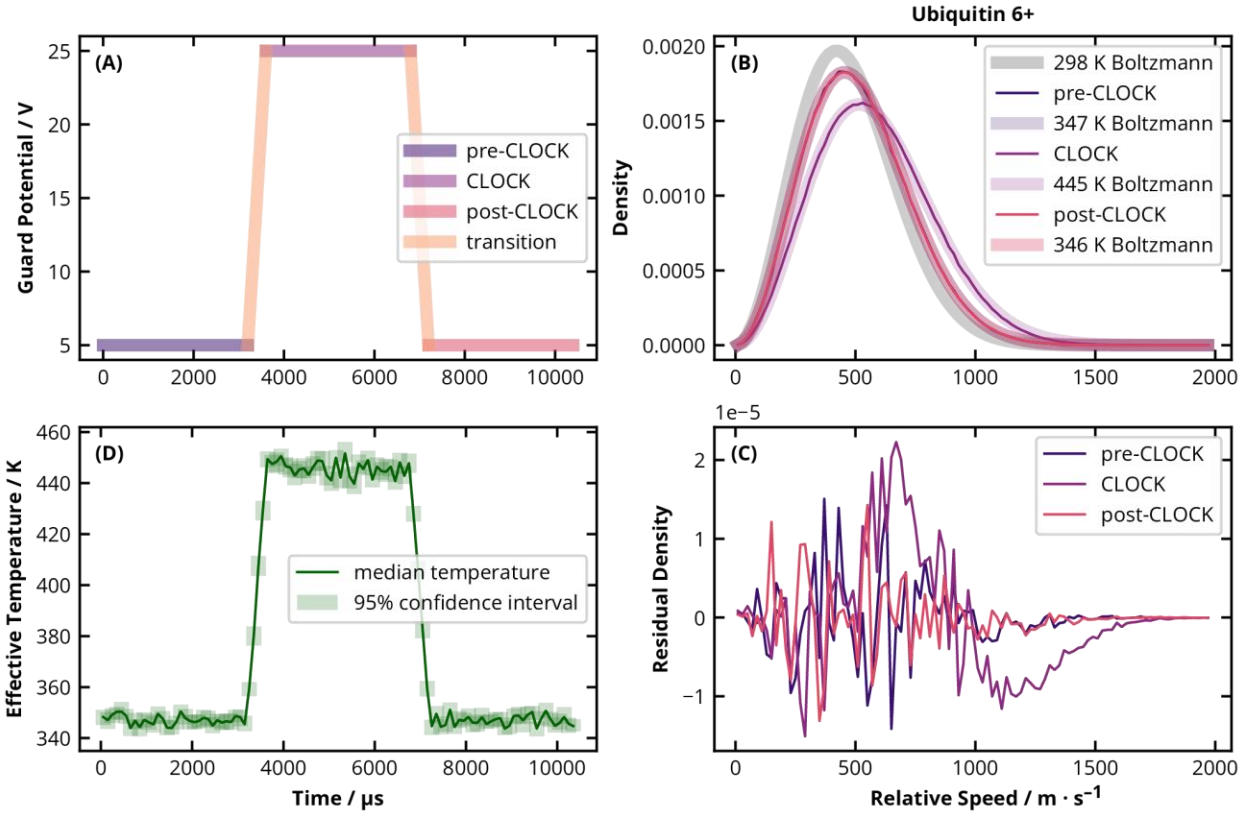

Figure 3.5. The effect of applied guard potential during trapping in the TW-SLIM region on median effective temperature of 6+ UBQ. Trapping was simulated with a TW height of 10 $V_{p\text{-}p}$ and 2.5 Torr N_2. (A) Applied guard potential plotted as a function of simulation time. The guard electrodes were held at 5 V for 3.2 ms, ramped to 25 V over 0.4 ms, held at 25 V for 3.2 ms, ramped back down to 5 V over 0.4 ms, and held at 5 V for the final 3.2 ms. (B) Ion-neutral relative speed distributions constructed for the pre-CLOCK, CLOCK, and post-CLOCK segments of the ion trajectory and overlaid with the Maxwell-Boltzmann relative-speed distribution used to determine T_{eff} for each segment, respectively. The Maxwell-Boltzmann relative speed distribution at room temperature (298 K) is also shown for reference. (C) Residuals between the ion-neutral relative speed distributions and corresponding Maxwell-Boltzmann relative speed distributions from (B). (D) T_{eff}

calculated for each 104 μs segment of the simulated plotted as a function of simulation time and overlaid with the 95% confidence interval for each segment. Figure B.1.2 shows the analysis workflow for a similar simulation performed with 1+ bradykinin.

To further understand the cause of the observed increases in T_{eff} at higher applied guard potentials, ion velocities were visualized in the x, y, and z dimensions (see Figure 3.2 for orientation). Figure 3.6 shows the distributions of the 6+ ubiquitin ion velocity in each dimension during trapping simulations with a wave height of 10 V_{p-p} and 2.5 Torr N_2 with the potential applied to the guard electrodes ranging from 0 to 40 V. In both the x and z dimensions, the ion velocity is centered around 0 $m \cdot s^{-1}$ and unimodal in shape. In the y dimension, the velocity distribution is bimodal and symmetric about 0 $m \cdot s^{-1}$, with maxima and increased density occurring at higher absolute values with increasing guard potentials. In addition to velocity, ion positions during simulated trapping were monitored. Figure B.1.4 shows the distributions of positions in the y dimension occupied by 6+ ubiquitin and 1+ bradykinin ions while trapped with a wave height of 10 V_{p-p} and 2.5 Torr N_2 with the potential applied to the guard electrodes ranging from 0 to 40 V. Overall, both ions have a median position closer to the electrodes when trapped with a higher applied guard potential. The 1+ bradykinin ion has a wider distribution of y positions at all guard potentials simulated. One possible explanation for the higher T_{eff} observed with increased guard potential is that the concomitant shift in ion position closer to the electrodes results in higher electric fields from the RF waveforms used to confine ions in the y-dimension. This is consistent with previous work proposing RF-induced heating as a cause for structural changes observed during ion trapping in TW-SLIM devices.[42] The impact of wave height on ion

y position was also investigated for 6+ ubiquitin; T_{eff} and y position data at four different wave heights and two different pressures are shown in Figure B.1.5.

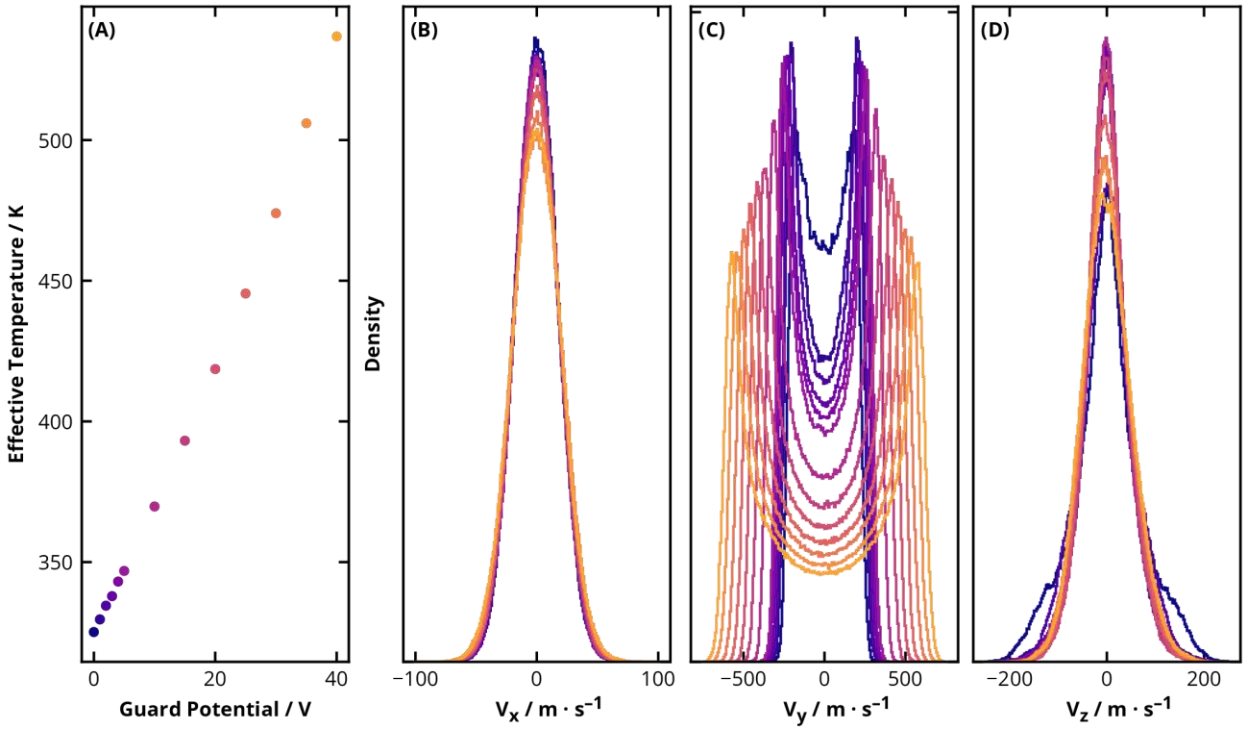

Figure 3.6. Distributions of the simulated 6+ ubiquitin ion velocity while trapped with a wave height of 10 10 V_{p-p} and 2.5 Torr N_2 and applied guard potential ranging from 0 to 40 V. (A) T_{eff} plotted as a function of applied guard potential. (B-D) Distributions of the ion velocity in the x, y, and z dimensions, respectively.

3.5 Conclusions

The effects of different traveling-wave SLIM experimental conditions on effective ion temperatures were examined using simulated ion trajectories. During simulated ion transmission through a TW-SLIM device, 6+ ubiquitin effective temperatures were elevated ~20 K above ambient temperatures (Figure 3.4). During simulated ion trapping on the same device, 6+

ubiquitin temperatures were elevated at least ~70 K above ambient temperatures (Figure 3.4). Conditions matching those employed in a recently-reported novel on-SLIM ion activation method (Figure 3.3) were also simulated. By modulating the potential applied to the guard electrodes, ion temperatures up to ~400 K above ambient were achieved (Figure 3.5, B.1.2, B.1.3). By visualizing the distributions of ion velocity (Figure 3.6) and position (Figure B.1.4), the source of the ion activation could be attributed to additional heating from the rf-confining electrodes as increased guard electrode potentials cause ions to move closer to the boards. The work reported here has implications for ion mobility experiments performed on this and other SLIM and similar devices, and offers the opportunity to quantitatively describe ion activation that has not been realized in other collision-induced activation experiments.

3.6 Acknowledgements

This material is based upon work supported by the National Institute of General Medical Sciences of the National Institutes of Health through award R01GM130708 (M.F.B.), the National Science Foundation through award 2203513 (M.F.B.) from the Division of Chemistry, with partial co-funding from the Division of Molecular and Cellular Biosciences, and the National Science Foundation through award 2140004 (A.E.R.) from the Division of Graduate Education.

3.7 References

(1) Mason, E. A.; McDaniel, E. W. *Transport Properties of Ions in Gases*, 1st ed.; Wiley, 1988. https://doi.org/10.1002/3527602852.

(2) Ruotolo, B. T.; Benesch, J. L. P.; Sandercock, A. M.; Hyung, S.-J.; Robinson, C. V. Ion Mobility–Mass Spectrometry Analysis of Large Protein Complexes. *Nat. Protoc.* **2008**, *3* (7), 1139–1152. https://doi.org/10.1038/nprot.2008.78.

(3) Smith, D. P.; Radford, S. E.; Ashcroft, A. E. Elongated Oligomers in β_2 -Microglobulin Amyloid Assembly Revealed by Ion Mobility Spectrometry-Mass Spectrometry. *Proc. Natl. Acad. Sci.* **2010**, *107* (15), 6794–6798. https://doi.org/10.1073/pnas.0913046107.

(4) Song, Y.; Nelp, M. T.; Bandarian, V.; Wysocki, V. H. Refining the Structural Model of a Heterohexameric Protein Complex: Surface Induced Dissociation and Ion Mobility Provide Key Connectivity and Topology Information. *ACS Cent. Sci.* **2015**, *1* (9), 477–487. https://doi.org/10.1021/acscentsci.5b00251.

(5) Pacholarz, K. J.; Peters, S. J.; Garlish, R. A.; Henry, A. J.; Taylor, R. J.; Humphreys, D. P.; Barran, P. E. Molecular Insights into the Thermal Stability of mAbs with Variable-Temperature Ion-Mobility Mass Spectrometry. *ChemBioChem* **2016**, *17* (1), 46–51. https://doi.org/10.1002/cbic.201500574.

(6) Rolland, A. D.; Biberic, L. S.; Prell, J. S. Investigation of Charge-State-Dependent Compaction of Protein Ions with Native Ion Mobility–Mass Spectrometry and Theory. *J. Am. Soc. Mass Spectrom.* **2022**, *33* (2), 369–381. https://doi.org/10.1021/jasms.1c00351.

(7) Wu, C.; Siems, W. F.; Klasmeier, J.; Hill, H. H. Separation of Isomeric Peptides Using Electrospray Ionization/High-Resolution Ion Mobility Spectrometry. *Anal. Chem.* **2000**, *72* (2), 391–395. https://doi.org/10.1021/ac990601c.

(8) Ruotolo, B. T.; Gillig, K. J.; Woods, A. S.; Egan, T. F.; Ugarov, M. V.; Schultz, J. A.; Russell, D. H. Analysis of Phosphorylated Peptides by Ion Mobility-Mass Spectrometry. *Anal. Chem.* **2004**, *76* (22), 6727–6733. https://doi.org/10.1021/ac0498009.

(9) Silveira, J. A.; Ridgeway, M. E.; Park, M. A. High Resolution Trapped Ion Mobility Spectrometery of Peptides. *Anal. Chem.* **2014**, *86* (12), 5624–5627. https://doi.org/10.1021/ac501261h.

(10) Mast, D. H.; Liao, H.-W.; Romanova, E. V.; Sweedler, J. V. Analysis of Peptide Stereochemistry in Single Cells by Capillary Electrophoresis–Trapped Ion Mobility Spectrometry Mass Spectrometry. *Anal. Chem.* **2021**, *93* (15), 6205–6213. https://doi.org/10.1021/acs.analchem.1c00445.

(11) Tomczyk, N.; Giles, K.; Richardson, K.; Ujma, J.; Palmer, M.; Nielsen, P. K.; Haselmann, K. F. Mapping Isomeric Peptides Derived from Biopharmaceuticals Using High-Resolution Ion Mobility Mass Spectrometry. *Anal. Chem.* **2021**, *93* (49), 16379–16384. https://doi.org/10.1021/acs.analchem.1c02834.

(12) Paglia, G.; Angel, P.; Williams, J. P.; Richardson, K.; Olivos, H. J.; Thompson, J. W.; Menikarachchi, L.; Lai, S.; Walsh, C.; Moseley, A.; Plumb, R. S.; Grant, D. F.; Palsson, B. O.; Langridge, J.; Geromanos, S.; Astarita, G. Ion Mobility-Derived Collision Cross Section As an Additional Measure for Lipid Fingerprinting and Identification. *Anal. Chem.* **2015**, *87* (2), 1137–1144. https://doi.org/10.1021/ac503715v.

(13) Hofmann, J.; Hahm, H. S.; Seeberger, P. H.; Pagel, K. Identification of Carbohydrate Anomers Using Ion Mobility–Mass Spectrometry. *Nature* **2015**, *526* (7572), 241–244. https://doi.org/10.1038/nature15388.

(14) Hines, K. M.; Ross, D. H.; Davidson, K. L.; Bush, M. F.; Xu, L. Large-Scale Structural Characterization of Drug and Drug-Like Compounds by High-Throughput Ion Mobility-Mass Spectrometry. *Anal. Chem.* **2017**, *89* (17), 9023–9030. https://doi.org/10.1021/acs.analchem.7b01709.

(15) Kenderdine, T.; Nemati, R.; Baker, A.; Palmer, M.; Ujma, J.; FitzGibbon, M.; Deng, L.; Royzen, M.; Langridge, J.; Fabris, D. High-resolution Ion Mobility Spectrometry-mass

Spectrometry of Isomeric/Isobaric Ribonucleotide Variants. *J. Mass Spectrom.* **2020**, *55* (2), e4465. https://doi.org/10.1002/jms.4465.

(16) Webb, I. K.; Garimella, S. V. B.; Tolmachev, A. V.; Chen, T.-C.; Zhang, X.; Norheim, R. V.; Prost, S. A.; LaMarche, B.; Anderson, G. A.; Ibrahim, Y. M.; Smith, R. D. Experimental Evaluation and Optimization of Structures for Lossless Ion Manipulations for Ion Mobility Spectrometry with Time-of-Flight Mass Spectrometry. *Anal. Chem.* **2014**, *86* (18), 9169–9176. https://doi.org/10.1021/ac502055e.

(17) Deng, L.; Ibrahim, Y. M.; Hamid, A. M.; Garimella, S. V. B.; Webb, I. K.; Zheng, X.; Prost, S. A.; Sandoval, J. A.; Norheim, R. V.; Anderson, G. A.; Tolmachev, A. V.; Baker, E. S.; Smith, R. D. Ultra-High Resolution Ion Mobility Separations Utilizing Traveling Waves in a 13 m Serpentine Path Length Structures for Lossless Ion Manipulations Module. *Anal. Chem.* **2016**, *88* (18), 8957–8964. https://doi.org/10.1021/acs.analchem.6b01915.

(18) Deng, L.; Webb, I. K.; Garimella, S. V. B.; Hamid, A. M.; Zheng, X.; Norheim, R. V.; Prost, S. A.; Anderson, G. A.; Sandoval, J. A.; Baker, E. S.; Ibrahim, Y. M.; Smith, R. D. Serpentine Ultralong Path with Extended Routing (SUPER) High Resolution Traveling Wave Ion Mobility-MS Using Structures for Lossless Ion Manipulations. *Anal. Chem.* **2017**, *89* (8), 4628–4634. https://doi.org/10.1021/acs.analchem.7b00185.

(19) Webb, I. K.; Garimella, S. V. B.; Tolmachev, A. V.; Chen, T.-C.; Zhang, X.; Cox, J. T.; Norheim, R. V.; Prost, S. A.; LaMarche, B.; Anderson, G. A.; Ibrahim, Y. M.; Smith, R. D. Mobility-Resolved Ion Selection in Uniform Drift Field Ion Mobility Spectrometry/Mass Spectrometry: Dynamic Switching in Structures for Lossless Ion Manipulations. *Anal. Chem.* **2014**, *86* (19), 9632–9637. https://doi.org/10.1021/ac502139e.

(20) Eaton, R. M.; Allen, S. J.; Bush, M. F. Principles of Ion Selection, Alignment, and Focusing in Tandem Ion Mobility Implemented Using Structures for Lossless Ion Manipulations (SLIM). *J. Am. Soc. Mass Spectrom.* **2019**, *30* (6), 1115–1125. https://doi.org/10.1007/s13361-019-02170-1.

(21) Zhang, X.; Garimella, S. V. B.; Prost, S. A.; Webb, I. K.; Chen, T.-C.; Tang, K.; Tolmachev, A. V.; Norheim, R. V.; Baker, E. S.; Anderson, G. A.; Ibrahim, Y. M.; Smith, R. D. Ion Trapping, Storage, and Ejection in Structures for Lossless Ion Manipulations. *Anal. Chem.* **2015**, *87* (12), 6010–6016. https://doi.org/10.1021/acs.analchem.5b00214.

(22) Chen, T.-C.; Ibrahim, Y. M.; Webb, I. K.; Garimella, S. V. B.; Zhang, X.; Hamid, A. M.; Deng, L.; Karnesky, W. E.; Prost, S. A.; Sandoval, J. A.; Norheim, R. V.; Anderson, G. A.; Tolmachev, A. V.; Baker, E. S.; Smith, R. D. Mobility-Selected Ion Trapping and Enrichment Using Structures for Lossless Ion Manipulations. *Anal. Chem.* **2016**, *88* (3), 1728–1733. https://doi.org/10.1021/acs.analchem.5b03910.

(23) Webb, I. K.; Garimella, S. V. B.; Norheim, R. V.; Baker, E. S.; Ibrahim, Y. M.; Smith, R. D. A Structures for Lossless Ion Manipulations (SLIM) Module for Collision Induced Dissociation. *J. Am. Soc. Mass Spectrom.* **2016**, *27* (7), 1285–1288. https://doi.org/10.1007/s13361-016-1397-x.

(24) Pellegrinelli, R. P.; Yue, L.; Carrascosa, E.; Ben Faleh, A.; Warnke, S.; Bansal, P.; Rizzo, T. R. A New Strategy Coupling Ion-Mobility-Selective CID and Cryogenic IR Spectroscopy to Identify Glycan Anomers. *J. Am. Soc. Mass Spectrom.* **2022**, *33* (5), 859–864. https://doi.org/10.1021/jasms.2c00043.

(25) Mitchell Wells, J.; McLuckey, S. A. Collision-Induced Dissociation (CID) of Peptides and Proteins. In *Methods in Enzymology*; Elsevier, 2005; Vol. 402, pp 148–185. https://doi.org/10.1016/S0076-6879(05)02005-7.

(26) Johnson, A. R.; Carlson, E. E. Collision-Induced Dissociation Mass Spectrometry: A Powerful Tool for Natural Product Structure Elucidation. *Anal. Chem.* **2015**, *87* (21), 10668–10678. https://doi.org/10.1021/acs.analchem.5b01543.

(27) Dixit, S. M.; Polasky, D. A.; Ruotolo, B. T. Collision Induced Unfolding of Isolated Proteins in the Gas Phase: Past, Present, and Future. *Curr. Opin. Chem. Biol.* **2018**, *42*, 93–100. https://doi.org/10.1016/j.cbpa.2017.11.010.

(28) Zhou, M.; Wysocki, V. H. Surface Induced Dissociation: Dissecting Noncovalent Protein Complexes in the Gas Phase. *Acc. Chem. Res.* **2014**, *47* (4), 1010–1018. https://doi.org/10.1021/ar400223t.

(29) Benesch, J. L. P. Collisional Activation of Protein Complexes: Picking up the Pieces. *J. Am. Soc. Mass Spectrom.* **2009**, *20* (3), 341–348. https://doi.org/10.1016/j.jasms.2008.11.014.

(30) Bansal, P.; Yatsyna, V.; AbiKhodr, A. H.; Warnke, S.; Ben Faleh, A.; Yalovenko, N.; Wysocki, V. H.; Rizzo, T. R. Using SLIM-Based IMS-IMS Together with Cryogenic Infrared Spectroscopy for Glycan Analysis. *Anal. Chem.* **2020**, *92* (13), 9079–9085. https://doi.org/10.1021/acs.analchem.0c01265.

(31) Bansal, P.; Ben Faleh, A.; Warnke, S.; Rizzo, T. R. Identification of *N* -Glycan Positional Isomers by Combining IMS and Vibrational Fingerprinting of Structurally Determinant CID Fragments. *The Analyst* **2022**, *147* (4), 704–711. https://doi.org/10.1039/D1AN01861B.

(32) Bansal, P.; Ben Faleh, A.; Warnke, S.; Rizzo, T. R. Multistage Ion Mobility Spectrometry Combined with Infrared Spectroscopy for Glycan Analysis. *J. Am. Soc. Mass Spectrom.* **2023**, *34* (4), 695–700. https://doi.org/10.1021/jasms.2c00361.

(33) Allen, S. J.; Eaton, R. M.; Bush, M. F. Structural Dynamics of Native-Like Ions in the Gas Phase: Results from Tandem Ion Mobility of Cytochrome *c*. *Anal. Chem.* **2017**, *89* (14), 7527–7534. https://doi.org/10.1021/acs.analchem.7b01234.

(34) Zercher, B. P.; Hong, S.; Roush, A. E.; Feng, Y.; Bush, M. F. Are the Gas-Phase Structures of Molecular Elephants Enduring or Ephemeral? Results from Time-Dependent, Tandem Ion Mobility. *Anal. Chem.* **2023**, *95* (25), 9589–9597. https://doi.org/10.1021/acs.analchem.3c01222.

(35) Shvartsburg, A. A.; Smith, R. D. Fundamentals of Traveling Wave Ion Mobility Spectrometry. *Anal. Chem.* **2008**, *80* (24), 9689–9699. https://doi.org/10.1021/ac8016295.

(36) Gabelica, V.; Shvartsburg, A. A.; Afonso, C.; Barran, P.; Benesch, J. L. P.; Bleiholder, C.; Bowers, M. T.; Bilbao, A.; Bush, M. F.; Campbell, J. L.; Campuzano, I. D. G.; Causon, T.; Clowers, B. H.; Creaser, C. S.; De Pauw, E.; Far, J.; Fernandez-Lima, F.; Fjeldsted, J. C.; Giles, K.; Groessl, M.; Hogan, C. J.; Hann, S.; Kim, H. I.; Kurulugama, R. T.; May, J. C.; McLean, J. A.; Pagel, K.; Richardson, K.; Ridgeway, M. E.; Rosu, F.; Sobott, F.; Thalassinos, K.; Valentine, S. J.; Wyttenbach, T. Recommendations for Reporting Ion Mobility Mass Spectrometry Measurements. *Mass Spectrom. Rev.* **2019**, *38* (3), 291–320. https://doi.org/10.1002/mas.21585.

(37) Morsa, D.; Gabelica, V.; De Pauw, E. Effective Temperature of Ions in Traveling Wave Ion Mobility Spectrometry. *Anal. Chem.* **2011**, *83* (14), 5775–5782. https://doi.org/10.1021/ac201509p.

(38) Merenbloom, S. I.; Flick, T. G.; Williams, E. R. How Hot Are Your Ions in TWAVE Ion Mobility Spectrometry? *J. Am. Soc. Mass Spectrom.* **2012**, *23* (3), 553–562. https://doi.org/10.1007/s13361-011-0313-7.

(39) Webb, I. K. Perspective: The Complex Relationship between Charge, Mobility, and Gas-phase Protein Structure. *J. Mass Spectrom.* **2024**, *59* (5), e5013. https://doi.org/10.1002/jms.5013.

(40) Chen, S.-H.; Russell, D. H. How Closely Related Are Conformations of Protein Ions Sampled by IM-MS to Native Solution Structures? *J. Am. Soc. Mass Spectrom.* **2015**, *26* (9), 1433–1443. https://doi.org/10.1007/s13361-015-1191-1.

(41) Kwantwi-Barima, P.; Garimella, S. V. B.; Attah, I. K.; Zheng, X.; Ibrahim, Y. M.; Smith, R. D. Accumulation of Large Ion Populations with High Ion Densities and Effects Due to Space Charge in Traveling Wave-Based Structures for Lossless Ion Manipulations (SLIM) IMS-MS. *J. Am. Soc. Mass Spectrom.* **2024**, *35* (2), 365–377. https://doi.org/10.1021/jasms.3c00389.

(42) Kinlein, Z.; Clowers, B. H. Altering Conformational States of Dynamic Ion Populations Using Traveling Wave Structures for Lossless Ion Manipulations. *Anal. Chem.* **2024**, *96* (16), 6450–6458. https://doi.org/10.1021/acs.analchem.4c00692.

(43) Morsa, D.; Gabelica, V.; De Pauw, E. Fragmentation and Isomerization Due to Field Heating in Traveling Wave Ion Mobility Spectrometry. *J. Am. Soc. Mass Spectrom.* **2014**, *25* (8), 1384–1393. https://doi.org/10.1007/s13361-014-0909-9.

(44) Prell, J. S. Modeling Collisional Kinetic Energy Damping, Heating, and Cooling of Ions in Mass Spectrometers: A Tutorial Perspective. *Int. J. Mass Spectrom.* **2024**, *504*, 117290. https://doi.org/10.1016/j.ijms.2024.117290.

(45) Allen, S. J.; Bush, M. F. Radio-Frequency (Rf) Confinement in Ion Mobility Spectrometry: Apparent Mobilities and Effective Temperatures. *J. Am. Soc. Mass Spectrom.* **2016**, *27* (12), 2054–2063. https://doi.org/10.1007/s13361-016-1479-9.

(46) Wageman, A.; Roush, A. E.; Feng, Y.; Bush, M. F. SLIMPHONY: A New SLIM-Based Instrument That Orchestrates Complex Ion Mobility – Mass Spectrometry Experiments. manuscript in preparation.

(47) Davidson, K. L.; Oberreit, D. R.; Hogan, C. J.; Bush, M. F. Nonspecific Aggregation in Native Electrokinetic Nanoelectrospray Ionization. *Int. J. Mass Spectrom.* **2017**, *420*, 35–42. https://doi.org/10.1016/j.ijms.2016.09.013.

(48) Huntley, A. P.; Hollerbach, A. L.; Prabhakaran, A.; Garimella, S. V. B.; Giberson, C. M.; Norheim, R. V.; Smith, R. D.; Ibrahim, Y. M. Development of a Structure for Lossless Ion Manipulations (SLIM) High Charge Capacity Array of Traps. *Anal. Chem.* **2023**, *95* (9), 4446–4453. https://doi.org/10.1021/acs.analchem.2c05025.

(49) Kwantwi-Barima, P.; Harrilal, C. P.; Garimella, S. V. B.; Attah, I. K.; Smith, R. D.; Ibrahim, Y. M. Effect of Traveling Waveform Profiles on Collision Cross Section Measurements in Structures for Lossless Ion Manipulations. *J. Am. Soc. Mass Spectrom.* **2022**, *33* (5), 783–792. https://doi.org/10.1021/jasms.1c00364.

(50) Conant, C. R.; Attah, I. K.; Garimella, S. V. B.; Nagy, G.; Bilbao, A.; Smith, R. D.; Ibrahim, Y. M. Evaluation of Waveform Profiles for Traveling Wave Ion Mobility Separations in Structures for Lossless Ion Manipulations. *J. Am. Soc. Mass Spectrom.* **2021**, *32* (1), 225–236. https://doi.org/10.1021/jasms.0c00282.

Appendix A: Supporting Information for Chapter 2

A.1 Supplementary Information

Additional Methods

Experimental Timing Details for Combining Multiple Passes and Activation in Selection-Trapping, IM-IM-MS. The experiments performed to generate the data shown in Figure 2.5B–G require ion selection at one of two locations after initial IM separation. The results shown in Figure 2.5B–D followed ion selection at ^{4}R, and the results shown in Figure 2.5E–G followed ion selection at ^{7}R. Ions selected at ^{4}R have undergone ~83 cm of separation prior to trapping, and ions selected at ^{7}R have undergone ~169 cm of separation prior to trapping. Due to diffusion-based broadening, the ion population selected at ^{7}R is temporally wider than the ion population selected at ^{4}R. Therefore, when selecting ions at ^{7}R, additional time must be allocated for unselected ions to exit the boards (via ^{7}R) prior to activating the selected ions trapped at ^{8}R. This is accomplished by keeping the wave applied to ^{8}R stationary for ~24 ms while maintaining the applied guard potential at 5 V before the guard potential is raised to the activation value for ~25 ms. The guard potential is then reset to 5 V for the last ~1 ms prior to ion release. To enable a more direct comparison between activation at different regions within SLIMPHONY, the same delay time and activation duration were used for the experiments shown in Figure 2.5B–D.

Table A.1.1. The TW and guard electrode potential parameters for the separation portions of all experiments shown in Figure 2.4B–D are summarized in the table below.

Separation

TW Height / V_{p-p}	TW Frequency / kHz	Guard Potential / V
15	15	5

Table A.1.2. The trapping, TW and guard electrode potential, and activation parameters for the trapped portions of the experiments shown in Figure 2.4B–D are summarized in the table below. Italicized values represent the range of values for each parameter that was varied in the experiments shown in Figure 2.4B–D, respectively.

Trapping

	TW Height / V_{p-p}	Delay Time / ms	Guard Potential / V	Activation Time / ms
4B	15	*5 – 525*	5	
4C	15	70	*0 – 40*	69
4D	15	70	30	*0 – 69*

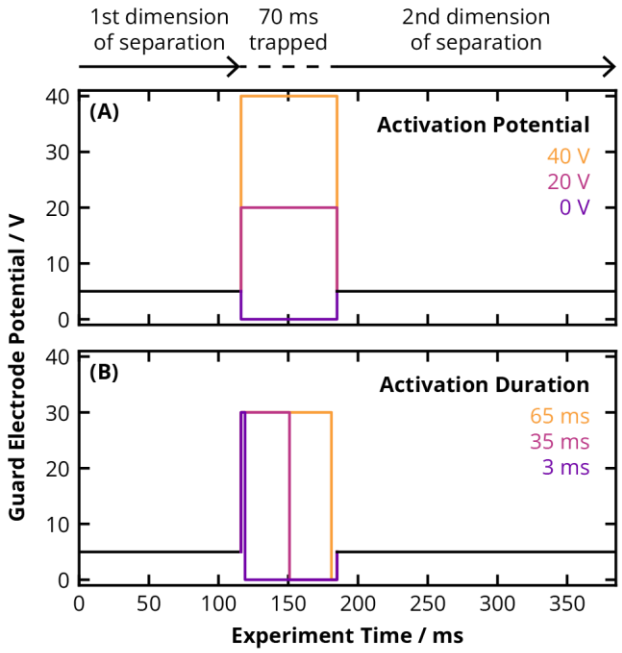

Figure A.1.1. Example timing profiles of the DC potential applied to the guard electrodes for the experiments whose results are shown in (A) Figure 2.4C and (B) Figure 2.4D.

Appendix B: Supporting Information for Chapter 3

B.1 Supplementary Information

Table B.1.1. Total z displacement and median and 95% confidence interval of effective temperatures of 6+ ubiquitin during 5-ms transmission simulation for four different waveform profiles.

Transmission

Waveform profile	z displacement / mm	Median T_{eff} / K	T_{eff} 95% CI / K
Pulse	29	316.9	316.5 – 317.3
Sawtooth	5	315.5	315.2 – 315.9
Sine	17	316.5	316.2 – 316.8
Triangle	11	315.6	315.2 – 316.1

Table B.1.2. Median and 95% confidence interval of effective temperatures of 6+ ubiquitin during 5-ms trapping simulation for four different waveform profiles

Trapping

Waveform profile	Median T_{eff} / K	T_{eff} 95% CI / K
Pulse	369.0	368.6 – 369.5
Sawtooth	376.5	376.0 – 376.9
Sine	371.7	371.2 – 372.1
Triangle	370.2	369.9 – 370.6

Table B.1.3. Median and 95% confidence interval of effective temperatures of 6+ ubiquitin during 3.2-ms trapping simulation at varying guard potentials with a simulated wave height of 10 V_{p-p} and N_2 pressure of 2.5 Torr. These conditions were used to simulate trajectories whose results are shown in Figure B.1.4.

6+ Ubiquitin

Guard Potential / V	**Median T_{eff} / K**	**T_{eff} 95% CI / K**
1	330.0	329.4 – 330.6
2	333.9	333.5 – 334.4
3	338.1	337.7 – 338.7
4	342.7	342.1 – 343.3
5	347.0	346.5 – 347.6
10	369.9	369.3 – 370.5
15	393.5	393.0 – 394.2
20	418.8	418.1 – 419.5
25	445.7	445.1 – 446.3
30	474.1	473.3 – 474.9
35	506.2	505.5 – 507.0
40	537.4	536.5 – 538.3

Table B.1.4. Median and 95% confidence interval of effective temperatures of 1+ bradykinin during 3.2-ms trapping simulation at varying guard potentials with a simulated wave height of 10 V_{p-p} and N_2 pressure of 2.5 Torr. These conditions were used to simulate trajectories whose results are shown in Figure B.1.4.

1+ Bradykinin

Guard Potential / V	**Median T_{eff} / K**	**T_{eff} 95% CI / K**
1	334.1	333.1 – 335.2
2	344.1	342.9 – 344.9
3	347.0	346.1 – 348.1
4	353.1	352.1 – 354.2
5	357.2	356.1 – 358.2
10	385.1	384.1 – 386.4
15	423.6	422.4 – 424.8
20	463.4	462.0 – 464.9
25	502.2	500.7 – 503.7
30	543.7	542.3 – 545.1
35	600.7	599.0 – 601.9
40	701.2	689.6 – 709.6

Table B.1.5. Median and 95% confidence interval of effective temperatures of 6+ ubiquitin during 3.2-ms trapping simulation at varying guard potentials with a simulated wave height of 15 V_{p-p} and N_2 pressure of 3.0 Torr. These conditions provide a direct comparison to the experimental conditions used to generate the arrival-time distributions shown in Figure 3.3.

6+ Ubiquitin

Guard Potential / V	Median T_{eff} / K	T_{eff} 95% CI / K
1	350.0	349.6 – 350.4
2	354.5	354.1 – 355.0
3	360.1	359.6 – 360.5
4	365.1	364.6 – 365.5
5	369.6	369.1 – 370.1
10	395.4	395.0 – 396.0
15	422.9	422.2 – 423.4
20	453.7	453.0 – 454.3
25	486.0	485.2 – 486.8
30	521.5	520.8 – 522.3
35	560.6	559.9 – 561.3
40	605.8	604.9 – 606.3

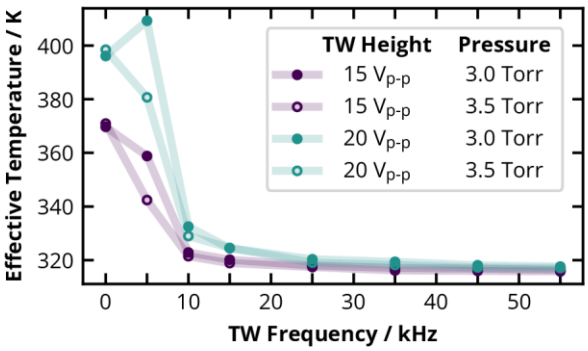

Figure B.1.1. The effect of TW frequency on median effective temperature of 6+ UBQ transmitted through the TW-SLIM region at a frequency of 30 kHz. Simulations were performed at two different TW heights and two different pressures. Effective temperatures calculated from simulations of trapped ions, i.e. in which the traveling wave voltages were applied and not moved throughout the simulation, are plotted as 0 kHz frequency for comparison to temperatures from transmission simulations. The total simulation time was 10 ms for each TW frequency simulated.

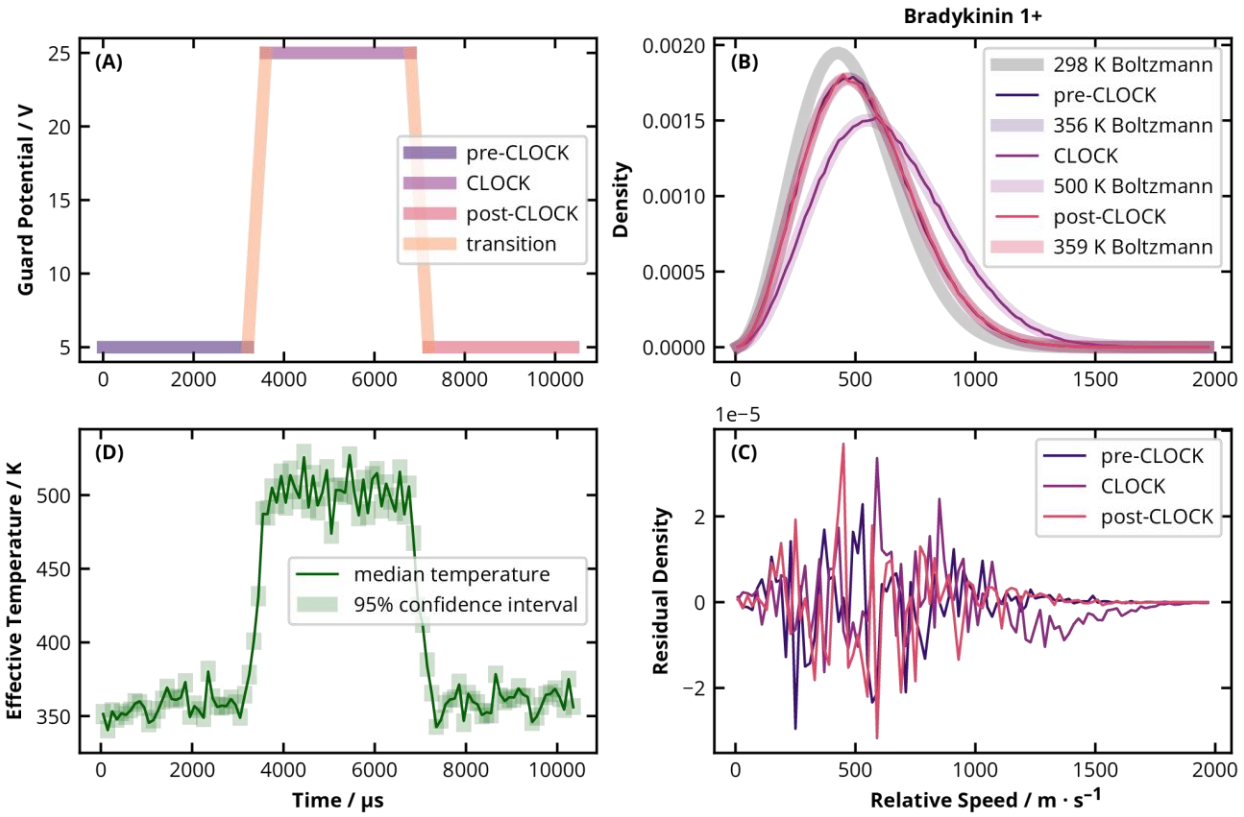

Figure B.1.2. The effect of applied guard potential during trapping in the TW-SLIM region on median effective temperature of 1+ BK. Trapping was simulated with a TW height of 10 $V_{p\text{-}p}$ and 2.5 Torr N_2. (A) Applied guard potential plotted as a function of simulation time. The guard electrodes were held at 5 V for 3.2 ms, ramped to 25 V over 0.4 ms, held at 25 V for 3.2 ms, ramped back down to 5 V over 0.4 ms, and held at 5 V for the final 3.2 ms. (B) Ion-neutral relative speed distributions constructed for the pre-CLOCK, CLOCK, and post-CLOCK segments of the ion trajectory and overlaid with the Maxwell-Boltzmann relative-speed distribution used to determine T_{eff} for each segment, respectively. The Maxwell-Boltzmann relative speed distribution at room temperature (298 K) is also shown for reference. (C) Residuals between the ion-neutral relative speed distributions and corresponding Maxwell-Boltzmann relative speed distributions from (B). (D) T_{eff}

calculated for each 104 µs segment of the simulated plotted as a function of simulation time and overlaid with the 95% confidence interval for each segment.

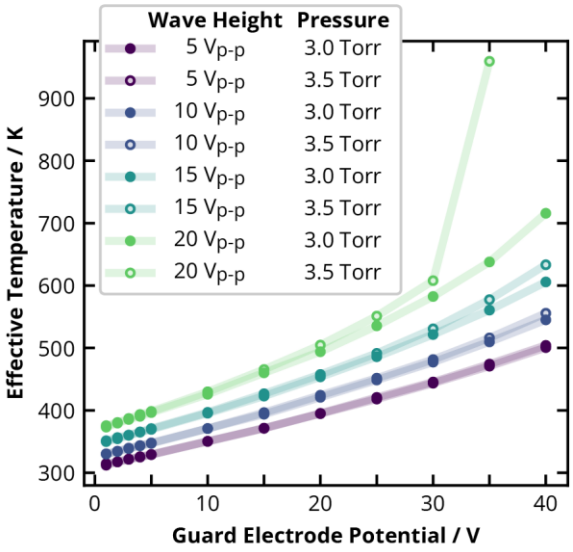

Figure B.1.3. Results from 3.2-ms trapped simulations of 6+ ubiquitin at varying guard electrode potentials. T_{eff} increases with guard potential, wave height, and pressure. The trajectory simulated with a wave height of 20 V_{p-p}, 3.5 Torr N_2, and 40 V guard potential was unstable, resulting in the ion colliding with the electrodes prior to the end of the simulation.

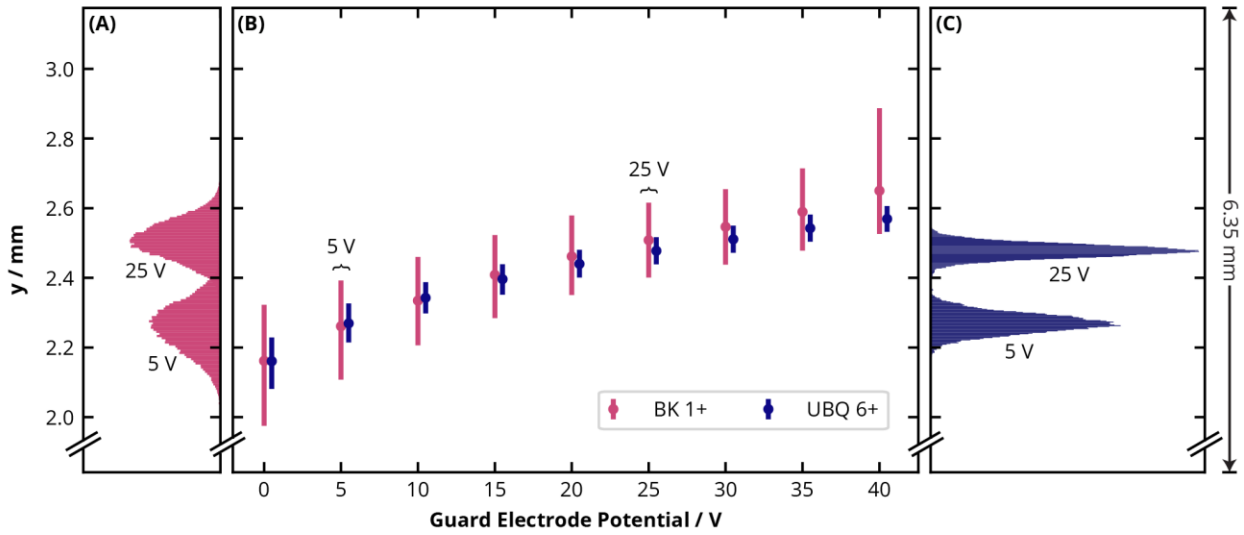

Figure B.1.4. Effect of applied guard potential on ion position along the y-axis (rf-confined between boards). (A) and (C) Histograms of ion distance from the center plane between the two SLIM boards (represented by y=0) during trapping with a TW height of 10 $V_{p\text{-}p}$ and 2.5 Torr N_2 for 1+ BK and 6+ UBQ, respectively, at guard voltages of 5 V and 25 V. From these and other histograms of ion position at each guard electrode potential, the median positions were determined and plotted in (B). The error bars represent the bounds containing the middle 95% of ion positions over a 3.2-ms trapping simulation. The 6+ ubiquitin data is plotted with a 0.5-V horizontal offset to aid in visualization. See Table S3 and Table S4 for tabulation of the median T_{eff} values and 95% confidence intervals for these ions under the simulated conditions.

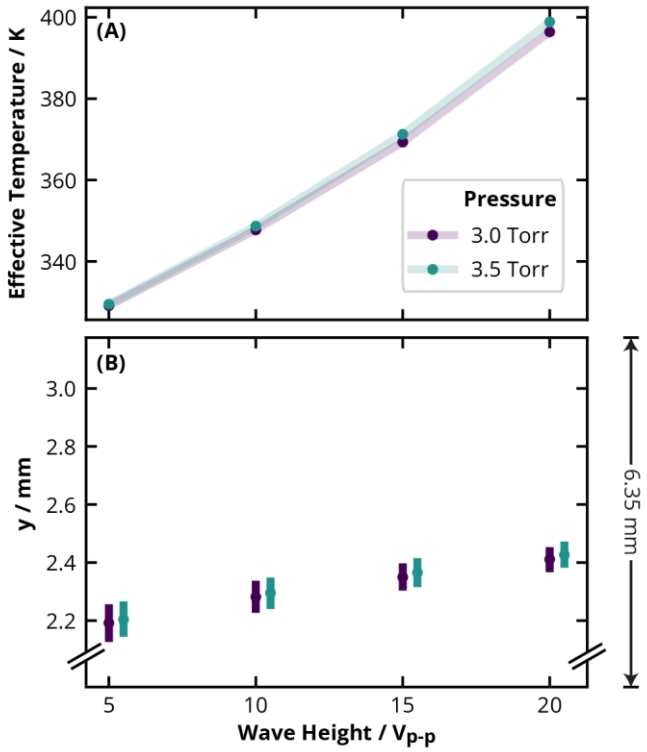

Figure B.1.5. Results from 3.2-ms trapped simulations of 6+ ubiquitin at varying wave heights. (A) T_{eff} versus wave height (data replotted from Figure B.1.3). (B) Median and 95% confidence interval of ion y position at each wave height, as determined in Figure B.1.4.

B.2 Sample SIMION user program

```
simion.workbench_program()

simion.import("collision_hs1.lua")

-- adjustable variables during flight
adjustable _temperature_k       = 298.15
adjustable _sigma_m2            = 1.2e-17
adjustable _gas_mass_amu        = 28.0
adjustable _mark_collisions     = 1
adjustable pe_update_each_usec  = 1
adjustable _pressure_pa         = 3.5*133.322368

-- adjustable variables at beginning of flight
adjustable _rf_frequency_hz         = 9.43E5
adjustable rf_phase_angle_deg       = 0.0
adjustable _rf_amplitude            = 120       --Vpp
adjustable _tw_frequency_hz         = 20000
adjustable tw_phase_angle_deg       = 0.0
adjustable _tw_amplitude            = 15        --Vpp
adjustable _guard_bias              = 5         --initial or default guard bias in volts
adjustable _guard_act               = 5         --changed guard bias in volts
adjustable _interval                = 3200      --time in usec for each segment of simulation
adjustable _rise_time               = 400       --rise time in usec for DC channel as measured
on oscilloscope

-- internal variables
local rf_omega                -- frequency in radians / usec
local rf_theta                -- phase offset in radians
--local tw_omega
--local tw_theta
local last_pe_update = 0.0  -- last potential energy surface update time (usec)

function segment.fast_adjust()
    -- Initialize constants once.
    if not rf_theta then
        rf_theta = rf_phase_angle_deg * (3.141592 / 180)
        rf_omega = _rf_frequency_hz * 6.28318E-6
    --  tw_theta = tw_phase_angle_deg * (3.141592 / 180)
    --  tw_omega = _tw_frequency_hz * 6.28318E-6
    end

    -- Apply RF+DC to each electrode.
    local rf_volts = sin(ion_time_of_flight * rf_omega - rf_theta) * _rf_amplitude
    local tw_volts = _tw_amplitude / 2

    for n=1,4,1 do
        adj_elect[n] = tw_volts
    end

    for m=5,8,1 do
        adj_elect[m] = -tw_volts
    end

    adj_elect10 = rf_volts
    adj_elect11 = -rf_volts

    -- Step guard voltage from default to test value and back to default value. Each value is
held for defined interval.
    -- Guard voltage is ramped between values over empirically-measured rise time.
    if (ion_time_of_flight <= _interval) or (ion_time_of_flight > (2 * _interval + 2 *
_rise_time)) then
        adj_elect9 = _guard_bias
```

```
60.     end
61.
62.     if (ion_time_of_flight > (_interval + _rise_time)) and (ion_time_of_flight <= (2 * _interval
+ _rise_time)) then
63.         adj_elect9 = _guard_act
64.     end
65.
66.     if (ion_time_of_flight > _interval) and (ion_time_of_flight <= _interval + _rise_time) then
67.         adj_elect9 = ((_guard_act - _guard_bias) / _rise_time) * (ion_time_of_flight -
_interval) + _guard_bias
68.     end
69.
70.     if (ion_time_of_flight > (2 * _interval + _rise_time)) and (ion_time_of_flight <= (2 *
_interval + 2 * _rise_time)) then
71.         adj_elect9 = ((_guard_bias - _guard_act) / _rise_time) * (ion_time_of_flight - (2 *
_interval + _rise_time)) + _guard_act
72.     end
73.
74. end
75.
76.
77. -- This trick first runs the other_actions segment defined previously
78. -- by the HS1 collision model and then runs our own code.
79. local previous_other_actions = segment.other_actions  -- copy previously defined segment.
80. function segment.other_actions()
81.     -- Run previously defined segment.
82.     previous_other_actions()
83.     -- Now run our own code...
84.
85.     -- Update PE surface display.
86.     if abs(ion_time_of_flight - last_pe_update) >= pe_update_each_usec then
87.         last_pe_update = ion_time_of_flight
88.         sim_update_pe_surface = 1    -- Request a PE surface display update.
89.     end
90.     if ion_time_of_flight >= (3 * _interval + 2 * _rise_time) then
91.             ion_splat = 1
92.     end
93. end
```

B.3 Sample SIMION trajectory data

```
------ Begin Next Fly'm ------


"Begin Fly'm (Fri Apr 04 18:07:38 2025)"
"Ions Flown Separately, Comp Quality(3)"
"Number of Ions to Fly = 1"


"Ion N","TOF","X","Y","Z","Vx","Vy","Vz","E","dE/dx","dE/dy","dE/dz"

1,0.00487116,15.809,6.14239,-2.37007,-0.00171643,-0.00167186,0.000328826,-0.344932,-0.000579307,-
0.000439345,1.19413
1,0.00595493,15.809,6.14239,-2.37007,-0.000845653,-0.000204407,0.0017941,-0.34482,-0.000579697,-
1.21421,1.19375
1,0.00845032,15.809,6.14239,-2.37007,-0.000267178,-0.00160021,0.00328063,-0.344767,-0.000580069,-
1.73188,1.19358
1,0.00888382,15.809,6.14239,-2.37007,0.00242224,-0.00259335,0.00376663,-0.344756,-0.000580095,-
1.82178,1.19355
1,0.0105094,15.809,6.14238,-2.37006,0.00325512,-0.00234128,0.00437203,-0.344708,-0.000579522,-
2.15874,1.19342
1,0.0184205,15.809,6.14237,-2.37003,0.00173182,0.000262686,0.00316119,-0.344463,-0.00057572,-
3.795,1.19272
1,0.0208048,15.809,6.14237,-2.37002,0.000958016,-0.00123433,0.000834197,-0.344407,-0.000575131,-
4.28664,1.19256
1,0.0209131,15.809,6.14237,-2.37002,0.00210432,0.0005619,0.000791106,-0.344404,-0.000575117,-
4.30896,1.19255
1,0.0212383,15.809,6.14237,-2.37002,0.00216958,0.00391088,0.00234157,-0.344397,-0.000575018,-
4.37594,1.19253
1,0.0274154,15.809,6.1424,-2.37001,0.00132996,0.00723805,0.00223654,-0.344416,-0.000573084,-
5.645,1.1925
1,0.0334836,15.8091,6.14245,-2.36999,0.00125856,0.0108762,0.000443804,-0.344659,-0.000571979,-
6.88429,1.19306
1,0.0383593,15.8091,6.14251,-2.36999,0.00186242,0.0134615,2.90503e-005,-0.345094,-0.000571153,-
7.87376,1.19412
1,0.04086,15.8091,6.14255,-2.36999,0.00113705,0.0175327,0.00163134,-0.345406,-0.000570502,-
8.37869,1.19489
1,0.0435677,15.8091,6.1426,-2.36999,-1.86932e-005,0.0196221,0.00358756,-0.345879,-0.00057011,-
8.92321,1.19608
1,0.0437843,15.8091,6.1426,-2.36999,-0.00123523,0.0190633,0.00267763,-0.345922,-0.000570117,-
8.96666,1.19619
1,0.0454088,15.8091,6.14263,-2.36998,-0.000291005,0.0196455,0.00158613,-0.346251,-0.000570478,-
9.29206,1.19702
1,0.0480078,15.8091,6.14269,-2.36998,-0.00149759,0.0217171,0.00334189,-0.346846,-0.00057068,-
9.81093,1.19853
1,0.0491988,15.8091,6.14271,-2.36998,-0.0014266,0.0202539,0.00571905,-0.347154,-0.000570997,-
10.0479,1.19932
1,0.0511479,15.8091,6.14275,-2.36997,-0.00241717,0.0211332,0.00625191,-0.347656,-0.000571498,-
10.4344,1.20061
1,0.053205,15.8091,6.1428,-2.36995,-0.00363466,0.0210927,0.00930822,-0.348238,-0.000572343,-
10.8408,1.20211
1,0.0579681,15.809,6.14291,-2.36991,-0.00597722,0.027269,0.00976456,-0.349764,-0.000575212,-
11.7749,1.20607
1,0.0603483,15.809,6.14298,-2.36989,-0.00578813,0.030462,0.00920627,-0.350754,-0.000577519,-
12.238,1.20865
1,0.0620788,15.809,6.14303,-2.36987,-0.0084485,0.0280706,0.0107148,-0.351578,-0.000579151,-
12.5732,1.21078
1,0.0630523,15.809,6.14306,-2.36986,-0.00836666,0.0297567,0.0107721,-0.352022,-0.000580467,-
12.7611,1.21194
1,0.0631605,15.809,6.14306,-2.36986,-0.00647141,0.0285288,0.00932151,-0.352074,-0.000580613,-
12.7819,1.21207
1,0.0640259,15.809,6.14309,-2.36985,-0.00542811,0.0305878,0.0104404,-0.352484,-0.00058152,-
12.9486,1.21314
```

```
1,0.0692162,15.809,6.14326,-2.3698,-0.00709829,0.0367097,0.00978016,-0.355396,-0.00058616,-
13.9406,1.2207
1,0.0706211,15.809,6.14331,-2.36978,-0.00665978,0.0408208,0.00743001,-0.35633,-0.000587787,-
14.2068,1.22312
1,0.0776385,15.8089,6.14362,-2.36973,-0.00678577,0.0473121,0.00500583,-0.362173,-0.000595498,-
15.5216,1.23823
1,0.0777464,15.8089,6.14362,-2.36973,-0.00836673,0.0470555,0.00643528,-0.362274,-0.00059562,-
15.5416,1.23849
1,0.0790411,15.8089,6.14369,-2.36973,-0.0103832,0.0474873,0.00453514,-0.363512,-0.000597393,-
15.7812,1.24169
1,0.0816299,15.8089,6.14381,-2.36971,-0.0123159,0.0498665,0.00400138,-0.366126,-0.000601749,-
16.2576,1.24843
1,0.0896031,15.8088,6.14425,-2.36968,-0.0119606,0.0576154,-0.00040287,-0.375672,-0.000617646,-
17.7002,1.27306
1,0.091756,15.8088,6.14437,-2.36969,-0.0120086,0.0581379,-0.00323522,-0.378639,-0.000621844,-
18.0834,1.28071
1,0.0948769,15.8087,6.14456,-2.3697,-0.0111895,0.0621655,-0.00273386,-0.383181,-0.000627965,-
18.634,1.29238
1,0.0967051,15.8087,6.14468,-2.3697,-0.0127715,0.0630183,-0.00866618,-0.386043,-0.000631335,-
18.9535,1.29975
1,0.0978877,15.8087,6.14475,-2.36971,-0.0102906,0.0657438,-0.00692982,-0.38795,-0.000633803,-
19.1593,1.30464
1,0.10808,15.8086,6.14549,-2.36979,-0.00941346,0.077717,-0.0062857,-0.407402,-0.000651408,-
20.8922,1.35465
1,0.116848,15.8085,6.14623,-2.36985,-0.00758847,0.0914114,-0.00725157,-0.428211,-0.000665687,-
22.3215,1.40821
1,0.117062,15.8085,6.14625,-2.36985,-0.00664808,0.0891013,-0.0101269,-0.428777,-0.000665979,-
22.3555,1.40967
1,0.118129,15.8085,6.14634,-2.36986,-0.00672123,0.0934717,-0.00966769,-0.431591,-0.000667278,-
22.5255,1.41691
1,0.123771,15.8084,6.1469,-2.36991,-0.00654627,0.102699,-0.0105645,-0.447982,-0.000674328,-
23.4083,1.4591
1,0.124302,15.8084,6.14695,-2.36992,-0.00674687,0.10392,-0.0102027,-0.449636,-0.000674986,-
23.4901,1.46336
1,0.126319,15.8084,6.14716,-2.36994,-0.0105315,0.104908,-0.0112084,-0.456104,-0.00067756,-
23.7985,1.48001
1,0.126849,15.8084,6.14722,-2.36995,-0.0107674,0.104063,-0.0117277,-0.457823,-0.00067855,-
23.8791,1.48444
1,0.130985,15.8084,6.14766,-2.37,-0.0114675,0.111546,-0.0113915,-0.471707,-0.000686464,-
24.4993,1.52018
1,0.134685,15.8083,6.14809,-2.37004,-0.012957,0.116523,-0.0106659,-0.485196,-0.000694041,-
25.0417,1.55492
1,0.135425,15.8083,6.14817,-2.37005,-0.0104462,0.115705,-0.0103134,-0.487984,-0.000695735,-
25.1485,1.56211
1,0.139857,15.8083,6.1487,-2.37009,-0.00831682,0.122511,-0.0114027,-0.50529,-0.000704212,-
25.7788,1.6067
1,0.140805,15.8083,6.14882,-2.3701,-0.00904138,0.125686,-0.0109685,-0.509161,-0.000705725,-
25.9114,1.61668
1,0.146998,15.8082,6.14963,-2.37017,-0.0102599,0.134499,-0.0120108,-0.536364,-0.000716468,-
26.7569,1.68679
1,0.150033,15.8082,6.15005,-2.37021,-0.0112038,0.13832,-0.0137711,-0.550609,-0.000722393,-
27.1581,1.72351
1,0.153792,15.8081,6.15058,-2.37026,-0.0108759,0.145521,-0.0138961,-0.569101,-0.000730363,-
27.6433,1.77117
1,0.156602,15.8081,6.151,-2.3703,-0.00922767,0.147888,-0.0160442,-0.583693,-0.000736248,-
27.9969,1.80878
1,0.158681,15.8081,6.15131,-2.37034,-0.0100086,0.151607,-0.0182289,-0.594746,-0.000740086,-
28.2539,1.83726
1,0.164067,15.808,6.15215,-2.37044,-0.0083313,0.163579,-0.019483,-0.625035,-0.000750836,-
28.9003,1.91531
1,0.165304,15.808,6.15236,-2.37046,-0.00831229,0.16521,-0.01798,-0.6324,-0.000753014,-
29.0447,1.93429
1,0.172082,15.808,6.15352,-2.37059,-0.00984992,0.178271,-0.0214099,-0.674913,-0.000765135,-
29.8069,2.04387
```

```
1,0.173002,15.808,6.15369,-2.37061,-0.00930349,0.174148,-0.0222581,-0.680987,-0.000767031,-
29.9068,2.05953
1,0.175969,15.8079,6.15421,-2.37067,-0.00888407,0.179878,-0.02185,-0.700561,-0.000772897,-
30.2234,2.10997
1,0.177092,15.8079,6.15442,-2.3707,-0.00739363,0.182765,-0.0200797,-0.708159,-0.000775061,-
30.3407,2.12955
1,0.178111,15.8079,6.1546,-2.37072,-0.0061174,0.183942,-0.0230011,-0.715167,-0.000776795,-
30.4459,2.14762
1,0.182683,15.8079,6.15547,-2.37082,-0.00787892,0.195566,-0.023259,-0.747631,-0.000783731,-
30.905,2.23128
1,0.184098,15.8079,6.15575,-2.37086,-0.00728208,0.199326,-0.0242131,-0.758148,-0.000786318,-
31.0424,2.25839
1,0.186113,15.8079,6.15615,-2.37091,-0.00681559,0.200565,-0.023268,-0.773492,-0.000789842,-
31.2344,2.29794
1,0.18702,15.8079,6.15633,-2.37093,-0.00929651,0.199548,-0.0209793,-0.780426,-0.000791366,-
31.3193,2.31582
1,0.187524,15.8079,6.15643,-2.37094,-0.00970725,0.200859,-0.0225414,-0.784265,-0.000792413,-
31.366,2.32572
1,0.189838,15.8078,6.15691,-2.37099,-0.00991599,0.202799,-0.0223859,-0.802208,-0.000797404,-
31.5771,2.37198
1,0.190542,15.8078,6.15705,-2.37101,-0.00731787,0.202815,-0.0233235,-0.807694,-0.000798951,-
31.6401,2.38613
1,0.190643,15.8078,6.15707,-2.37101,-0.0059904,0.20258,-0.0234458,-0.808477,-0.000799129,-
31.6491,2.38814
1,0.196257,15.8078,6.15824,-2.37114,-0.00349116,0.212122,-0.0270367,-0.853522,-0.000808047,-
32.1319,2.50428
1,0.199449,15.8078,6.15893,-2.37123,-0.00218883,0.217882,-0.0261061,-0.880137,-0.00081192,-
32.3913,2.57289
1,0.203519,15.8078,6.15983,-2.37134,-0.00319089,0.226072,-0.0266316,-0.915209,-0.000816105,-
32.7048,2.66331
1,0.204607,15.8078,6.16008,-2.37137,-0.00322351,0.226298,-0.0249858,-0.924803,-0.00081742,-
32.7854,2.68805
1,0.205101,15.8078,6.16019,-2.37138,-0.00310758,0.228084,-0.0249682,-0.929161,-0.000818021,-
32.8215,2.69929
1,0.205595,15.8078,6.16031,-2.37139,-0.00483414,0.229392,-0.0219821,-0.933548,-0.000818615,-
32.8573,2.7106
1,0.20599,15.8078,6.1604,-2.3714,-0.00561523,0.230163,-0.021463,-0.93707,-0.000819203,-
32.8856,2.71968
1,0.2112,15.8077,6.16163,-2.37151,-0.00567857,0.24041,-0.0214433,-0.984749,-0.000827737,-
33.2418,2.84268
1,0.211298,15.8077,6.16165,-2.37152,-0.0057683,0.240142,-0.0207345,-0.985662,-0.000827901,-
33.2482,2.84503
1,0.215107,15.8077,6.16258,-2.3716,-0.00486616,0.24829,-0.0209488,-1.02177,-0.000834366,-
33.4876,2.93819
1,0.215497,15.8077,6.16268,-2.37161,-0.00358429,0.248543,-0.0212883,-1.02552,-0.000834976,-
33.5111,2.94787
1,0.218022,15.8077,6.16331,-2.37166,-0.000930808,0.254589,-0.0252697,-1.05012,-0.000838425,-
33.6592,3.01135
1,0.218603,15.8077,6.16346,-2.37167,-0.00126748,0.250549,-0.0226684,-1.05587,-0.000838972,-
33.6924,3.02618
1,0.220059,15.8077,6.16383,-2.37171,-0.00080547,0.253829,-0.0227981,-1.07012,-0.000840412,-
33.7735,3.06293
1,0.220737,15.8077,6.164,-2.37172,0.000238167,0.254747,-0.023784,-1.07681,-0.000841037,-
33.8104,3.08021
1,0.226422,15.8077,6.16549,-2.37186,-0.000176434,0.262613,-0.0254233,-1.13428,-0.000845402,-
34.0988,3.22848
1,0.226807,15.8077,6.16559,-2.37187,0.000948564,0.263554,-0.0242834,-1.13819,-0.000845725,-
34.117,3.23857
1,0.228535,15.8077,6.16605,-2.37191,0.00138603,0.266131,-0.0228538,-1.15592,-0.000846868,-
34.1962,3.2843
1,0.23026,15.8077,6.16651,-2.37195,0.00278895,0.269039,-0.0217446,-1.17374,-0.000847896,-
34.2713,3.33028
```

B.4 iontemperature.py

```
 1. import numpy as np
 2. import matplotlib.pyplot as plt
 3. from scipy.optimize import leastsq
 4. import gzip
 5.
 6. class relative_speed_distribution:
 7.
 8.     def __init__(self, m, M, T, file_path="", low=0.0, high=4000.0, step=20., empty=False):
 9.         """
10.         Initializes the parameters underlying the distribution.
11.         Input variables:
12.         m is the mass of the ion in Da.
13.         M is the mass of the neural in Da.
14.         T is the temperature of the bath gas.
15.         low is the lowest speed in m/s.
16.         high is the highest speed in m/s.
17.         step is the bin increment in m/s.
18.         """
19.         avogadro_constant = 6.02214076e23
20.         self.m = m/(avogadro_constant*1000)    # Mass of the ion in kg
21.         self.M = M/(avogadro_constant*1000)    # Mass of the neutral in kg
22.         self.u = self.m*self.M/(self.m+self.M) # Reduced mass of the ion-neutral pair in kg
23.         self.T = T                             # Temperature of the bath gas in Kelvin
24.         self.k = 1.38066e-23                   # Boltzmann constant in J per Kelvin
25.         self.v_edges = np.arange(low, high, step)
26.         self.v_centers = (self.v_edges[0:-1]+self.v_edges[1:])/2.0
27.
28.         if len(file_path) > 0:
29.             self.file_path = file_path
30.             self.import_trajectory_text()
31.             self.generate_density()
32.
33.     def boltzmann_speeds(self, T):
34.         """
35.         Returns the Boltzmann ion-neutral speed distribution
36.         """
37.         v = self.v_centers
38.         u = self.u
39.         k = self.k
40.         return np.power(u/(2*np.pi*k*T),1.5)*4*np.pi*v*v*np.exp((-u*v*v)/(2*k*T))
41.
42.     def residual(self, T):
43.         """
44.         Returns the residual between a target distribution and that for a Boltzmann
distribution.
45.         """
46.         return self.boltzmann_speeds(T)-self.density
47.
48.     def optimize(self, T0):
49.         """
50.         Optimizes T_effective using:
51.         https://docs.scipy.org/doc/scipy-
1.15.0/reference/generated/scipy.optimize.leastsq.html#scipy.optimize.leastsq
52.         """
53.         return leastsq(self.residual, T0)[0]
54.
55.     def thermal_velocities(self,shape, m, T):
56.         k = self.k
57.         return np.random.normal(scale = np.sqrt(k*T/m), size = shape)
58.
59.     def import_trajectory_text_legacy(self):
60.         """
```

```
        Imports ion velocites from a trajectory file.
        Original function, before meta data.
        """
        original_population = np.loadtxt(fname=self.file_path, delimiter=',',skiprows=1)
        self.v_ion = original_population[:,5:8]*1.0e3
        print("Imported trajectory with " + str(np.shape(self.v_ion)[0]) + " collisions.")

    def import_trajectory_text(self):
        """
        Imports ion velocites from a trajectory file.
        """

        def find_meta(file_path, search_string="Ion N"):
            """
            Find line number containing the specified string in either a text file or gzipped
text file.

            Args:
                file_path (str): Path to the file to search
                search_string (str): String to search for

            Returns:
                int or None: Line number if found, None if not found or error occurs
            """
            try:
                # Check if file is gzipped by looking at file extension
                is_gzipped = file_path.lower().endswith('.gz')

                # Open file with appropriate method
                opener = gzip.open if is_gzipped else open
                mode = 'rt' if is_gzipped else 'r'

                with opener(file_path, mode) as file:
                    for line_num, line in enumerate(file, 1):
                        if search_string in line:
                            return line
                return None

            except FileNotFoundError:
                print(f"Error: File '{file_path}' not found.")
                return None
            except Exception as e:
                print(f"An error occurred: {e}")
                return None

        def find_pos_index(header_string):
            """
            Find the index of 'X' in a comma-separated string.

            Args:
                header_string(str): Comma-separated string containing column names

            Returns:
                int: Index of 'X', or -1 if not found
            """
            #Split the string and strip quotes and whitespace from each element
            headers = [field.strip(' "\'') for field in header_string.split(',')]

            try:
                return headers.index('X')
            except ValueError:
                return -1

        def find_vx_index(header_string):
            """
```

```
125.             Find the index of 'Vx' in a comma-separated string.
126.
127.             Args:
128.                 header_string (str): Comma-separated string containing column names
129.
130.             Returns:
131.                 int: Index of 'Vx', or -1 if not found
132.             """
133.             # Split the string and strip quotes and whitespace from each element
134.             headers = [field.strip(' "\'') for field in header_string.split(',')]
135.
136.             try:
137.                 return headers.index('Vx')
138.             except ValueError:
139.                 return -1
140.
141.         def find_tof_index(header_string):
142.             """
143.             Find the index of 'TOF' in a comma-separated string.
144.
145.             Args:
146.                 header_string (str): Comma-separated string containing column names
147.
148.             Returns:
149.                 int: Index of 'TOF', or -1 if not found
150.             """
151.             # Split the string and strip quotes and whtiespace from each element
152.             headers = [field.strip(' "\'') for field in header_string.split(',')]
153.
154.             try:
155.                 return headers.index('TOF')
156.             except ValueError:
157.                 return -1
158.
159.         def find_trajectory(file_path, search_string="0123456789"):
160.             """
161.             Find line number containing the specified string in either a text file or gzipped
text file.
162.
163.             Args:
164.                 file_path (str): Path to the file to search
165.                 search_string (str): String to search for
166.
167.             Returns:
168.                 int or None: Line number if found, None if not found or error occurs
169.             """
170.             try:
171.                 # Check if file is gzipped by looking at file extension
172.                 is_gzipped = file_path.lower().endswith('.gz')
173.
174.                 # Open file with appropriate method
175.                 opener = gzip.open if is_gzipped else open
176.                 mode = 'rt' if is_gzipped else 'r'
177.
178.                 with opener(file_path, mode) as file:
179.                     for line_num, line in enumerate(file, 1):
180.                         if line[0] in search_string:
181.                             return line_num
182.                 return None
183.
184.             except FileNotFoundError:
185.                 print(f"Error: File '{file_path}' not found.")
186.                 return None
187.             except Exception as e:
188.                 print(f"An error occurred: {e}")
```

```
189.                 return None
190.
191.         meta_text = find_meta(self.file_path)
192.         pos_index = find_pos_index(meta_text)
193.         vx_index = find_vx_index(meta_text)
194.         tof_index = find_tof_index(meta_text)
195.         first_line = find_trajectory(self.file_path)
196.
197.         original_population = np.loadtxt(fname=self.file_path,
delimiter=',',skiprows=(first_line-1))
198.         self.pos_ion = original_population[:,pos_index:(pos_index+3)]
199.         self.v_ion = original_population[:,vx_index:(vx_index+3)]*1.0e3
200.         self.time = original_population[:,tof_index]
201.         print("Imported trajectory with " + str(np.shape(self.v_ion)[0]) + " collisions.")
202.
203.     def generate_density(self):
204.         """
205.         Calculates the densities of a relative speed distribution.
206.         """
207.         self.v_gas = self.thermal_velocities(np.shape(self.v_ion), self.M, self.T)
208.         relative_speeds = np.sqrt(np.sum(np.square(self.v_ion-self.v_gas),axis=1))
209.         self.density = np.histogram(relative_speeds, bins=self.v_edges, density=True)[0]
210.
211.     def generate_density_resample(self):
212.         """
213.         Resamples with replacement from the original ion velocities, and
214.         then generates a new relative ion-neutral speed distribution.
215.         """
216.         rng = np.random.default_rng()
217.         v_ion_resample = rng.choice(self.v_ion,np.shape(self.v_ion)[0],replace=True)
218.         v_gas_resample = self.thermal_velocities(np.shape(self.v_ion), self.M, self.T)
219.         relative_speeds = np.sqrt(np.sum(np.square(v_ion_resample-v_gas_resample),axis=1))
220.         self.density = np.histogram(relative_speeds, bins=self.v_edges, density=True)[0]
221.
222.     def bootstrap_temperature(self, num_resamples = 200, alpha = 0.05):
223.         """
224.         Calculates a confidence interval for the temperature, based on resampled
225.         ion-neutral speed distributions.
226.         """
227.         self.alpha = alpha
228.         Teff = self.optimize(T0=self.T)
229.         Ttemp = np.zeros(num_resamples,dtype=np.float64)
230.         for i in range(num_resamples):
231.             self.generate_density_resample()
232.             Ttemp[i] = self.optimize(T0=Teff)
233.         indices = np.arange(num_resamples)
234.         self.T_resamples = np.sort(Ttemp)
235.         self.T_low = np.interp(num_resamples*alpha/2., indices,self.T_resamples)
236.         self.T_median = np.interp(num_resamples*0.5-0.5, indices, self.T_resamples)
237.         self.T_high = np.interp(num_resamples-1.-(num_resamples*alpha/2.),
indices,self.T_resamples)
238.
239.     def plot_velocity_distributions(self):
240.         """
241.         Relative velocity distribution of the ion from the imported trajectory.
242.         """
243.         fig, ax = plt.subplots(1,3,sharex=True)
244.         ax[0].hist(self.v_ion[:,0])
245.         ax[1].hist(self.v_ion[:,1])
246.         ax[2].hist(self.v_ion[:,2])
247.         ax[0].set_ylabel('Frequency')
248.         ax[0].set_yticklabels([])
249.         ax[1].set_yticklabels([])
250.         ax[2].set_yticklabels([])
251.         ax[0].set_xlabel('$V_x$')
```

```
252.         ax[1].set_xlabel('$V_y$')
253.         ax[2].set_xlabel('$V_z$')
254.
255.         plt.show()
256.
257.     def plot_speed_distributions(self):
258.         """
259.         Relative speed distribution from the imported trajectory.
260.         """
261.         fig, (ax1, ax2) = plt.subplots(2, 1,  sharex=True)
262.         ax1.plot(self.v_centers,self.density,label='Trajectory')
263.         Teff = self.optimize(T0=self.T)
264.         label = str(int(Teff)) + " K Boltzmann"
265.         ax1.plot(self.v_centers,self.boltzmann_speeds(Teff),label=label)
266.         ax2.plot(self.v_centers,self.residual(Teff),label='Residual')
267.
268.         ax1.set_title('Speed Distributions')
269.         ax2.set_xlabel('Relative Speed / m/s')
270.         ax1.set_ylabel('Density')
271.         ax2.set_ylabel('Residual')
272.         ax1.legend()
273.         ax2.legend()
274.         plt.show()
275.
276.     def plot_bootstrap(self):
277.         """
278.         Plots to visualize the results of bootstrapping and the determination of critical
temperatures
279.         from the resulting distributions.
280.         """
281.         fig, (ax1, ax2) = plt.subplots(2, 1,  sharex=True)
282.         num_resamples = np.size(self.T_resamples)
283.         ax1.hist(self.T_resamples, bins = int(np.sqrt(num_resamples)))
284.         ax2.plot(self.T_resamples,np.arange(num_resamples)/num_resamples)
285.         ax2.axvline(self.T_low)
286.         ax2.axvline(self.T_median)
287.         ax2.axvline(self.T_high)
288.
289.         ax1.set_title('Results from Bootstrap')
290.         ax2.set_xlabel('Effective Temperature / K')
291.         ax1.set_ylabel('Frequency')
292.         ax2.set_ylabel('Cum. Prob.')
293.         plt.show()
294.
295.
```